# Search for the Top Quark in the $e+$jets with $\mu-$tag Channel at DØ

by

Ssu-Min Chang

## ABSTRACT

The results of a search for the top quark in the $e+$jets with $\mu-$tag channel are presented. The search is performed with the DØ detector at the Fermilab Tevatron $p\bar{p}$ collider with an integrated luminosity of 74.9 $\mathrm{pb}^{-1}$ collected during 1993-95 run period of $\sqrt{s} = 1.8\,\mathrm{TeV}$. After optimizing the analysis for high top quark masses ($m_t > 130\,\mathrm{GeV}$), we observe 4 candidate events with an expected background of $1.44 \pm 0.20$ events. The probability for an upward fluctuation of the background to 4 or more events is 6.1%, which corresponds to 1.6 standard deviations. Assuming the excess is due to $t\bar{t}$ production and a top mass of $180\,\mathrm{GeV/c^2}$, we obtain a cross section of $\sigma(p\bar{p} \to t\bar{t} + X) = 4.9 \pm 3.6\,\mathrm{pb}$.

Submitted in partial fulfillment of the requirements
for the degree of Doctor of Philosophy in Physics
in the Graduate School of Arts and Sciences of
Northeastern University, July 1996

# Acknowledgements

First of all, I would like to thank my advisors Michael Glaubman and Darien Wood. Because of their continual support, encouragement, and guidance, I finally completed my study and finished this thesis. Mike Glaubman taught me a lot of things not only in physics, but also in other respects of life which will remain with me forever. Darien Wood has a broad knowledge about experimental high energy physics and always dedicated his time to research which have been a great inspiration to me.

I would also like to thank the members of Northeastern High Energy group at DØ: Takahiro Yasuda, Judd Wilcox, Steve Reucroft, Jorge H. Moromisato, and Eberhard Von Goeler. They were always very patient to answer ignorant questions from me. In particular, I am grateful to Takahiro Yasuda who usually invited me to dinner every time he visited Fermilab. Our new post doctors Pierrick Hanlet and Oliver Bardon provided me with helpful comments and advice for the defence for which I am thankful. I thank Professor Yogendra Srivastava, Robert S. Markiewics and John Swain in my thesis committee for their time and valuable comments. My schoolmates Pauti Chang, Hossein Johari, Erfan Amidi, Regina Demina, Syan-Sheng Gau, Sudeshna Palit, Daniel Hogenboom, Elisabetta Sassaroli, Kwok Lung Chan, and Chi Hing Mak have always been willing to help me and shared their fun with me.

The DØ top group created a enjoyable environment for me to work. I am grateful to Rich Partridge, Herbert Greenlee, Pushpalatha C. Bhat, Serban Protopopescu, Jim Cochran, Meenakshi Narain, John Hobbs, Chip Stewart, Jianming Qian, Bill Cobau, and Ryuji Yamada for teaching and supporting me throughout this analysis.

Jadzia Warchol, John Skeen, Stefan Gruenendahl, and Alan Bross taught me how to use DØ software when I started to work on upgraded tracking simulation, and Mary Ann Cummings, Jan Guida, Al Ito helped me do muon online calibration. I appreciate their help and kindness. I also thank the accelerator group to provide us $p\bar{p}$ beams to do experiment.

I also thank my friends Yi-Cheng Liu, Frank Hsieh, Howei Xu, Qiang Zhu, Jie Yang, Hailin Li, Ting Hu, Guoliang Wang, Hui Zhu, Tong Hu, John Jiang, Wei Chen, Freedy Nang, Cary Yoshikawa, Eunil Won, Chang Lyong Kim, Gene Alvarez, Sailesh Chopra, Singh Harpreet, and Vipin Bhatnagar. Because of their friendship, life in Fermilab is more enjoyable and colorful.

At last I have to thank my parents and five sisters. Without their fully support, I would not have finished my degree.

This thesis is dedicated to my mother.

# Contents

**Abstract** . . . . . iii

**Acknowledgements** . . . . . v

**List of Tables** . . . . . xii

**List of Figures** . . . . . xvi

**1 Introduction** . . . . . 1

1.1 The Standard Model . . . . . 2

1.2 The Top Quark . . . . . 6

1.2.1 Why the Top was Expected to Exist . . . . . 6

1.2.2 Discovery of the Top Quark . . . . . 7

1.2.3 Production and Decay of the Top Quark . . . . . 9

1.2.4 The Top Quark and New Physics . . . . . 13

**2 Experimental Apparatus** . . . . . 15

2.1 The Fermilab Tevatron . . . . . 15

2.2 The DØ Detector . . . . . 18

2.3 Central Detector (CD) . . . . . 22

2.3.1 Vertex Chamber (VTX) . . . . . 22
2.3.2 Central Drift Chamber (CDC) . . . . . 23
2.3.3 Forward Drift Chamber (FDC) . . . . . 24
2.3.4 Transition Radiation Detector (TRD) . . . . . 25
2.4 Calorimeters . . . . . 26
2.4.1 The Central Calorimeter (CC) . . . . . 33
2.4.2 The End Calorimeter (EC) . . . . . 33
2.4.3 Intercryostat Detectors and Massless Gaps . . . . . 34
2.5 Muon Detector . . . . . 34
2.5.1 The Muon Toroids . . . . . 36
2.5.2 Wide Angle Muon System (WAMUS) . . . . . 37
2.5.3 Small Angle Muon System (SAMUS) . . . . . 41
2.6 Triggering and Data Acquisition . . . . . 41
2.6.1 Level 0 . . . . . 43
2.6.2 Level 1 . . . . . 43
2.6.3 Level 2 . . . . . 45

**3 Event Reconstruction and MC Simulation . . . . . 47**
3.1 Event Vertex . . . . . 48
3.2 Missing Transverse Energy . . . . . 49
3.3 Electrons . . . . . 51
3.3.1 Reconstruction of Electrons and Photons . . . . . 51
3.3.2 Offline Electron Selection . . . . . 53
3.4 Jets . . . . . 63

3.4.1 Jet Reconstruction . . . . . 63
3.4.2 Energy Corrections . . . . . 65
3.5 Muons . . . . . 68
3.5.1 Muon Reconstruction . . . . . 68
3.5.2 Offline Muon Selection . . . . . 69
3.6 Monte Carlo Simulation . . . . . 75
3.6.1 Generators . . . . . 76
3.6.2 Detector Simulation . . . . . 78

**4 Data Analysis . . . . . 81**
4.1 Online Event Selection . . . . . 82
4.1.1 Trigger Requirements . . . . . 82
4.1.2 $W$ + jets triggers . . . . . 85
4.2 Offline Event Selection . . . . . 87
4.2.1 Inclusive $W \to e\nu$ Events . . . . . 88
4.2.2 Sources of Background in the $W \to e\nu$ Events . . . . . 92
4.2.3 Search for $t\bar{t}$ by Soft Muon Tagging . . . . . 99
4.2.4 Additional Cuts . . . . . 101
4.2.5 Candidate events . . . . . 104
4.3 Backgrounds in $e$ + jets + $\mu$−tag . . . . . 108
4.3.1 QCD Background . . . . . 108
4.3.2 $W$ + jets Background . . . . . 109
4.3.3 Background Summary . . . . . 113
4.4 Signal Efficiency . . . . . 115

4.4.1 Trigger Efficiency . . . . . 116

4.4.2 Offline Efficiency . . . . . 118

4.4.3 Cross Section for $t\bar{t}$ Production . . . . . 120

**5 Conclusion . . . . . 123**

# List of Tables


1.1 Fundamental particles of the Standard Model. . . . . 4

1.2 Branching fractions of $t\bar{t}$ decay channels. . . . . 11

2.1 Muon System Parameters. . . . . 40

3.1 The efficiencies of electron offline cuts. . . . . 62

3.2 Triggers used to study the efficiencies of muon cuts. . . . . 74

3.3 The efficiencies of CF muon offline cuts. . . . . 76

4.1 Summary of two triggers used in the analysis. . . . . 86

4.2 Inclusive jet multiplicity of $W$ candidate events. . . . . 93

4.3 QCD background estimate for $W + 3$ or more jets. . . . . 96

4.4 QCD background estimate for the inclusive $W +$ jets sample. . . . 97

4.5 Summary of kinematic requirements for event selections. . . . . 105

4.6 Characteristics of the 5 top candidate events which pass the Loose Set of cuts. . . . . 106

4.7 QCD background estimate for the inclusive $W +$ jets data sample. 109

4.8 A comparison of the observed number of tagged muons in different samples with the prediction from the muon rate. . . . . 113

4.9 The $W$ + jets background estimate for the inclusive $W$ + jets data sample. . . . . 114

4.10 Summary of different backgrounds to the $t\bar{t}$ signal in the inclusive $W$ + jets data sample. . . . . 115

4.11 Efficiency×branching ratio fraction ($\varepsilon \times Br$) and expected $t\bar{t}$ yields of 74.9 $\mathrm{pb}^{-1}$ data for different top mass. . . . . 119

4.12 Cross section of excess events as a function of different top quark masses. . . . . 122

# List of Figures


1.1 Lowest order QCD processes for $t\bar{t}$ productions. . . . . 9

1.2 Theoretical $t\bar{t}$ production cross section as a function of top quark mass. . . . . 11

1.3 The characteristic of $t\bar{t} \rightarrow e + \text{jets} + \mu-\text{tag}$ channel. . . . . 13

1.4 The Standard Model relation between $m_t$. $M_W$, and $M_H$. . . . . 14

2.1 The view of Fermilab Tevatron Collider. . . . . 16

2.2 A cutaway isometric view of the DØ detector. . . . . 19

2.3 Arrangement of the DØ tracking and transition radiation detectors. 21

2.4 $r$–$\phi$ view of the vertex chamber. . . . . 23

2.5 End view of the central drift chamber. . . . . 24

2.6 The $\Theta$ and $\Phi$ modules of the forward drift chamber. . . . . 25

2.7 Schematic view of a unit cell of the DØ liquid argon calorimeter. . 30

2.8 The cutaway view of the DØ calorimeter. . . . . 31

2.9 Side view of a quarter of the Central Calorimeter and the End Calorimeter. . . . . 32

2.10 Side view of the muon system. . . . . 35

2.11 Variation in the detector thickness in interaction lengths as a function of polar angle. . . . . 36

2.12 The end view of PDT chambers in the B and C layer. . . . . 38

2.13 The cell structure of WAMUS PDT. . . . . 39

2.14 The muon cathode pad. . . . . 39

2.15 Block diagram of the trigger and data acquisition system. . . . . 42

3.1 $\not{E}_T$ resolution as a function of scalar sum of $E_T$. . . . . 51

3.2 The isolation parameter ($f_{iso}$) distribution for electron signals (shaded) and backgrounds (unshaded). . . . . 54

3.3 The distribution of $\chi^2$ for the electron signal sample (shaded) and background sample (unshaded). . . . . 55

3.4 The track match parameter ($\sigma_{trk}$) distribution for electron signals (shaded) and backgrounds (unshaded). . . . . 57

3.5 The $dE/dx$ distribution for electron signals (shaded) and backgrounds (unshaded) in the CDC. . . . . 58

3.6 The EM fraction distribution for electron signals (shaded) and backgrounds (unshaded). . . . . 59

3.7 The invariant mass spectrum for electron pairs (solid dots) with unbiased electron in the CC. . . . . 61

3.8 The jet energy resolution as a function of the average corrected jet $E_T$. . . . . 65

3.9 Energy correction factor for jets as a function of $E_T$ at $\eta = 0$ (upper) and $\eta = 2$ (lower). . . . . 67

3.10 The $\phi$ distribution of muon rate per jet for the pre-shutdown and post-shutdown data. . . . . 72

3.11 The $\eta$ distribution for the pre-shutdown and post-shutdown muons in the second quadrant. . . . . 73

3.12 The $\Delta R_{\mu j}$ distribution of muons with (a) the standard cuts and (b) IFW4 $\geq$2. . . . . 75

4.1 (a) The electron $E_T$ distribution and (b) The $\not{E}_T$ distribution from the $W$ MC (solid line) and $t\bar{t}$ ($m_t = 180$ GeV) MC (dashed line). . 89

4.2 The transverse mass distribution of the $W$ data. . . . . 90

4.3 The $E_T$ of the first 4 leading jets from $t\bar{t}$ MC ($m_t = 180$ GeV). . . 91

4.4 The $E_T$ of the first 4 leading jets from inclusive $W$ events. . . . . 91

4.5 (a) $\eta$ distributions of jets from the $t\bar{t}$ MC (solid line) and inclusive $W$ data (dashed line). (b) The efficiency of $\eta$ cuts for both samples. 92

4.6 $\not{E}_T$ distribution for (a) tight electron events (solid dots), and (b) "fake electron" events (shaded histogram). . . . . 95

4.7 Muon $p_T$ distribution of (a) $t\bar{t}$ MC ($m_t = 180$ GeV) and (b) $W+$jets MC. . . . . 100

4.8 Muon-jet separation ($\Delta R_{\mu j}$) of (a) $t\bar{t}$ MC ($m_t = 180$ GeV) and (b) $W+$jets MC. . . . . 101

4.9 Tagged jet $E_T$ ($E_T^{tag}$) distribution of (a) $t\bar{t}$ MC ($m_t = 180$ GeV) and (b) $W+$jets MC. . . . . 102

4.10 Muon tagging rate per event as a function of $\not{E}_T$. . . . . 103

4.11 The correlation of the angle $\Delta\phi$ between the $\not{E}_T$ and the tagged muon with the $\not{E}_T$ for (a) QCD multijet background events and (b) $W$+jets Monte Carlo. . . . . 104

4.12 $H_T$ distribution of (a) QCD multijet events, (b) $W$ + jets MC, (c) $t\bar{t}$ MC with $m_t = 140$ GeV, and (d) $t\bar{t}$ MC with $m_t = 180$ GeV. . . 105

4.13 Display of event #85129/19079. . . . . 107

4.14 Typical Feynman diagrams contributing to heavy quark production with $W$ bosons: (a) gluon splitting to $b\bar{b}$ pair and (b) single charm production. . . . . 108

4.15 Muon tagging rate per jet as a function of jet $\eta$. . . . . 111

4.16 Muon tagging rate per jet as a function of jet $E_T$. . . . . 112

4.17 (a) $\not{E}_T$ spectra for the sample selected from EM1_ELE_MON trigger and subsample also passing L2 $\not{E}_T$ of 14 GeV threshold. (b) The efficiency of L2 $\not{E}_T$ threshold as a function of offline $\not{E}_T$. 117

4.18 Measured cross section as a function of top quark mass. . . . . 122

5.1 The cross section from the different top search channels. . . . . 124

5.2 The fitted mass distribution for candidate events with the expected mass distributions for top quark events and backgrounds. . . . . 125

# Chapter 1

# Introduction

High energy physics research, or research in particle physics, is an ambitious effort of human beings to determine what are the fundamental constituents of matter, the elementary particles, and what are their interactions. The main objective of particle physics is to establish a complete and simple mathematical model to answer this question. Elementary particles appear to be of two distinct groups. The first group consists of spin $\frac{1}{2}$ particles obeying Fermi-Dirac statistics, knows as "fermions"; this group includes the "quarks" and "leptons." The second group consists of the so-called "bosons"; they have integral spin and obey Bose-Einstein statistics.

We have found three generations of leptons and quarks, listed as follows:

$$\text{lepton} \quad \begin{pmatrix} \nu_e \\ e \end{pmatrix} \quad \begin{pmatrix} \nu_\mu \\ \mu \end{pmatrix} \quad \begin{pmatrix} \nu_\tau \\ \tau \end{pmatrix}$$

$$\text{quark} \quad \begin{pmatrix} u \\ d \end{pmatrix} \quad \begin{pmatrix} c \\ s \end{pmatrix} \quad \begin{pmatrix} t \\ b \end{pmatrix},$$

of which the top ($t$) quark remained unobserved until March 1995 (see section 1.2.2). This thesis presents the analysis of the top search in the $t\bar{t} \rightarrow e + \text{jets} + \mu-\text{tag}$ channel in the data collected at DØ in the 1993-95 running period with a luminosity of $74.9\,\text{pb}^{-1}$.

The structure of this thesis will be to briefly introduce the Standard Model in this chapter, to explain the reason why the top quark was expected to exist, and to describe the different channels in the top quark search. In Chapter 2 we describe the experimental apparatus. In Chapter 3 we explain the reconstruction and identification of particles. The detailed analysis, including the selection of signal, estimation of background, and evaluation of the efficiencies is presented in Chapter 4. The final chapter summarizes the result of the search for the top quark in the DØ experiment.

## 1.1 The Standard Model

The Standard Model [1, 2, 3] is one of the most successful theories of modern physics. One basic concept of the Standard Model is that the forces of nature can be described in terms of local gauge field theories in which the physical equations are invariant under transformations applied independently at each space-time point. It is composed of two similar but distinct quantum theories, quantum chromodynamics (QCD) which describes the nuclear force between quarks, and the electroweak theory (EW) which describes the combination of electromagnetic and weak force. The quanta of these force fields are spin 1 (vector) bosons, the gluons for QCD and the $\gamma$, $W^{\pm}$, and $Z^0$ for

EW [4, 5].

The spin $\frac{1}{2}$ particles of theory are the quarks and leptons. The quarks interact with gluon fields but the leptons do not. The quarks come in different flavors, of which five have been firmly established ($u$, $d$, $s$, $c$, $b$), and the sought after the sixth flavor ($t$ quark) is the topic of this thesis. Each of these flavors carries one of three possible "color charges." There are three charged leptons ($e$, $\mu$, $\tau$) and their corresponding neutrinos ($\nu_e$, $\nu_\mu$, $\nu_\tau$). Table 1.1 lists properties of these quarks and leptons. All quark color charges are equal, i.e., they couple equally to the gluon (QCD) field. The electrically charged particles couple to the electromagnetic field according to their (electric) charge as shown in Table 1.1. All particles couple to the weak field with their (universal) weak charge. An antiparticle exists for each of these particles, with the same mass as its corresponding particle but opposite charge.

An important difference between the QCD field and the electromagnetic (QED) part of the EW field is that the photon does not carry electric charge, but the gluon does carry color charge. QCD is an $SU(3)$ non-Abelian gauge field theory, i.e. the field quanta themselves are a field source, in contrast to QED which is a $U(1)$ Abelian theory. Color provides a mechanism for binding quarks together into hadrons. Hadrons are further classified into mesons (composed of a quark and an antiquark $q\bar{q}$) and baryons (composed of three quarks $qqq$). Hadrons have no net color, i.e. they are color singlets. Since free quarks have never been observed, there must exist a mechanism which confines quarks into hadrons, known as quark confinement. What is really confined is probably color; that would imply that gluons, having color, would also be con-

| Quark (spin $\frac{1}{2}$) | Charge (e) | Mass (MeV) |
|---|---|---|
| $u$ | +2/3 | $2-8$ |
| $d$ | -1/3 | $5-15$ |
| $c$ | +2/3 | $1,000-1,600$ |
| $s$ | -1/3 | $100-300$ |
| $t$ | +2/3 | $\sim 170,000$ |
| $b$ | -1/3 | $4,100-4,500$ |
| **Lepton (spin $\frac{1}{2}$)** | **Charge (e)** | **Mass (MeV)** |
| $e$ | -1 | 0.51 |
| $\nu_e$ | 0 | $< 7.3 \times 10^{-6}$ |
| $\mu$ | -1 | 105.6 |
| $\nu_\mu$ | 0 | $< 0.17$ |
| $\tau$ | -1 | 1,777 |
| $\nu_\tau$ | 0 | $< 24$ |
| **Gauge Boson (spin 1)** | **Charge (e)** | **Mass (MeV)** |
| gluons | 0 | 0 |
| $\gamma$ | 0 | 0 |
| $W^\pm$ | $\pm 1$ | 80,300 |
| $Z$ | 0 | 91,190 |

Table 1.1: Fundamental particles of the Standard Model.

fined. It seems that free color exists inside hadrons where the temperature is between $10^8$ eV and $10^9$ eV, but not outside, where it is about $3 \times 10^{-4}$ eV. It is believed that QCD can offer a possible explanation of confinement, but no formal proof exists.

The electroweak field has the symmetry of the $SU(2) \times U(1)$ gauge group. The left-handed components of lepton or quark pairs of the same family, e.g. $\nu_e$ and $e^-$, $c$ and $s$, transform as doublets under $SU(2)$. They are called weak isospin doublets, with weak isospin $t = 1/2$, and $t_3 = 1/2$ for $\nu_e$ ($c$) and $t_3 = -1/2$ for $e^-$ ($s$). The right-handed components transform as singlets under $SU(2)$; they have $t = 0$ and $t_3 = 0$.

There are four gauge bosons in this theory. Two ($\gamma$, $Z^0$) are electrically neutral and two are charged ($W^+$, $W^-$). The photon is massless, whereas the $Z^0$ ($\sim 91$ GeV) and the $W$ ($\sim 80$ GeV) are massive. This is a case of broken ($SU(2) \times U(1)$) symmetry. Originally the $SU(2)$ part was a $W^i_\mu$, $i = 1,2,3$ field with coupling constant $g_2$ and the $U(1)$ part a $B_\mu$ field, with coupling constant $g_1$. The scalar field, with vacuum expectation value $v$, supposedly broke the symmetry leading to the current four fields and their couplings. The origin of the particle masses is of great interest and may imply the existence of scalar (Higgs) particles — the mass being acquired from the scalar field via the so-called Higgs Mechanism. The EW theory allows for only 3 free parameters corresponding to the original 3, though there are many more observables – $\alpha$, $g_V$, $g_A$, $M_W$, $M_Z$, .... The observables, however, are effected by radiative and QCD corrections, as well as by the masses of top and the Higgs. The consistency of the overconstrained data from LEP at CERN and from SLC

at SLAC with the EW theory has been so spectacular as to enable a correct prediction of the top mass and to set some limits on the Higgs mass. However, the Higgs has not yet been been observed experimentally.

Although the Standard Model successfully describes many aspects of high energy interactions, this model is still incomplete. The fermion part of the Standard Model contains a large number of free parameters, and unification of the strong interaction with the weak and electromagnetic in the same way that the Glashow-Weinberg-Salam model has united the weak and electromagnetic forces has not been successful. Furthermore, gravitational effects must be incorporated into any final theory of elementary particles. As a result, numerous theories of physics beyond the Standard Model have been developed, but so far there is no evidence which has been found to support any new theories.

## 1.2 The Top Quark

### 1.2.1 Why the Top was Expected to Exist

The Standard Model does not predict the number of generation of fermions, but it does require that quarks come in pairs. Thus, since the $b$ quark was discovered [6] in 1977 the existence of a third generation of quarks was indicated, and the search of the $b$'s weak-isospin partner, called the top ($t$) quark, was started. This quark weak isospin doublet was supposed to parallel the third generation weak isospin lepton doublet associated with the $\tau$ lepton discovered in the SLAC data by Perl et al. [7] in 1975.

A strong indication that the top quark has to exist is based on proof that the $b$ quark behaves like a member of a weak isospin doublet with a $SU(2)_L$ electroweak interaction. One way of doing this is to measure the forward-backward asymmetry ($A_{FB}$) in the reaction $e + e- \rightarrow (\gamma, Z) \rightarrow b\bar{b}$. The forward-backward asymmetry is defined as

$$A_{FB} \equiv \frac{\sigma_F - \sigma_B}{\sigma_F + \sigma_B}, \tag{1.1}$$

where $\sigma_F$ and $\sigma_B$ are the cross section of $b$ jets in the forward and backward directions respectively. The contribution to the cross section from the $\gamma$ decay is symmetric about the plane perpendicular to the beamline in the CM frame, but that from the $Z$ is not if the $b$ quark is a $SU(2)_L$ doublet. $A_{FB}$ is proportional to $t_{3L} - t_{3R}$, where $t_{3L}$ and $t_{3R}$ are the third components of left-handed and right-handed isospin respectively. To precisely determine $t_{3L}$ and $t_{3R}$, one can combine the $A_{FB}$ with the measurement of $\Gamma(Z \rightarrow b\bar{b})$, which is proportional to $(t_{3L} + \frac{1}{3}\sin^2\theta_W)^2 + (t_{3R} + \frac{1}{3}\sin^2\theta_W)^2$. The result shows [11]

$$t_{3L} = -0.504^{+0.018}_{-0.011} \tag{1.2}$$

$$t_{3R} = -0.008^{+0.056}_{-0.056}, \tag{1.3}$$

which strongly suggests that the $b$ quark is in a $SU(2)_L$ doublet. Therefore its isospin partner, the $t$ quark, should exist.

### 1.2.2 Discovery of the Top Quark

Searches for the top quark began in the late 1970s. Each search resulted in a higher mass limit for the top quark [8, 9, 10]. In 1993 the DØ collaboration

set the limit on the mass of the top quark at $m_t > 131\,\mathrm{GeV}$ from the 1992-1993 [12] collider run (Run 1A) data. In 1994, the CDF collaboration reported finding evidence of the top quark [13], with a cross section of $13.9^{+6.1}_{-4.8}$ pb, a mass of $174 \pm 10^{+13}_{-12}\,\mathrm{GeV}$, and a significance of 2.8 standard deviations. However, because the excess of signal events was not large enough to rule out background fluctuations, CDF stopped short of claiming discovery.

As mentioned in the discussion of electroweak theory, the mass of the top quark affects fits of the theory to the precision electroweak measurements at LEP and SLC. These results are slightly affected by the unknown Higgs mass ($M_H$). A recent combined fit to 15 measured parameters yields [18]

$$m_t = 178^{+11}_{-11}\,{}^{+18}_{-19}\,\mathrm{GeV}, \tag{1.4}$$

where the central value assumes $M_H = 300\,\mathrm{GeV}$, the first error is due to experimental and theoretical uncertainties, and the second error is determined by varying the Higgs mass from 60 GeV to 1000 GeV.

In 1995, on the basis of more data, both DØ and CDF claimed the discovery of the top quark. DØ reported a cross section of $6.4 \pm 2.2$ pb and a mass of $199^{+19}_{-21} \pm 22\,\mathrm{GeV}$ on the basis of $50\,\mathrm{pb}^{-1}$ [14]. CDF measured a cross section of $6.8^{+3.6}_{-2.4}$ pb and a mass of $176 \pm 8 \pm 10\,\mathrm{GeV}$ on the basis of $67\,\mathrm{pb}^{-1}$ [15]. (The first set of errors comes from statistical uncertainties and the second set of errors from systematic uncertainties.) After many years of searching, we finally established the existence of the top quark. Even with the current data (about $100\,\mathrm{pb}^{-1}$ from Run 1A and Run 1B), the top cross section, mass, and branching ratios to the different decay modes still have large uncertainties. We

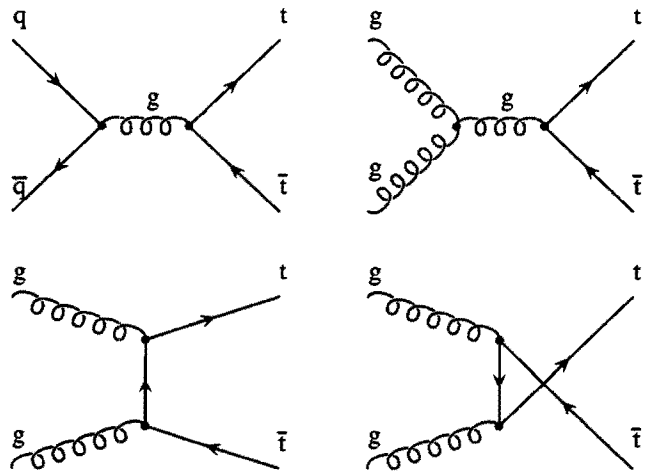


Figure 1.1: Lowest order QCD processes for $t\bar{t}$ productions.

have to improve all these measurements in the future.

### 1.2.3 Production and Decay of the Top Quark

At the Fermilab Tevatron collider, the top production is supposed to be mainly in the form of $t\bar{t}$ pairs, through the $q\bar{q}$ annihilation and gluon fusion diagrams shown in Fig. 1.1. The cross sections of the $t\bar{t}$ production have been calculated using QCD [16]. Fig 1.2 shows this production as a function of top mass.

Because the top quark is heavy, it will decay rapidly with the emission of a real $W$. In the Standard Model, the possible decay modes for $m_t > M_W + m_b$ include

- $t \rightarrow Wb$,
- $t \rightarrow Ws$, and

- $t \rightarrow Wd$.

According to the Cabibbo-Kobayashi-Maskawa matrix elements [17], the branching ratio of the decay $t \rightarrow Wb$ is nearly one hundred percent, and the other two decay modes are negligible.

A $W$ boson can either decay leptonically ($W \rightarrow l\bar{\nu}_l$, where $l$ is $e$, $\mu$, or $\tau$), or hadronically ($W \rightarrow c\bar{s}$ or $W \rightarrow u\bar{d}$). Because of the universality of the coupling strength between $W$ bosons and fermions, the branching ratio of all decay channels are equal. Taking into account the three colors and matching anticolors (the $W$ is colorless) available for each quark pair there are 9 equally probable decay channels for the $W$. The branching fraction of each leptonic decay mode of $W$ bosons is 1/9, and that of each quark decay mode is 3/9. A quark (either a $b$ quark directly from a top decay or other quarks from a $W$ decay) typically produces a localized cluster of hadrons in a small angle, known as "jet." Thus, the decay modes of the individual members of the $W^+W^-$ pair determine three major categories of $t\bar{t}$ events:

- the dilepton channels ($t\bar{t} \rightarrow l_1 l_2 \bar{\nu}_1 \bar{\nu}_2 b\bar{b}$),
- the lepton + jets channels ($t\bar{t} \rightarrow l\bar{\nu}q\bar{q}'b\bar{b}$), and
- the all jets channel.

The branching fractions of these channels are listed in Table 1.2. The $\tau$ poses special problems because of its decay, so its channels do not figure in the following analysis, "lepton" referring only to $e$ and $\mu$. Each of the remaining channels has certain advantages. The dilepton channels have the cleanest sig-

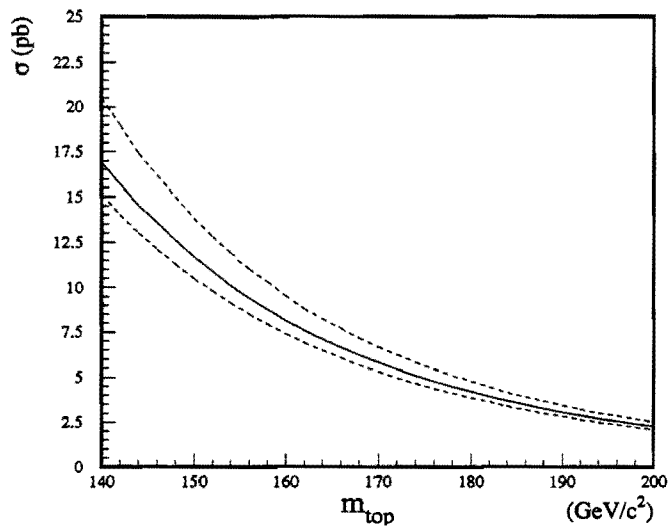


Figure 1.2: Theoretical $t\bar{t}$ production cross section as a function of top quark mass [16]. The lower and upper curves indicate the uncertainty for the central prediction.

| $W$ $W \rightarrow$ $\downarrow$ | $e\nu_e$ (1/9) | $\mu\nu_\mu$ (1/9) | $\tau\nu_\tau$ (1/9) | $q\bar{q}'$ (6/9) |
|---|---|---|---|---|
| $e\nu_e$ (1/9) | 1/81 | 1/81 | 1/81 | 6/81 |
| $\mu\nu_\mu$ (1/9) | 1/81 | 1/81 | 1/81 | 6/81 |
| $\tau\nu_\tau$ (1/9) | 1/81 | 1/81 | 1/81 | 6/81 |
| $q\bar{q}'$ (6/9) | 6/81 | 6/81 | 6/81 | 36/81 |

Table 1.2: Branching fractions of $t\bar{t}$ decay channels.

nal and lowest background but the smallest branching ratio (1/81 for $ee$ or $\mu\mu$, 2/81 for $e\mu$), the all jets channel has the largest branching ratio (36/81) and the worst background, while the lepton plus jets channels have reasonable branching ratios (12/81 for $e+$jets or $\mu+$jets) and a more moderate background.

The focus of this dissertation is on the $e+$jets channel, in which one $W$ boson decays to $e\nu_e$ and the other $W$ boson decays to a pair of quarks that are detected as jets. The background in this mode, which mainly comes from the production of a $W$ accompanied by jets, can be reduced by requiring at least one of the jets to be identified as a $b$ quark. One way to do this is to find a $\mu$ in one of the high $p_T$ jets of the event (so called $\mu-$tag); the fraction of $t\bar{t} \rightarrow e+$jets$+\mu-$tag events can be calculated from the fact that 20% of $b$ quarks will decay to $\mu + X$ so that the two $b$ jets will have at least one $\mu$ in 36% of all cases, and from the fact that the hadronic decaying $W$ will have a jet with a $\mu$ in it from $c$ decay in 5% of all cases. The fraction of $e+$jets containing a $\mu$ will therefore be about 40%, so the $e+$jets$+\mu$-tag channel will contain $40\% \times 12/81 = 6\%$ of all $t\bar{t}$'s produced.

This research has concentrated on finding the selection criteria with the highest efficiency and lowest background for detecting $t\bar{t}$ decays in the $e+$jets$+\mu-$tag channel. We will present in detail the analysis of signal selection, background estimation, and efficiency study for this channel, and then measure the cross section of $t\bar{t}$ production based on the number of observed events and estimated background.

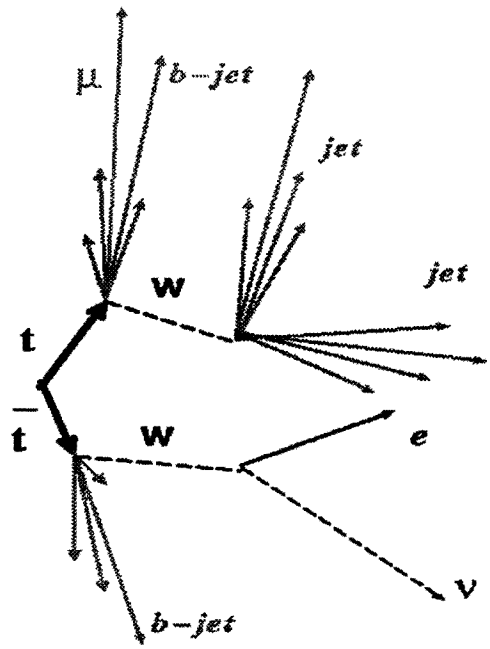


Figure 1.3: The characteristic of $t\bar{t} \rightarrow e + \text{jets} + \mu-\text{tag}$ channel.

### 1.2.4 The Top Quark and New Physics

The discovery of the top quark is again a victory of the Standard Model. Since the mass of the top quark is very heavy and close to the electroweak symmetry breaking scale, it is possible that top quark production will provide an exciting window on new physics. Experimentally, the most important missing ingredient of the Standard Model is the Higgs, which is supposed to give mass to the other particles in the theory. The top mass ($m_t$) can provide constraints on the mass of the Higgs ($M_H$), which is very useful information for the Higgs search, especially when combined with an accurate $W$ mass. The precise measurement of the masses of the top and $W$ will be the major aim of the next DØ run.

Fig 1.4 shows the relation of $m_t$, $M_W$ and $M_H$ [19]. In the next run, the

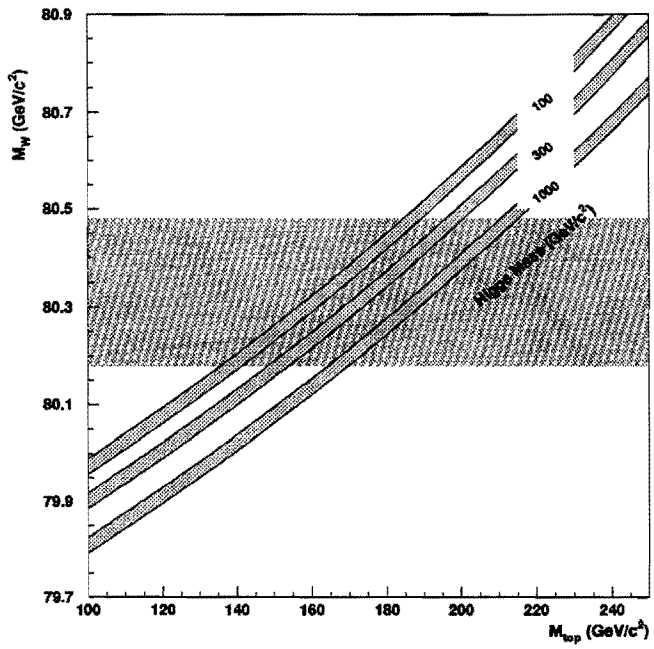


Figure 1.4: The Standard Model relation between $m_t$. $M_W$, and $M_H$. The striped band shows the the current world average $M_W$ and its one standard deviation range.

Tevatron will provide about ten thousand $t\bar{t}$ pairs. The uncertainty of $m_t$ is expected to be improved up to 2-4 GeV, and that of $M_W$ is expected to be around 40 MeV. Hopefully it can help us understand more mysteries in the near future.

# Chapter 2

# Experimental Apparatus

## 2.1 The Fermilab Tevatron

The Fermilab Tevatron is, at present, the highest energy particle accelerator in the world [20, 21]. It consists of a number of accelerators and related systems designed to work together to produce stable particle beams of circulating protons and antiprotons for the desired $p\bar{p}$ collisions at a center of mass energy of 1.8 TeV.

The basic components of the Tevatron are:

- The Cockroft-Walton Pre-Accelerator.
- The Linear Accelerator (LINAC).
- The Booster Synchrotron.
- The Main Ring.
- The Pbar ($\bar{p}$) Storage Rings (including the Debuncher and the Accumulator).

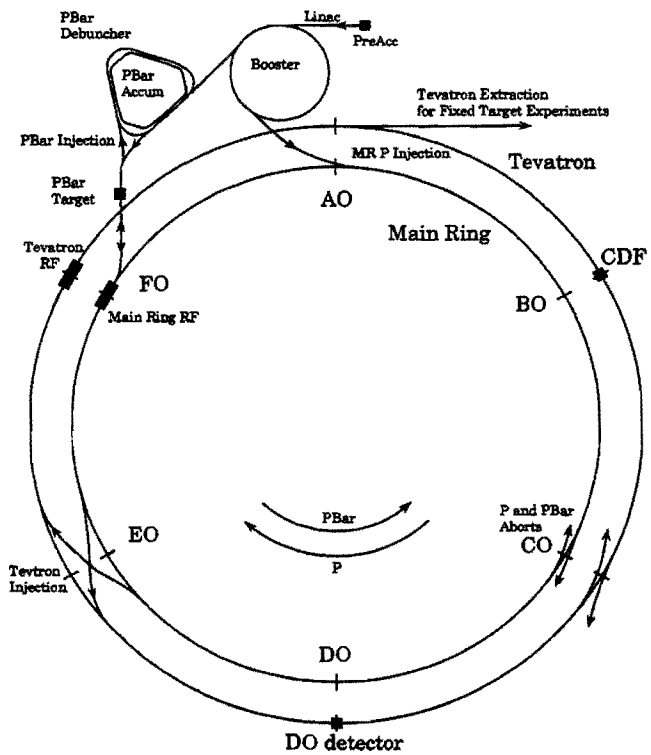


Figure 2.1: The view of Fermilab Tevatron Collider.

- The Tevatron.

Fig. 2.1 shows the basic elements of the Fermilab Tevatron Collider. The beam starts as hydrogen atoms from a DC discharge of hydrogen gas. Electrons are added to the hydrogen atoms thereby producing $H^-$ ions. The $H^-$ ions are introduced into the Pre-Accelerator, which speeds the ions up to an energy of 750 keV. Transport lines then direct the $H^-$ ions into the 150 m long LINAC, which was upgraded just before Run 1B. Within the LINAC, the ions are accelerated to 400 MeV. After leaving the LINAC the ions pass through a carbon foil, which effectively removes all the electrons from the $H^-$ ions, leaving only the hydrogen nuclei (protons). At this point the protons are stored in the Booster Accelerator. Within this synchrotron the protons are bunched

into 84 bunches and accelerated by passing through a series of 18 RF cavities. At the end of the acceleration cycle (about 33 ms long) the protons exit the booster with an energy of 8 GeV. Then the bunched beam is injected into the Main Ring.

The Main Ring is a synchrotron with a radius of 1 kilometer. It has more than 1,000 copper-coiled bending and focusing magnets to provide confinement and stability. Dipole magnets keep the protons travelling in a circular orbit and quadrupole magnets focus the beam into a small cross section. Here the beam is accelerated from 8 GeV to 120 GeV by RF electromagnetic fields. The 120 GeV proton bunches are extracted from the Main Ring and used to bombard a nickel-copper target to produce approximately 21 million antiprotons per batch (84 bunches). The antiprotons are then injected into the Pbar Storage Rings.

The Pbar Storage Ring is comprised of the Debuncher and the Accumulator. The antiproton beam is created with a wide spread in momentum. The Debuncher uses a stochastic cooling technique to narrow the momentum distribution of the antiprotons and to reduce their transverse oscillations as much as possible. This cooling technique was first developed for the $p\bar{p}$ collider at CERN that made the historical discovery of $W, Z$ particles. Pick-up plates sense the average deviation of particles from the desired orbit, and send correction signals across chords to kicker plates in time to adjust the paths of the errant particles. The effect on each cycle is very small, but repeated over a lot of turns, the result is significant.

Approximately 72 billion antiprotons per hour are sent to the Accumulator

after the cooling process. Further cooling takes place in the Accumulator where the density of the antiprotons is increased by a factor of about one million. After a period of 4 to 6 hours the continuous accumulation of antiprotons results in a "store" of about 330 billion antiprotons.

As with the protons, the antiprotons are accelerated in the Main Ring (travelling in a direction opposite to that of the protons) up to an energy of 150 GeV. From the Main Ring both protons and antiprotons are injected into the Tevatron. The Tevatron is located within the same beam tunnel as the Main Ring, about 2 feet below it. It has more than 1000 superconducting magnets that are cooled to a temperature of 4.8° Kelvin by means of a liquid Helium cooling system. These magnets have magnetic fields that are strong enough to keep very high energy particles travelling within the ring. Six bunches of protons (approximately $2 \times 10^{11}$ particles per bunch) and six bunches of antiprotons (approximately $5 \times 10^{10}$ particles per bunch) are accelerated by the RF from 150 GeV to 900 GeV. Once the desired final energy is reached for both proton and antiproton bunches, the two beams are brought together at two beam-crossing stations designated as BØ (CDF) and DØ. A special group of quadrupole magnets (low-beta quadrupoles) are used to focus beams to about $1\,\mathrm{mm}^2$. Beam crossings takes place about once every $3.5\,\mu\mathrm{s}$.

## 2.2 The DØ Detector

The DØ Detector [22] at the Fermilab Tevatron Collider is a large general purpose detector for the study of short-distance phenomena in high energy

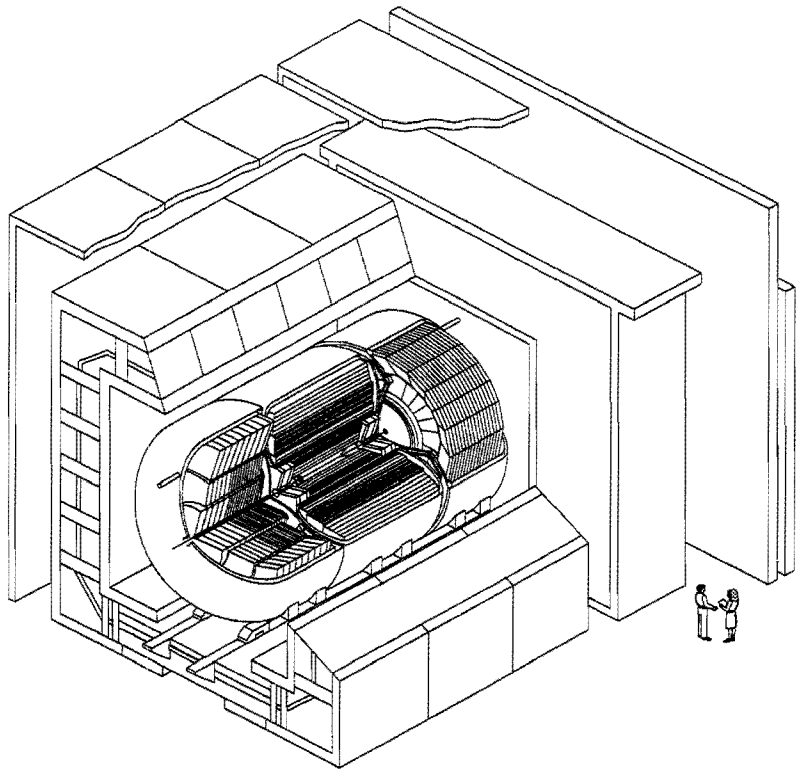

Figure 2.2: A cutaway isometric view of the DØ detector.

proton-antiproton collisions. It is approximately 13 m high, 11 m wide and 17 m long and weighs about 5500 tons. The DØ detector was designed to optimize the following three general goals:

- To provide excellent identification and measurement of electrons and muons.
- To provide good measurement of high $p_T$ parton jets.
- To provide a well-controlled measure of missing transverse energy ($\not{E}_T$) for the detection of neutrinos or other non-interacting particles.

A cutaway isometric view of the DØ detector is shown in Fig. 2.2. The three major subsystems of the detector are:

- The Central Detector.
- The Calorimeter.
- The Muon Detector.

A right handed coordinate system is used at DØ. The positive $z$-axis is along the direction of the proton beam and the $y$-axis is upward. The azimuthal ($\phi$) and polar ($\theta$) angles are defined conventionally, with $\phi = 0$ along the positive $x$-axis and $\theta = 0$ coincident with the positive $z$-axis. The $r$-coordinate denotes the perpendicular distance from the beam axes. Instead of $\theta$, it is convenient to use the pseudorapidity $\eta$, which is defined as

$$\eta \equiv -\ln(\tan\frac{\theta}{2}). \tag{2.1}$$

It approximates the true rapidity

$$y \equiv \frac{1}{2}\ln\left(\frac{E+p_z}{E-p_z}\right), \tag{2.2}$$

for finite angles in the limit that (m/E) $\rightarrow$ 0. Another convenient quantity we often use is "transverse" momentum, the momentum projected onto the plane perpendicular to the beam axis,

$$p_T = p\,\sin\theta\,. \tag{2.3}$$

It is especially useful in collider experiments because the momenta of the escaped partons along the beam pipe and immediately surrounding it can not be measured. However, the transverse momenta of these particles are small. One can apply momentum conservation to the observed $p_T$. Since most of

the $p_T$ is derived from energy measurements in the calorimeter, it is usually presented as "transverse energy", defined by

$$E_T = E \sin\theta \,. \tag{2.4}$$

When treated as a vector, the direction of $E_T$ should be taken to be the same as the $p_T$ vector. The invariant cross section is given by

$$E\frac{d^3\sigma}{dp^3} = \frac{1}{2\pi}\frac{d^2\sigma}{p_T dp_T dy} \simeq \frac{1}{2\pi}\frac{d^2\sigma}{E_T dE_T d\eta} \,. \tag{2.5}$$

Rapidity is thus a natural phase space element. The pseudorapidity $\eta$ is more commonly used because it is only a geometric angular variable and because the masses of the final particles are not usually known and can be neglected compared with their kinetic energies (in the limit $y \to \eta$).

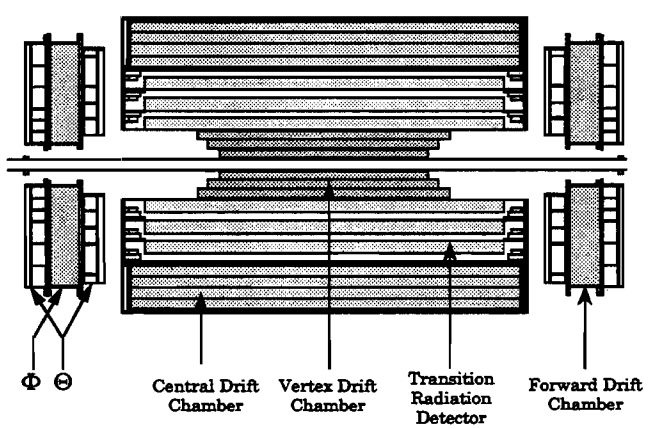


Figure 2.3: Arrangement of the DØ tracking and transition radiation detectors.

## 2.3 Central Detector (CD)

The DØ central detector (CD) consists of the transition radiation detector (TRD) and the DØ tracking system shown in Fig. 2.3. The tracking detectors include

- The Vertex Drift Chamber (VTX).
- The Central Drift Chamber (CDC).
- The two Forward Drift Chambers (FDC).

Because of the absence of a central magnetic field, the momenta of the charged particles are not measured in the tracking system. The goal of the DØ tracking detector is to provide good two-track resolving power, high tracking efficiency for single charged particles, and a good ionization energy measurement to distinguish single electrons from closely-spaced conversion pairs. The TRD is included in order to gain an additional rejection of isolated pions which might otherwise mimic electrons.

### 2.3.1 Vertex Chamber (VTX)

The vertex chamber [22, 23] is the innermost tracking detector in DØ. It has an inner radius of 3.7 cm, just outside the beryllium beam pipe, and an outer active radius of $r = 16.2$ cm. It consists of three concentric layers of cells, as shown in Fig. 2.4. The innermost layer has 16 cells in azimuth, and the outer two layers have 32 cells each. The average drift velocity under normal DØ operating conditions ($< E > \simeq 1\,\mathrm{kV/cm}$) is about $7.3\,\mu\mathrm{m/ns}$. The

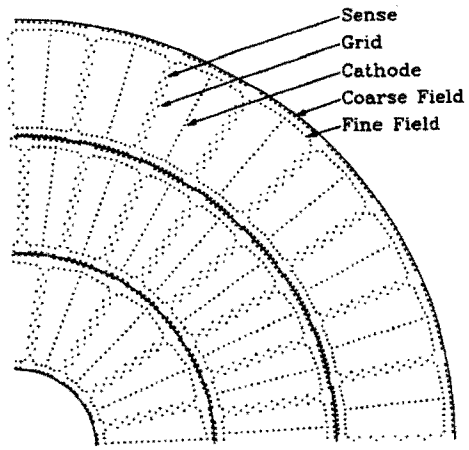


Figure 2.4: $r$–$\phi$ view of the vertex chamber.

$r\phi$ position of a hit is determined from the drift time. The typical resolution is 60 $\mu$m. The $z$ position is determined using a technique called charge division: the resistive sense wire (with a 1.8 k$\Omega$/m resistivity) is read out at both ends and treated as a voltage divider. The average resolution is about 1.5 cm in this direction. The VTX is designed to accurately determine event vertex positions in the transverse plane, especially the secondary vertices arising from $b$ quark. However, because of the high particle flux near the beam pipe, the resolution is not adequate to detect these secondary vertices.

### 2.3.2 Central Drift Chamber (CDC)

The CDC [22, 23] provides coverage for large angle tracks, with $40° < \theta < 140°$, after the TRD and just prior to their entrance into the Central Calorimeter. It is a cylindrical shell of length 184 cm and radii between 49.5 cm and 74.5 cm. It consists of four concentric rings with 32 azimuthal cells per

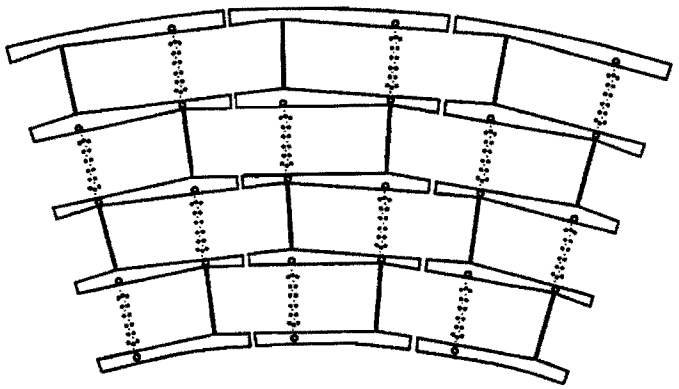

Figure 2.5: End view of the central drift chamber.

ring, as shown in Fig. 2.5. In the middle of each cell, there are 7 sense wires equally spaced in radii at the same $\phi$ coordinate. The wires are parallel to the $z$ axis, and read out at one end. They measure the $\phi$ coordinate of a track. There are two parallel delay lines in each cell, one before the first sense wire and the other after the last sense wire in the cell. Each propagates signals induced from the nearest neighboring sense wires. The signals are read out at the two ends and the difference of two arrival times is used to locate the $z$-coordinate of a track. The $r\phi$ position resolution in the CDC is about 180 $\mu$m and the $z$ resolution is about 3 mm.

### 2.3.3 Forward Drift Chamber (FDC)

The FDC's [22, 23] extend the coverage for charged particle tracking down to $\theta \simeq 5°$ with respect to both emerging beams. They are located at either end of the concentric barrels of the CDC, VTX and TRD and just before the

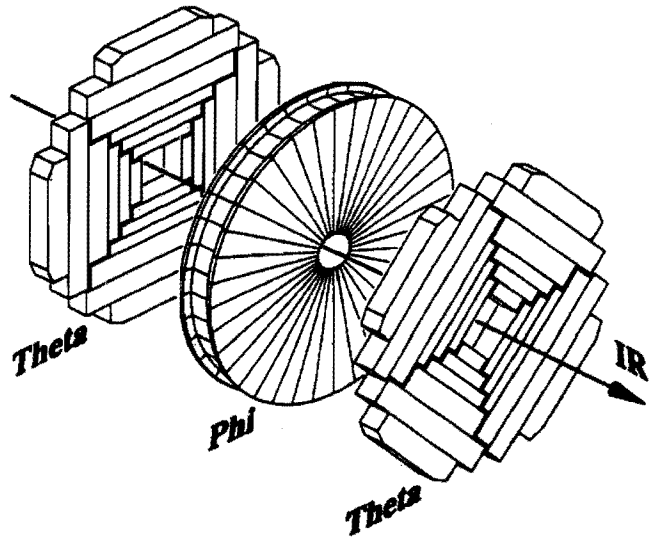


Figure 2.6: The $\Theta$ and $\Phi$ modules of the forward drift chamber.

entrance wall of the end calorimeters. Each FDC package consists of three separate chambers, as shown in Fig. 2.6. The $\Phi$ module has radial sense wires and measures the $\phi$ coordinate. It is sandwiched between a pair of $\Theta$ modules whose sense wires measure the $\theta$ coordinate. The geometric composition of the FDC subcells is more complicated than that of the CDC, but the operating principle is similar. The position resolution is about 200 $\mu$m for $r\phi$ and 300 $\mu$m for $r\theta$.

### 2.3.4 Transition Radiation Detector (TRD)

The TRD [22, 24] is located between the VTX and the CDC. It provides independent electron identification in addition to that given by the calorimeters and the tracking chambers. When highly relativistic charged particles (with $\gamma > 10^3$) traverse boundaries between media with different dielectric constants, transition radiation X-rays are produced on a cone with an open-

ing angle of $1/\gamma$. The energy flux of the radiation is proportional to the $\gamma$. In this way transition radiation detectors can be used to distinguish particles of different mass but of the same energy by means of their $\gamma$ factor. Since the photon emission of a single boundary does not yield detectable signals, transition radiation detectors use many thin foils with gaps between them.

The TRD consists of three separate units, each containing a radiator foil and an X-ray detection chamber. 393 radiator foils in a volume filled with nitrogen gas produce an energy spectrum of X-rays which is determined by the foil thickness and the gaps between the foils. A radial-drift proportional wire chamber (PWC) acts as the X-ray conversion medium and also collects the resulting charge which drifts radially outwards to sense cells. The magnitude and time of arrival of clusters of charge are used to distinguish electrons from hadrons. Each TRD chamber has 256 anode readout channels. The thickness of the full TRD at $\theta = 90°$ is 8.1% of a radiation length and 3.6% of an interaction length. Due to its rather low efficiency, this analysis does not use the TRD information.

## 2.4 Calorimeters

Since there is no central magnetic field in the DØ detector, the calorimeters provide the energy measurement for electrons, photons and jets. In addition, they play an important role in the identification of those objects, and in establishing the transverse energy balance in an event.

A calorimeter is basically a block of matter which intercepts the incident

particles, and it is thick enough to contain all the energy of the subsequent cascade of low energy particles within its volume. Most of the incident energy appears as ionization (or scintillator excitation) in the medium. Finally the ionization (or the scintillation light) is read out electronically.

There are two basic types of particle showers produced by high energy particles: electromagnetic showers and hadronic showers. The former occurs when the incident particle is an electron or photon, and the latter is due to the passage of hadronic particles, like $\pi$ and $K$ mesons or protons and neutrons.

The interaction of electrons and photons in matter at energies well above 10 MeV is characterized by $\gamma$ emission, or bremsstrahlung, and $e^+e^-$ pair production. A parent electron will radiate photons, which convert to pairs, which radiate and produce fresh pairs in turn, the number of particles increasing exponentially until the average particle energy is approximately the critical energy, at which an electron loses the same amounts of energy by radiation and ionization. This process is called electromagnetic (EM) showering. Two important consequences of this multiplicative process are:

- the incident energy is linearly related to the total track length of the particles in the secondary population;
- the depth of the material necessary to reach the shower maximum increases only logarithmically with the energy of the incoming particle.

The longitudinal development of the shower is characterized by the radiation length $X_0$, the mean distance over which a high energy electron drops to $1/e$

of its energy by bremsstrahlung. $X_0$ can be approximated by [17]

$$X_0 = \frac{176.4\,\mathrm{A}}{\mathrm{Z}(\mathrm{Z}+1)\ln(287/\sqrt{\mathrm{Z}})}\ \mathrm{g/cm^2}\,, \tag{2.6}$$

where Z and A are respectively the atomic number and weight of the medium. Electromagnetic shower detectors are mostly built from high-Z materials, (of small $X_0$), which contain the shower in a small volume.

Hadronic showers result from the strong interactions of the incoming particle. In the process, $\pi$ and $K$ mesons are usually produced. A considerable fraction of the particle energy is ultimately transferred to nuclei; the excited nuclei release their energy by emitting nucleons first and then $\gamma$'s as they cascade to the ground state. All the secondary particles lose their kinetic energy through ionization or by inducing nuclear interactions which lead to more secondaries. This cascade process only stops when the energies of the secondaries are so small that they are exhausted by ionization energy loss or absorbed in a nuclear process. Since such interactions usually have a cross section much smaller than the EM cross section and involve higher $p_T$ transfers, there is a much greater lateral and longitudinal distribution of energies compared to an EM shower. Also, the much larger variety of interaction processes implies much larger fluctuations in the shower development compared to the pure EM shower. Therefore, the energy resolution for strongly interacting particle is worse. The hadronic shower dimension is governed by the nuclear interaction length $\lambda$, which is related to the total hadronic cross section, which ranges between 40 and 100 mb. The interaction length is given approximately by the formula $\lambda = 35\,\mathrm{A}^{1/3}\,\mathrm{g/cm^2}$ [17].

The scales of the profiles for electron and hadron showers are very different, the hadronic shower being much longer and broader. The differences may be used to distinguish electrons and photons from hadrons, and it works best for high-Z materials, because the ratio between $\lambda$ and $X_0$ increases almost linearly with the Z. For instance, uranium has $X_0 = 6.0\,\mathrm{g/cm^2}$ and $\lambda = 199\,\mathrm{g/cm^2}$. As a result, electromagnetic showers in uranium will reach their maximum well before the development of hadronic showers.

Based on considerations of size and cost, a sampling calorimeter, as opposed to a total absorption calorimeter such as NaI crystals, is used quite frequently for high energy particles. The usual configuration is a stack of many plates of dense metallic absorber, interleaved with planes of sensitive material. In sampling calorimeters one measures the ionization loss of shower particles that traverse a sensitive layer. This is just a small fraction of the total ionization, usually somewhere in the $1\% - 10\%$ range, but should be a fixed fraction of it. This fixed fraction is called the sampling fraction and is to first order equal to the mass ratio of the sensitive to the absorbing materials in the calorimeter.

The DØ calorimeters [22, 25, 26] use liquid argon as the sensitive layer to sample the ionization produced in electromagnetic and hadronic showers, and uranium/copper as the absorber. The major factors for this choice are the proven ability of liquid argon calorimeters to perform reliably and stably, the high density afforded by the combination of uranium and thin argon gaps, the radiation hardness, and the superior performance in terms of energy resolution and the equalization of response to hadronic and electromagnetic

particles. Liquid argon also has the property of unit gain and relative simplicity of calibration, the flexibility in segmenting the calorimeter into transverse and longitudinal cells and the relatively low unit cost for readout electronics.

The choice of liquid argon, however, brings about the complications of cryogenic systems. The DØ calorimeters consist of three components as shown in Figure 2.8: the central calorimeter (CC) and a pair of end calorimeters (ECN and ECS), each contained in massive vessels (cryostats). There are three distinct types of modules in both the CC and the EC:

- An electromagnetic section (EM), with relatively thin uranium absorber plates (3-4 mm) to measure the energy of particles such as electrons or photons which mainly interact with the matter electromagnetically.
- A fine-hadronic section (FH), with thicker uranium absorber plates (6 mm).
- A coarse-hadronic section (CH), with thick copper or stainless steel plates (46.5 mm).

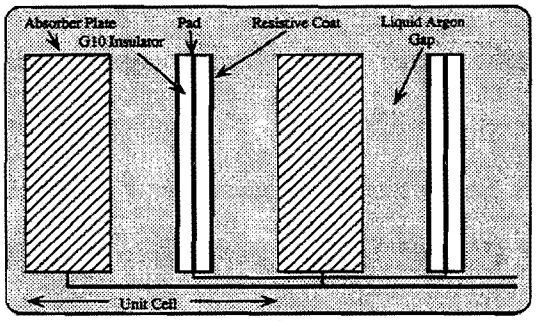


Figure 2.7: Schematic view of a unit cell of the DØ liquid argon calorimeter.

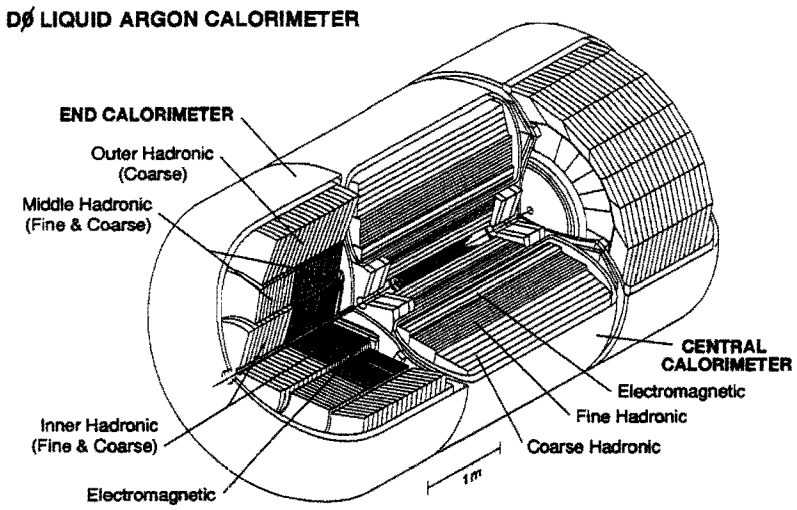


Figure 2.8: The cutaway view of the DØ calorimeter.

Each calorimeter cell contains liquid argon gaps, absorber plates and readout boards, as shown in Fig. 2.7. Each liquid argon gap is between a grounded absorber plate and a readout board. A board is made of two 0.5 mm sheets laminated together; the inner surface of one sheet is bare G-10 and the inner surface of the other is copper-clad and is milled to the desired pattern of pads. The outer surfaces of the board are coated with a resistive epoxy. The resistive surfaces are at a positive high voltage (2.0-2.5 kV) so that charges can collect on them and induce charges on the pads of the readout board. The pads with the same $\eta$ and $\phi$ are ganged together in the longitudinal direction to form a readout cell. Both the CC and EC are segmented into pseudo-projective towers (see Fig. 2.9) with $\Delta\phi \times \Delta\eta = 0.1 \times 0.1$. The calorimeter is divided into many layers along the particle trajectory direction in order to provide a good measurement of the energy shower profile. In the third layer of the electromagnetic (EM) calorimeter, where the EM shower maximum is expected, the $\Delta\eta$ and $\Delta\phi$ segment is $0.05 \times 0.05$ instead of the normal

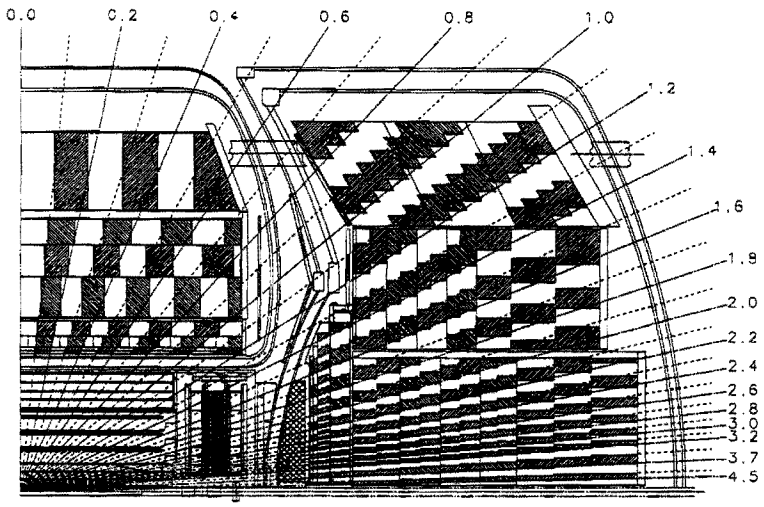


Figure 2.9: Side view of a quarter of the Central Calorimeter and the End Calorimeter.

$0.1 \times 0.1$ segment, improving the spatial resolution for electrons and photons. The electron energy resolution of the EM calorimeter was well measured in a test beam at Fermilab and was parameterized as:

$$(\frac{\sigma}{E})^2 = C^2 + (\frac{S}{\sqrt{E}})^2 + (\frac{N}{E})^2 \ , \tag{2.7}$$

where $C = (0.3 \pm 0.2)\%$, $S = (15.7 \pm 0.5)\% \sqrt{\text{GeV}}$ and $N = 0.140\,\text{GeV}$ [22]. The response is also known to be linear with energy to better than 0.3% for electron energies $E > 10\,\text{GeV}$. The DØ calorimeter also has good containment of shower energy. At $\eta = 0$, the central calorimeter has a total of 7.2 nuclear absorption lengths; at the smallest angle of the end calorimeter, the total is 10.3 nuclear absorption lengths.

### 2.4.1 The Central Calorimeter (CC)

The central calorimeter comprises three concentric cylindrical shells and covers roughly the range of $|\eta| \leq 1.1$. There are 32 azimuthally distributed EM modules in the inner ring, 16 fine hadronic in the surrounding ring and 16 coarse hadronic modules in the outer ring. To reduce the energy loss in the crack the EM, FH and CH module boundaries are rotated so that no projective ray encounters more than one intermodule gap. The EM modules contain four longitudinal sections of 2.0, 2.0, 6.8 and 9.8 radiation lengths ($X_0$). The FH modules contain three longitudinal sections of 1.3, 1.0 and 0.9 interaction lengths ($\lambda$). The CH modules contain just one depth segment of 3.2 $\lambda$.

### 2.4.2 The End Calorimeter (EC)

The EC extends to $|\eta| = 4$. There are two mirror-image end calorimeters (ECN and ECS) which contain four module types: one EM module, one inner hadronic (IH) module, 16 middle and outer hadronic (MH and OH) modules. The ECEM modules contain four readout sections of 0.3, 2.6, 7.9 and 9.3 $X_0$. The material in front of the cryostat brings the total absorber for the first section up to about 2 $X_0$. The ECIH modules are cylindrical. The fine hadronic part contains four readout sections with 1.1 $\lambda$ for each one and the coarse part has a single readout section with 4.1 $\lambda$. Each of the ECMH modules has four uranium fine-hadronic sections of about 0.9 $\lambda$ and single stainless steel coarse-hadronic section of 4.4 $\lambda$. The ECOH are all stainless

steel coarse-hadronic modules with the absorber plates inclined at an angle of about $60^o$ with respect to the $z$ axis.

### 2.4.3 Intercryostat Detectors and Massless Gaps

The region of $0.8 \leq |\eta| \leq 1.4$ contains a large amount of uninstrumented material in the form of cryostat walls, stiffening rings and module endplates. The material profile along a particle path varies with rapidity through this region. Two scintillation counter arrays called intercryostat detectors (ICD) were built to correct for the energy deposited in the uninstrumented walls. In addition, separate readout cells called massless gaps are installed in both the CC and EC calorimeters. One ring with the standard segmentation is mounted on the end plates of the CCFH modules. Additional rings are mounted on the front plates of both the ECMH and the ECOH modules. Each massless gap detector consists of three liquid argon gaps with two readout boards without any absorber plates. These massless gaps together with the ICD provide an approximation to the sampling of EM showers.

## 2.5 Muon Detector

The muon detecting system [22, 27, 28, 29] consists of five separate solid-iron toroidal magnets, together with sets of proportional drift tube chambers (PDT) to measure track coordinates down to approximately 3°. The calorimeter absorbs most of the electromagnetic and hadronic showers, so hits in these chambers are mainly due to muons or background sources from outside of the

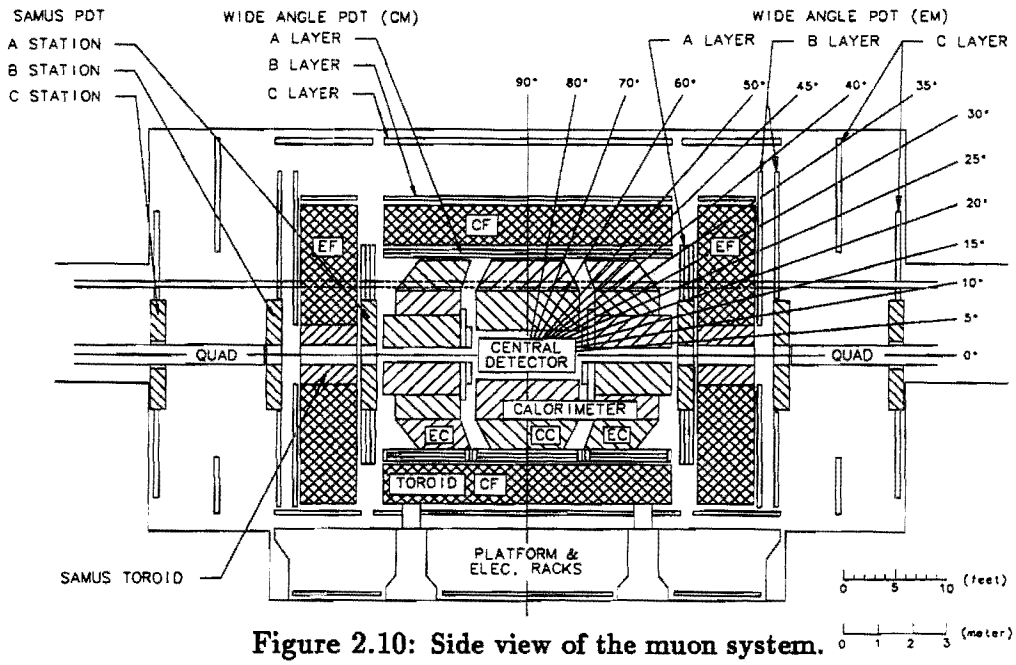


Figure 2.10: Side view of the muon system.

detector (e.g., beam halo, cosmic ray). The large number of interaction lengths of the calorimeter and muon toroids shown in Fig. 2.11 provide a clean environment for the identification of muons with negligible punchthrough probability.

Fig. 2.10 shows the DØ detector with five toroids and their associated PDT layers. The magnetic fields produced by the toroids are approximately along the $\hat{\phi}$ direction, so particles are bent in $r$–$z$ plane. The first layer of PDTs (known as the A-layer) is inside the toroids to measure the incident trajectories of particles. The other two layers (B and C-layers) are arranged outside the bend to measure the exit trajectories; thus the muon momentum can be obtained from the deflection of the track in the magnetic fields. Because of multiple Coulomb scattering in the iron toroids, the relative muon momentum resolution is greater than 18%.

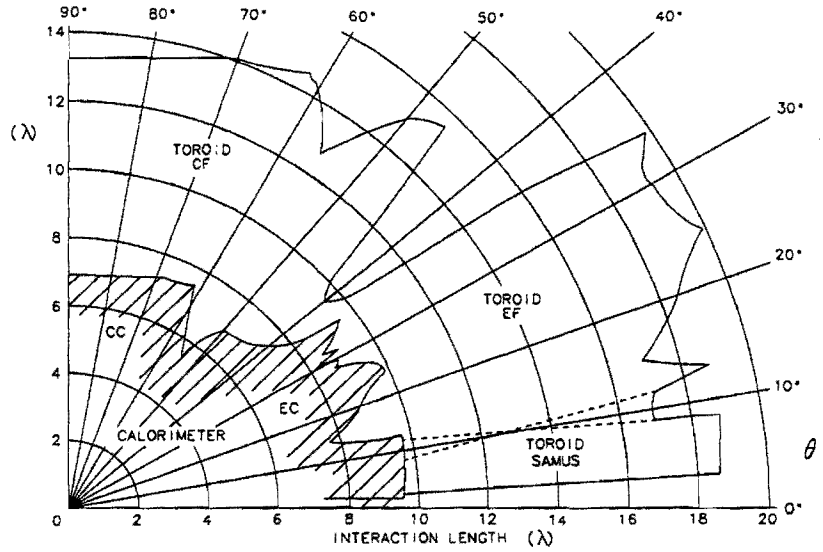


Figure 2.11: Variation in the detector thickness in interaction lengths as a function of polar angle.

### 2.5.1 The Muon Toroids

The five toroids consist of one central toroid (CF), covering the central pseudorapidity region up to $|\eta| < 1.0$, two end toroids (EF), covering the range $1.0 < |\eta| < 2.5$, and two small angle toroids (SAMUS), fitting the central holes of the EF toroids and extending the muon coverage over the region of $2.5 < |\eta| < 3.3$.

The CF toroid is centered on the Tevatron beam line. It is a square annulus 109 cm thick and weighing 1973 metric tons. The distance from the beam to the inner surface of the CF toroid is 317.5 cm. The CF toroid is built out of three different pieces. The bottom piece is fixed to the detector platform and helps provide support for the enclosed tracking and calorimeter systems. The remainder of the CF toroid is composed of two C-shaped shells which may be split apart to allow access to the interior detectors. Internal

fields of about 1.9 Tesla are excited by twenty coils of 10 turns each carrying 2500 A currents.

The two EF toroids are located at $447 < |z| < 600$ cm. They have 183 cm by 183 cm square inner holes centered on the beam line. Fields of approximately 2 Tesla are induced in the EF toroids by eight coils with 8 turns each carrying a current of 2500 A.

The square inner hole of each EF toroid contains a small angle (SAMUS) toroid. Each SAMUS toroid weighs 32 metric tons, has outer surfaces at 170 cm from the beam axis and a 102 cm squared inner hole through which the beam pipe can pass. Two coils of 25 turns each carry currents of 1000 A. Tungsten-Lead collimators fill the space between the SAMUS toroids and the Tevatron beam pipe.

### 2.5.2 Wide Angle Muon System (WAMUS)

The wide angle muon system (WAMUS) consists of the CF and EF toroids and a collection of WAMUS chambers. The WAMUS chambers are arranged in three layers. The A-layer chambers are inside the toroids, and the B and C-layer chambers are outside the toroids. In order to get a good measure of the muon track after it exits the toroids, the B and C-layers are separated by $\geq 1$ m.

There are four planes of PDT cells in each A-layer and three planes in the B and C-layer chambers. The cell structure for all WAMUS PDTs is the same. There are 164 WAMUS chambers differing only in the number of

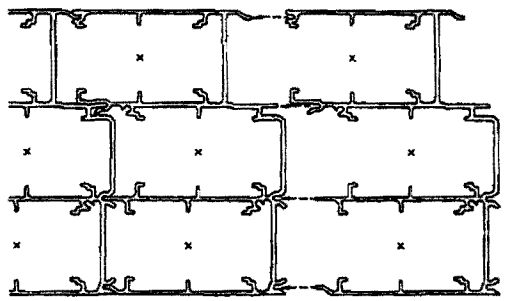

Figure 2.12: The end view of PDT chambers in the B and C layer. The A layer chambers are similar, but have four planes instead of three.

PDT planes, width, and length. WAMUS PDTs are formed from aluminum extrusion unit cells which are cut to the appropriate lengths and then press-fitted together. Fig. 2.12 shows a transverse offset between planes of PDTs that helps resolve left-right drift-time ambiguities. Fig. 2.13 shows the basic interior construction of a WAMUS PDT. Two cathode pad strips are inserted into the top and bottom of each cell. Gold-plated tungsten anode wires are held near the center of each cell. The maximum drift distance is 5 cm. The drift time allows us to calculate the drift distance and determines the bend coordinate. Its resolution is about 500 $\mu$m.

The PDTs are mounted roughly parallel to the magnetic field (along $\hat{\phi}$ direction) so that the bend of a muon track will occur in the drift coordinate ($\sim \theta$ coordinate) for a better measurement. The coordinate ($\xi$) along the wire direction (non-bend) is measured by a combination of cathode pad signals induced by the anode pulse, and timing information from the anode wire. The anode wires for adjacent cells are jumpered together at one end in order to simplify chamber electronics. First the coarse measurement of the $\xi$ is derived

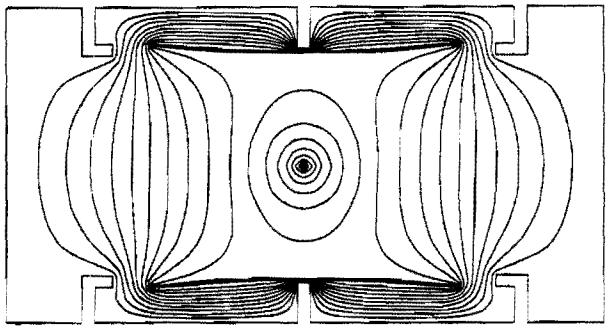

Figure 2.13: The cell structure of WAMUS PDT, with the electric equipotential lines shown.

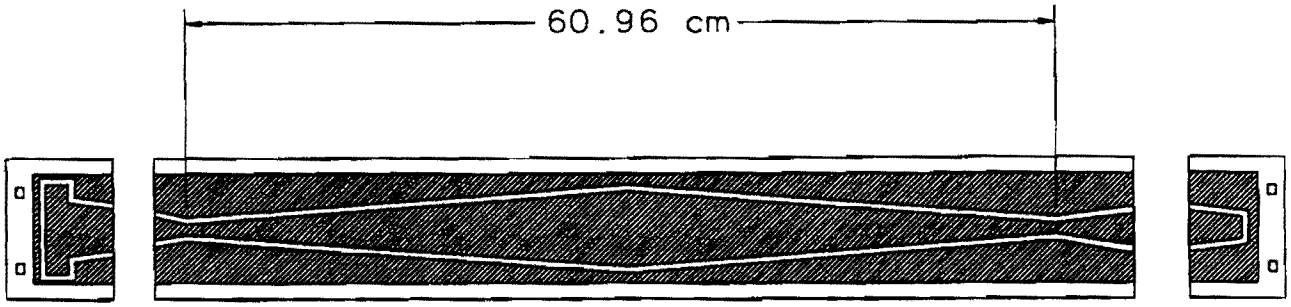


Figure 2.14: The muon cathode pad.

from the time difference for a particular anode signal from the two ends of the paired wire. The $\xi$ coordinate resolution from this $\Delta t$ information varies from 10 cm to 30 cm along the wire. A more precise measurement is obtained by the cathode pad signals, which consist of inner and outer electrodes with a repeating diamond pattern as shown in Fig. 2.14. The ratio of sum and difference of inner and outer signals gives a $\xi$ resolution of approximately 1 cm.

| | WAMUS | SAMUS |
|---|---|---|
| Rapidity coverage | $\|\eta\| \leq 1.7$ | $1.7 \leq \|\eta\| \leq 3.6$ |
| Magnetic Field | 2 T | 2 T |
| Number of Chambers | 164 | 6 |
| Interaction lengths | 13.4 | 18.7 |
| Bend view resolution | $\pm 0.9$ mm | $\pm 0.35$ mm |
| Non-bend resolution | $\pm 10$ mm | $\pm 0.35$ mm |
| Gas | Ar 90%,$CF_4$ 6%,$CO_2$ 4% | $CF_4$ 90%,$CH_4$ 10% |
| Avg. Drift Velocity | 6.5 cm/$\mu$s | 9.7 cm/$\mu$s |
| Anode Wire Voltage | +4.56 kV | +4.0 kV |
| Cathode Pad Voltage | +2.3 kV | – |
| Number of cells | 11,386 | 5308 |

Table 2.1: Muon System Parameters.

### 2.5.3 Small Angle Muon System (SAMUS)

The small angle muon system (SAMUS) consists of two SAMUS toroids and a collection of SAMUS chambers. The SAMUS chambers cover the pseudorapidity region $2.5 < |\eta| < 3.5$. As with WAMUS, the SAMUS chambers are also arranged into three layers called stations. A-stations precede the SAMUS toroids, with B and C-stations placed after the SAMUS toroids. The SAMUS stations cover an area of $312 \times 312\,\mathrm{cm}^2$ perpendicular to the beam direction. A 61 (86) cm interior square hole permits the passage of the beam pipe in the A and B (or C) stations. Each station consists of three planes of cylindrical proportional drift tubes. Each plane in turn is segmented into two half-planes or doublets. The tubes in a given plane are oriented along the x,y, and u directions (u being at 45 degrees with respect to x and y). Adjacent tubes are offset by one half a tube diameter. The SAMUS system contains a total of 5308 tubes. Anode wires are gold-plated tungsten and are tensioned to 208 g. The maximum drift time is 150 ns. As with WAMUS, the drift time to drift distance is approximately linear. The resolution of a single drift tube is approximately $350\,\mu$m. The signal processing and digitization is similar to that employed for WAMUS. Further details of the muon system are listed in Table 2.1.

## 2.6 Triggering and Data Acquisition

The DØ trigger and data acquisition systems are designed to select and record interesting physics and calibration events efficiently. The trigger has

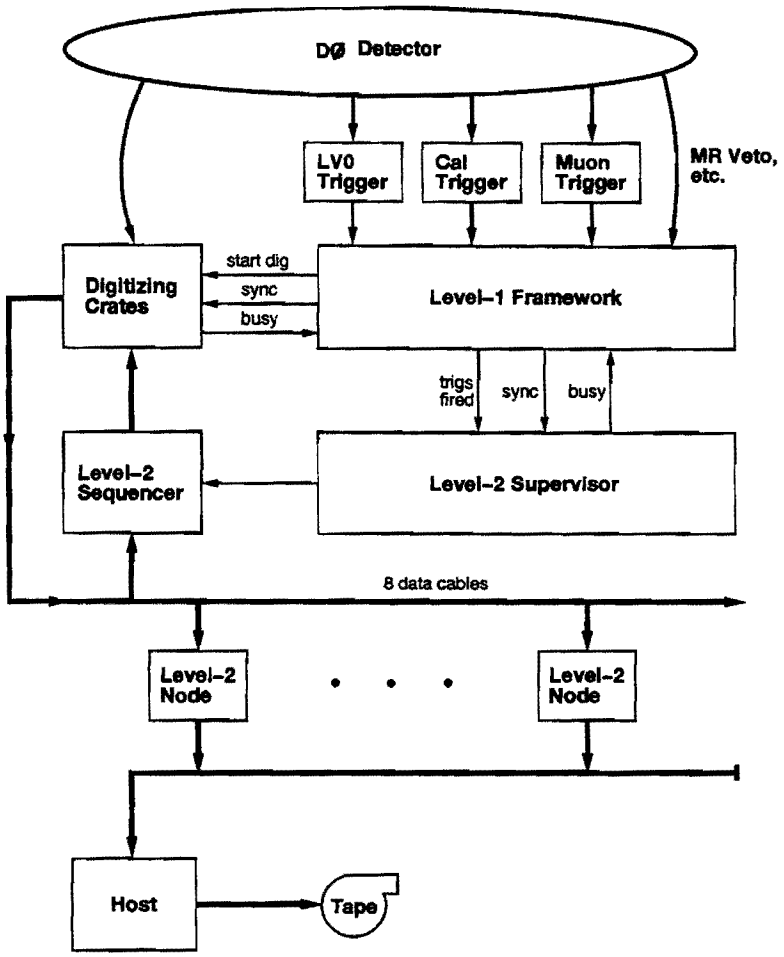


Figure 2.15: Block diagram of the trigger and data acquisition system.

three levels of increasingly sophisticated event characterization. At a typical luminosity of $\mathcal{L} = 1.6 \times 10^{31}\,\mathrm{cm}^{-2}\mathrm{s}^{-1}$, the level 0 rate is about 150 KHz. The Level 1 reduces the rate to 200 Hz because that is the full capacity of the Level 2 processors. Then the Level 2 software reduces the event rate further down to 2 Hz and the events are written out to long-term storage devices (8 mm tapes) in real time.

### 2.6.1 Level 0

Level 0 [22, 30] is a scintillator-based trigger designed to register the presence of inelastic collisions and serves also as the luminosity monitor. It uses two hodoscopes of scintillation counters mounted on the front surfaces of the end calorimeters. These hodoscopes have an array of counters inscribed in a 45 cm radius circle to give partial coverage for the rapidity range $1.9 \leq \eta \leq 4.3$ and nearly full coverage for $2.3 \leq \eta \leq 3.9$. This rapidity coverage is set by the requirement that a coincidence of both Level 0 detectors be $\geq 99\%$ efficient in detecting non-diffractive inelastic collisions.

The difference in the arrival time of particles to the detectors at both ends is used to determine the $z$-coordinate of the collision point. Although most of the collisions happen near $z = 0$, the large spread of the collision vertex distribution ($\sigma \simeq 30\,\text{cm}$ gaussian) can introduce a large error in the $E_T$ calculation. At high luminosity, the probability of multiple interactions is sizable. When the multiple interactions are present, the time difference information from Level 0 is ambiguous and a flag is set to identify these events for the subsequent trigger levels.

### 2.6.2 Level 1

Level 1 [22, 31, 32] is a collection of hardware trigger elements arranged in a flexible software driven architecture that allows for easy modification. All Level 1 triggers operate within the $3.5\,\mu s$ time interval between beam crossings and they have to complete their work in this short period and thus

contribute no dead time. The framework gathers digital information from each of the specific Level 1 trigger devices and selects a particular event for further examination. Specific trigger selection is performed by a 2-dimensional AND-OR network. 256 latched bits called AND-OR Input Terms which carry specific pieces of detector information such as one calorimeter cluster over 10 GeV, form one set of inputs to the AND-OR network. The 32 orthogonal AND-OR lines corresponding to 32 specific Level 1 triggers are the outputs of the AND-OR Network. Each of these triggers is defined by a pattern indicating, for every AND-OR Input Term, whether that term is required to be asserted, negated or ignored. Satisfaction of one or more specific trigger requirements results in a request for the readout of the full event data by the data acquisition hardware if free from front-end busy restrictions or other vetoes.

Of specific interest for this thesis is the Level 1 calorimeter trigger. The system operates on analog trigger pickoffs from the calorimeter signal shaping and processing electronics and the energy signals are summed into $\Delta\eta \times \Delta\phi = 0.2 \times 0.2$ trigger towers up to $\eta = 4$ for both EM and Hadronic sections. It uses the $z$-vertex information provided by the Level 0 trigger and several fast lookup memories to calculate the EM and hadronic transverse energies and their $x$ and $y$ components for each trigger tower above a certain threshold.

Level 1.5 trigger [34, 35] has been implemented to reduce the event rate input to Level 2 by a factor of 10-20, and to further confirm the fast Level 1 decision. Level 1.5 is an intermediate hardware trigger which is only used to examine muons and calorimeter EM candidates from level 1. If an event fails selection Level 1.5 criteria, the read-out is aborted. The average event rate

into Level 2 is about 200 Hz.

### 2.6.3 Level 2

Candidates from Level 1 are passed through the standard DØ data acquisition pathways to a farm of microprocessors which serve as Level 2 trigger systems [22, 33] as well as event builders. Sophisticated software algorithms resident in the Level 2 processors reduce the output rate to 2 Hz before passing events on to the host computer for event monitoring and recording on tape. There are 48 software event-filtering nodes in the Level 2 system. The VAX-ELN filtering process in each node is built around a series of filter tools. Each tool has a specific function related to the identification of a type of particle or an event characteristic. The interesting ones for this thesis are those for jets, calorimeter EM clusters and $\not{E}_T$. The events passing Level 2 filters are recorded on 8 mm tapes and are available for reconstruction and analysis.

# Chapter 3

# Event Reconstruction and MC Simulation

Raw data consist of digitized electronic signals from different parts of the DØ detector. These signals are produced by particles that are the final products of individual collisions ("events"). The first step of the data analysis is to correlate all the signals from the passage or absorption of each final particle and then use that information to determine as much as possible about that particle's 4-vector. This process is called "reconstruction." In some cases the information from final products of the collision is used to reconstruct the 4-vectors of the particles that decay to them.

The DØ standard reconstruction package DØRECO (containing about 150,000 lines of Fortran code) uses the raw signals to find energy clusters in the calorimeters, and charged particle trajectories in the drift chambers and transition radiation detectors. From these data DØRECO determines the event vertex, and provides preliminary identification of electrons, photons, muons, taus, jets, and $\not{E}_T$ (neutrinos). Since there are always some uncertainties in the identification, DØRECO stores possible candidates and necessary

information in "banks" to allow users to do a better determination. The banks connect to each other to form a hierarchical tree structure so that users can go through these links to find the required information from the appropriate bank. For the work reported in this thesis, the DØRECO package version 12 has been used for the analysis.

## 3.1 Event Vertex

The event vertex information is very important for reconstructing electrons, muons or jets. DØRECO determines the event vertex in the following steps:

- Tracks in the Central Drift Chamber (CDC) are reconstructed, and extrapolated to the center of the detector.
- The $z$-positions of the intersection of each track with the beam axis ($z$-axis) are then histogrammed.
- The above distribution is fitted to a gaussian function and the mean of the $z$-position is taken as the vertex.

The resolution of the vertex $z$-position is about 1-2 cm depending on the number of reconstructed tracks associated with it. Multiple vertices can typically be separated if they are at least 7 cm apart [36].

## 3.2 Missing Transverse Energy

The original "signature" of neutrinos in nuclear beta decay was missing energy and angular momentum, missing momentum not being used until later in the determination of the helicity of the neutrino. In the Tevatron the situation is reversed — the energy in the (hard) parton-parton collision is not known and it is impossible to sum up the angular momenta of the multitude of emitted particles, so only missing momentum is left to identify neutrinos. The original longitudinal momenta of the colliding partons are not known but their transverse momenta are expected to be only of the order of a GeV, so a large missing transverse momentum is the neutrino signature.

The missing transverse momentum is determined essentially from energy deposits in the calorimeters, so it is referred to as missing transverse energy, $\not{E}_T$, as if energy were a vector.

During the data taking, charge is collected by each calorimeter cell and digitized by the readout system as raw ADC counts. The DØRECO converts ADC counts into energies using the calorimeter calibration constants. Then the transverse momenta (or transverse energies) deposited in a cell can be calculated as

$$p_x = E_x = E \sin\theta \cos\phi \,, \tag{3.1}$$

$$p_y = E_y = E \sin\theta \sin\phi \,, \tag{3.2}$$

where $E$ is the energy deposited in the cell with $\theta$ and $\phi$ as the polar and azimuthal angles respectively. The missing transverse energy, by definition, is

the negative value of the total transverse momenta:

$$\not{E}_x = -\sum_i p_{x,i} = -\sum_i E_i \sin\theta_i \cos\phi_i \,, \tag{3.3}$$

$$\not{E}_y = -\sum_i p_{y,i} = -\sum_i E_i \sin\theta_i \sin\phi_i \,, \tag{3.4}$$

and the magnitude is calculated as

$$\not{E}_T = \sqrt{\not{E}_x^{\,2} + \not{E}_y^{\,2}} \,. \tag{3.5}$$

The sum is over all cells in the calorimeter and the intercryostat detectors (ICD). High $p_T$ muons deposit only a fraction of their energy in the calorimeters and therefore contribute to $\not{E}_T$. To make sure that $\not{E}_T$ is properly used as a measurement of neutrinos we make some special cuts on the azimuthal angle ($\phi$) between the $\not{E}_T$ and the muon. The details will be discussed in the next chapter.

Since the $\not{E}_T$ is the sum over all objects in the calorimeter, the mismeasurement of any object in an event affects its value. So, whatever correction is made to electrons and jets, the corresponding correction is made to the $\not{E}_T$ by adding the $E_T$ correction of each object to the $\not{E}_T$ vectorially.

The $\not{E}_T$ resolution has been studied using the minimum bias (inclusive inelastic) data sample. Since the cross section of minimum bias events ($\sim$ 48 mb) is much higher than that of any process involving high $p_T$ neutrinos or muons in the final state, large $\not{E}_T$ in these events will be considered as a mismeasurement. The resolution is parameterized as

$$\sigma_{\not{E}_T} = a + b \cdot \tilde{E}_T \,, \tag{3.6}$$

where $a$ is a constant term which represents the average transverse energy leak in the beam direction, and $\tilde{E}_T$ is the scalar sum of transverse energies defined as

$$\tilde{E}_T = \sum_i E_i \sin\theta_i \ . \tag{3.7}$$

We obtained $a = 1.08\,\mathrm{GeV}$ and $b = 0.019$ [37].

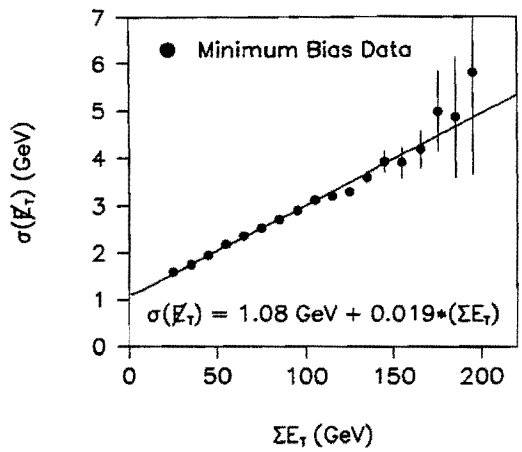


Figure 3.1: $\not{E}_T$ resolution as a function of scalar sum of $E_T$.

## 3.3 Electrons

### 3.3.1 Reconstruction of Electrons and Photons

Electrons and photons deposit almost all of their energy in the electromagnetic calorimeters. During the event reconstruction phase, the energy in each $\Delta\eta \times \Delta\phi = 0.1 \times 0.1$ tower is calculated by summing up energies in all the electromagnetic (EM) and the first hadronic (FH1) cells in a tower.

Clusters are formed by using the "nearest neighbor" algorithm. This algorithm tries to connect every tower in the calorimeter with the highest

energy tower in its local neighborhood, which consists of $3 \times 3$ towers in $\eta$–$\phi$ space, centered on it. If the energy in that neighboring tower is higher than a 50 MeV threshold, the two towers are considered to be associated with each other. After all the towers are looped over, each set of towers linked by associations is merged into a cluster. The centroid of the cluster is computed by the log-energy-weighted cell positions in the third electromagnetic layer.

$$\vec{x}_c = \frac{\Sigma_i w_i \vec{x}_i}{\Sigma_i w_i}, \qquad w_i = \max[0, w_0 + \ln \frac{E_i}{E_{tot}}], \tag{3.8}$$

where $E_i$ is the energy in the $i^{th}$ cell and $w_0$ is an $\eta$ and $E_T$ dependent parameter, chosen to optimize the position resolution.

The following requirements are used to select electron and photon candidates:

- The $E_T$ of the cluster has to be greater than 1.5 GeV. In addition, the energy in the EM portion of the calorimeter is required to exceed 90% of the total energy in the cluster, and the energy outside the central tower has to be less than 60%.

- If there is a central detector track pointing to the calorimeter cluster within a $|\Delta\eta| = 0.1$ and $|\Delta\phi| = 0.1$ "road", the cluster is identified as an electron candidate and stored in the PELC bank. Otherwise, it will be classified as a photon candidate and saved in the PPHO bank. The size of $|\Delta\eta|$ can vary with the resolution of the vertex position.

### 3.3.2 Offline Electron Selection

The above reconstruction requirements are very loose. There are many variables that are used to refine the selection of electron candidates for the final analysis. In order to compare the signal (electrons like those from $W$ decays) to the background for different cuts, we have to generate reference samples for both signals and backgrounds. The best signal sample comes from the $Z \rightarrow e^+e^-$ candidates: by selecting PELC pairs with an invariant mass around the $Z$ mass peak and with at least one of them being a "good" PELC, we have the other PELC as an unbiased electron. We use the set of these electrons to study electron identification. The background sample is more readily available, since more than 95% of PELC's are not from either $W$ or $Z$ decays to begin with, and we select those events which have only a single PELC and low $\not{E}_T$ to further discriminate against $W$'s and $Z$'s. We define a "loose" and a "tight" electron based on the following parameters:

(1) **Isolation Parameter**

Since an electron from a $W$ or $Z$ decay does not come from a jet, it should appear as isolated from other particles. The isolation parameter for a cluster is defined as

$$f_{iso} = \frac{E_{total}(\mathcal{R} = 0.4) - E_{EM}(\mathcal{R} = 0.2)}{E_{EM}(\mathcal{R} = 0.2)}, \tag{3.9}$$

where $E_{total}(\mathcal{R})$ ($E_{EM}(\mathcal{R})$) is the total (EM) calorimeter energy in the core of the radius $\mathcal{R} = \sqrt{\Delta\eta^2 + \Delta\phi^2}$. In Fig. 3.2 we show distributions of $f_{iso}$ for electron candidates from the $Z \rightarrow ee$ sample (shaded histogram)

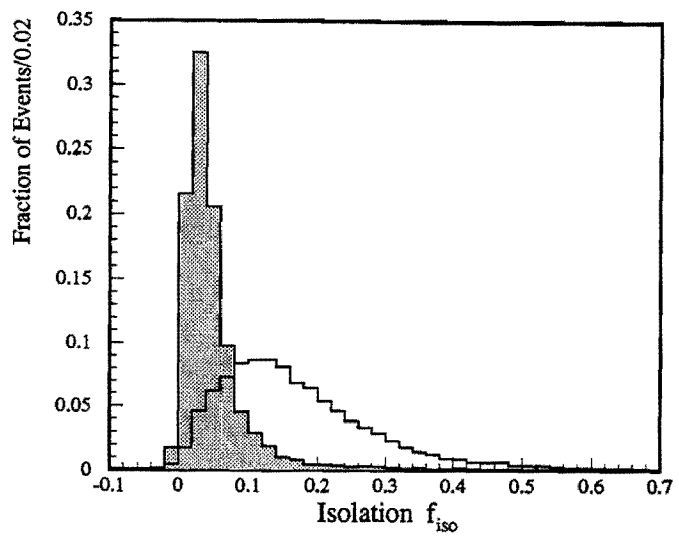


Figure 3.2: The isolation parameter ($f_{iso}$) distribution for electron signals (shaded) and backgrounds (unshaded).

and for all PELC objects (unshaded histogram) from the events with a single PELC and $\not\!\!E_T < 10\,\mathrm{GeV}$ (background). The requirement for "loose" electrons is $f_{iso} < 0.15$; for "tight" electrons it is $f_{iso} < 0.1$.

(2) **Electron Likelihood**

Most "fake" electrons are from two sources — low energy charged hadrons spatially overlapping with energetic photons from $\pi^0$ or $\eta$ decays, and isolated photons which have converted to $e^+e^-$. The "standard" procedure [39, 38] cuts on four variables that are included in the PELC banks (or associated banks):

- the H-matrix $\chi^2$,
- the track match ($\sigma_{trk}$),
- the track ionization ($dE/dx$) in the CD,

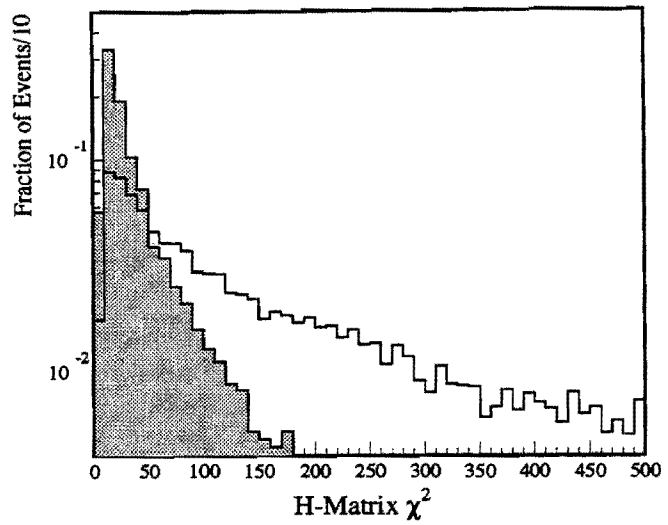


Figure 3.3: The distribution of $\chi^2$ for the electron signal sample (shaded) and background sample (unshaded).

- the EM energy fraction ($f_{EM}$).

However, we found that a multidimensional likelihood calculation, the Neyman-Pearson test [40, 41], gives better rejection of these backgrounds than cuts on the four variables individually. We first introduce these variables and then explain the likelihood method [42].

- **H-matrix $\chi^2$**: The H-matrix algorithm [39] is used to analyze the shower profile in the calorimeter. The shower shape is characterized by the distribution of fractional shower energies throughout the calorimeter. These fractions are correlated, since a shower which deposits a large fraction of its energy in the first layer will deposit a smaller fraction in subsequent layers and vice versa. In order to take these correlations into account, we construct a $41 \times 41$ covariance matrix (**V**) from a reference sample of $N$ Monte Carlo electrons

with energies ranging from 10 to 150 GeV. The covariance matrix is defined as

$$V_{ij} = \frac{1}{N}\sum_{n=1}^{N}(x_i^n - \overline{x_i})(x_j^n - \overline{x_j}), \tag{3.10}$$

where $x_i^n$ is the value of the $i^{th}$ observable for the $n^{th}$ electron and $\overline{x_i}$ is the mean of the $i^{th}$ observable. These 41 observables consist of the fractional energies in layers 1,2,and 4 of the EM calorimeter, the fractional energies in each cell of a $6 \times 6$ array in EM layer 3 centered on the most energetic tower in the cluster, the $z$-position of the interaction vertex, and the logarithm of the total cluster energy. A **V** matrix is built for each of 37 $|\eta|$ values. The **H**-matrix is then defined by the inverse of this covariance matrix

$$\mathbf{H} \equiv \mathbf{V}^{-1}. \tag{3.11}$$

For a shower characterized by the observables $x_i'$, the $\chi^2$ describes how likely these observables are to be due to single electrons rather than hadrons with or without accompanying electromagnetic radiation.

$$\chi^2 = \sum_{i,j=1}^{41}(x_i' - \overline{x_i})H_{ij}(x_j' - \overline{x_j}). \tag{3.12}$$

Fig. 3.3 shows the distribution of $\chi^2$ for electron candidates compared to that for fakes.

- **Track Match** $\sigma_{trk}$: As mentioned before, one of our major backgrounds is a charged hadronic particle overlapping with photons

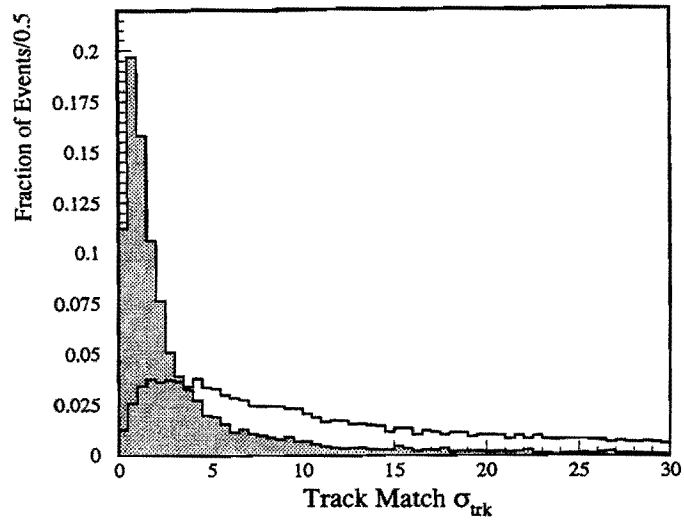


Figure 3.4: The track match parameter ($\sigma_{trk}$) distribution for electron signals (shaded) and backgrounds (unshaded).

from the decay of neutral mesons ($\pi^0$'s, $\eta^0$'s). In such cases no tracks are left in the central detector unless one is generated by an adjacent charged particle. This background is reduced by requiring the CD track to point precisely to the centroid of the calorimeter cluster. The track match significance is defined as:

$$\sigma_{trk} = \sqrt{\left(\frac{\Delta\phi}{\delta_{\Delta\phi}}\right)^2 + \left(\frac{\Delta z}{\delta_{\Delta z}}\right)^2}, \tag{3.13}$$

if the cluster is in the Central Calorimeter (CC). $\Delta\phi$ is the azimuthal mismatch, $\Delta z$ the mismatch in the $z$ direction (beam direction), and $\delta_x$ is the resolution in observable $x$. For candidates in the End Calorimeter (EC),

$$\sigma_{trk} = \sqrt{\left(\frac{\Delta\phi}{\delta_{\Delta\phi}}\right)^2 + \left(\frac{\Delta r}{\delta_{\Delta r}}\right)^2}, \tag{3.14}$$

where $\Delta r$ is the mismatch transverse to the beam. The distribution of the track match significance for both signal and background is shown in Fig. 3.4.

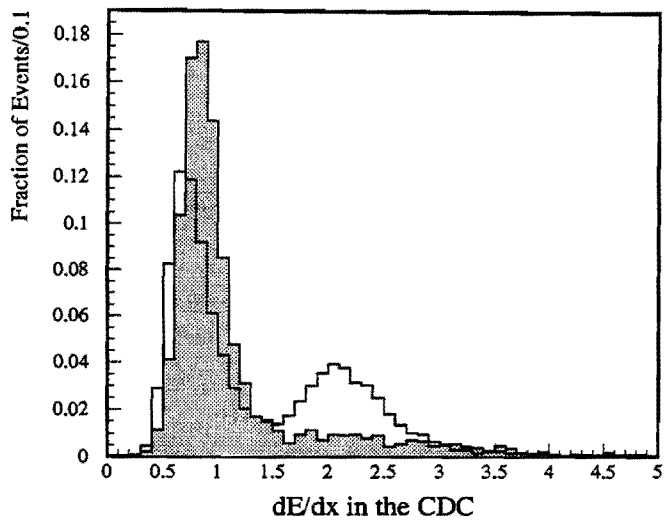


Figure 3.5: The $dE/dx$ distribution for electron signals (shaded) and backgrounds (unshaded) in the CDC.

- **Track Ionization $dE/dx$**: Since there is no central magnetic field in the DØ detector, $e^+e^-$ pairs from photon conversions will not separate from each other and will be reconstructed as a single track. However, their energy deposition per unit length ($dE/dx$) will be twice that of a single charged particle. Fig. 3.5 shows that most electrons have $dE/dx \sim 1$ while the background events have a bump around 2.

- **EM fraction $f_{EM}$**: Electron candidates in the PELC bank have already passed the requirement that the electromagnetic energy fraction be higher than 90% ($f_{EM} > 0.9$). Fig. 3.6 shows that most

electrons have even higher EM fractions as compared to the backgrounds. This variable is included to help reject background in the likelihood test.

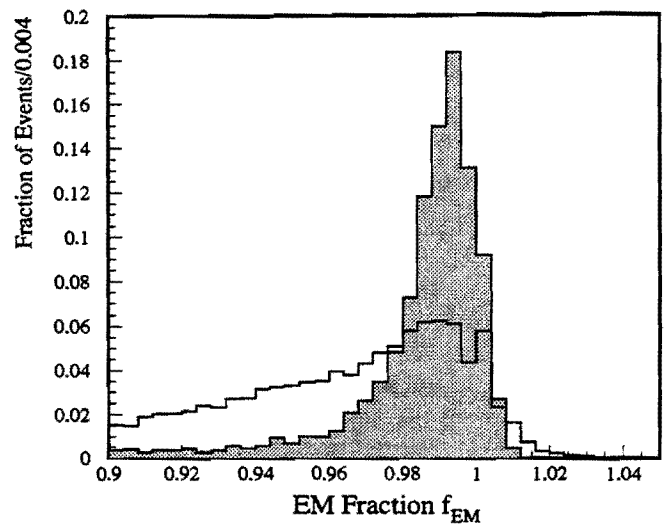


Figure 3.6: The EM fraction distribution for electron signals (shaded) and backgrounds (unshaded).

Let $x$ denote a 4 dimensional column array consisting of the 4 parameters described above. $p(x|e)dx$ (or $p(x|b)dx$) represents the probability that these four parameters of a signal (or background) event falls in the interval $[x, x+dx]$. These four parameters are assumed to be statistically independent, and although there is apparently some correlation between the H-matrix $\chi^2$ and $f_{EM}$, this is still a good approximation. Based on the assumption, the probability density functions $p(x|h)$ for signals (h=e) and backgrounds (h=b), then are computed by using the formula

$$p(x|h) = p_1(\chi^2|h) \cdot p_2(\sigma_{trk}|h) \cdot p_3(dE/dx|h) \cdot p_4(f_{EM}|h)\,. \qquad (3.15)$$

where $p_i(x_i|h)$ is the probability distribution function of variable $x_i$ for real electrons (h=e) or fakes (h=b). To implement density functions, each distribution is normalized and split into bins. (50-100 bins are used for each distribution.) Each bin in each distribution has a probability given by the integral of the probability density over the bin. $p(x|h)$ then is a product of four individual probabilities, each one according to which bin $x_i$ falls into.

A PELC characterized by a 4 dimensional array $x'$ is considered to be an electron if it passes the likelihood test:

$$\mathcal{L}_e \equiv \frac{p(x'|b)}{p(x'|e)} < k\,. \tag{3.16}$$

The "tight" electron cuts require $\mathcal{L}_e < 0.25$ if the cluster is in the CC, and $\mathcal{L}_e < 0.30$ if it is in the EC. The "loose" cuts require $\mathcal{L}_e < 0.5$ in both the CC and EC.

In addition to these quality cuts, the analysis also applies kinematic cuts on electron $E_T$ and $\eta$ that will be discussed in the next chapter. Also because no EM layers exist in the gap between the CC and EC, the region $1.2 \leq |\eta^{det}| \leq 1.4$ is excluded, where $|\eta^{det}|$ is calculated from the center of the detector rather than the vertex of the event.

The efficiencies of offline cuts have been studied using unbiased electrons from $Z \rightarrow ee$ sample by tagging one electron with tight cuts. We further subdivide the sample into CC ($|\eta^{det}| < 1.2$) and EC ($1.4 < |\eta^{det}| < 2.5$) depending on the fiducial regions of unbiased electrons. The invariant mass distribution

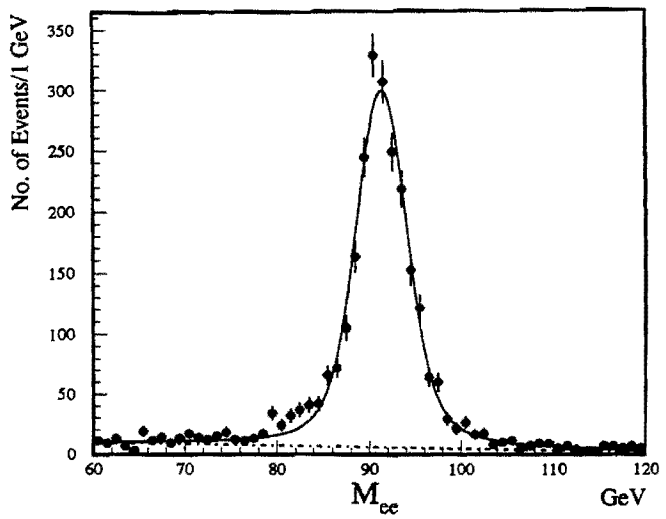


Figure 3.7: The invariant mass spectrum for electron pairs (solid dots) with unbiased electron in the CC. It is fitted to a Breit-Wigner curve convoluted with a Gaussian (solid line) plus a straight line background (dashed line).

($M_{ee}$) is shown in Fig. 3.7. While computing efficiencies the following two samples are used.

- The parent sample: the unbiased electrons with the invariant mass of electron pairs in the range $86 < M_{ee} < 96$ GeV. This sample represents good electrons. We have 1957 events in the CC and 908 events in the EC.

- The control sample: the unbiased electrons with the $ee$ invariant mass between 60 and 70 GeV, far from the $Z$ peak. This sample is used to compute the background. There are 109 (55) events in the CC (EC).

We fit the invariant mass spectrum to a Breit-Wigner curve convoluted with a Gaussian plus a straight line background. This straight line background fit is used to estimate the contamination in the parent sample. We find the

background fraction is $f_b = (3.0 \pm 0.5)\%$ in the CC and $f_b = (4.3 \pm 1.0)\%$ in the EC. The electron efficiency for a given cut is calculated by

$$\varepsilon_s = \frac{\varepsilon_p - \varepsilon_b f_b}{1 - f_b}, \tag{3.17}$$

where $\varepsilon_p$ and $\varepsilon_b$ are the fraction of electrons passing the given cut in the parent sample and the control sample respectively. The systematic error is mainly due to the uncertainty in the background estimation. Therefore we take $|\varepsilon_s - \varepsilon_p|$ as our systematic error. In Table 3.1 we list the efficiency for tight and loose cuts.

| cut | efficiency in the CC (%) | cut | efficiency in the EC (%) |
|---|---|---|---|
| $f_{iso} < 0.15$ | $98.9 \pm 0.6$ | $f_{iso} < 0.15$ | $99.4 \pm 0.4$ |
| $f_{iso} < 0.1$ | $95.9 \pm 1.1$ | $f_{iso} < 0.1$ | $96.9 \pm 1.0$ |
| $\mathcal{L}_e < 0.5$ | $85.9 \pm 1.5$ | $\mathcal{L}_e < 0.5$ | $62.5 \pm 1.9$ |
| $\mathcal{L}_e < 0.25$ | $80.5 \pm 1.5$ | $\mathcal{L}_e < 0.3$ | $50.6 \pm 1.9$ |
| loose cut ($f_{iso} < 0.15$, $\mathcal{L}_e < 0.5$) | $85.5 \pm 1.6$ | loose cut ($f_{iso} < 0.15$, $\mathcal{L}_e < 0.5$) | $62.4 \pm 1.9$ |
| tight cut ($f_{iso} < 0.1$, $\mathcal{L}_e < 0.25$) | $78.7 \pm 1.6$ | tight cut ($f_{iso} < 0.1$, $\mathcal{L}_e < 0.3$) | $49.8 \pm 1.9$ |

Table 3.1: The efficiencies of electron offline cuts.

## 3.4 Jets

### 3.4.1 Jet Reconstruction

Hard collisions of particles produce quarks and gluons. These colored partons can be regarded as free during the collision, but subsequently each will "hadronize" or "fragment" into a group of colorless hadronic particles through the creation of additional quark-antiquark pairs. This group of particles tends to lie in a cone around the direction of motion of the original parton, and deposits a "shower" of energy in a small $\eta$–$\phi$ space of the calorimeter. This energy cluster forms a jet. Hard and soft parton radiation makes it difficult to define exactly the relationship of the "jet" to the "original" parton. For this reason, DØ uses more than one definition for a jet.

The most common definition uses the "fixed cone algorithm", in which jets are taken to be the energy inside of cones of a fixed radius in $\eta$–$\phi$ space. Cones with three different radii are constructed by DØRECO, i.e., 0.7, 0.5 and 0.3. Users can choose which one to use depending on the particular physics analysis. Generally speaking, a small cone algorithm is suitable for events with many jets because two close jets may be merged together when reconstructed with a big cone algorithm. A small cone, on the other hand, may not contain all the energy of a jet. To compromise these factors, the 0.5 cone jet algorithm is used in the DØ top search and is described below.

- The jet reconstruction process starts with the determination of the $E_T$

contained in $\Delta\eta \times \Delta\phi = 0.1 \times 0.1$ calorimeter towers. As in Section 3.2,

$$E_x = \sum_i^{tower} E_x^i \tag{3.18}$$

$$E_y = \sum_i^{tower} E_y^i, \tag{3.19}$$

and the $E_T$ is calculated as

$$E_T = \sqrt{E_x^2 + E_y^2}. \tag{3.20}$$

The towers with $E_T$ higher than 1.0 GeV threshold are selected as "seed towers" and sorted in decreasing order of $E_T$. "Pre-clusters" are formed from all contiguous seed towers within $|\Delta\eta| < 0.3$ and $|\Delta\phi| < 0.3$. For each pre-cluster, the $E_T$-weighted centroid defines the axis of the corresponding jet candidate.

- A cluster is defined around each pre-cluster that includes all towers within a fixed cone radius ($\mathcal{R} = 0.5$ in our case). The centroid of this new cluster is re-computed, which defines a new jet axis. The process is repeated until the shift of the jet axis is less than 0.001 in $\eta$–$\phi$ space or the iteration reaches the maximum value of 50 times.

- If two clusters share some energy with each other, then the shared $E_T$ is examined. If it is more than 50% of that of the lower $E_T$ cluster, the two clusters are merged, and the jet axis recalculated. Otherwise, the jets are split, and each shared cell is assigned to the closest cluster.

- Finally, clusters with $E_T > 8$ GeV are stored in the JETS bank as jet candidates.

The jet energy resolution has been examined by using the transverse momentum balance between the two jets in dijet events. The jet $E_T$ resolution is parameterized as:

$$\left(\frac{\sigma_{E_T}}{E_T}\right)^2 = C^2 + \frac{S^2}{E_T} + \frac{N^2}{E_T^2}, \tag{3.21}$$

where $C$ is a cell by cell error from the calibration, $S$ represents the shower fluctuations in the sampling gap, and $N$ denotes the contribution of noise. The resolution in the forward region is worse than in the Central Calorimeter due to the out-of-cone energy and $\eta$ resolution effects. In the CC we have $C = 0.0 \pm 0.005$, $S = 0.81 \pm 0.016\sqrt{\text{GeV}}$, $N = 7.07 \pm 0.09\,\text{GeV}$ [37].

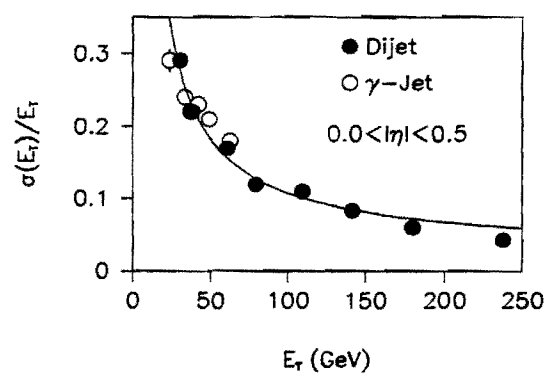


Figure 3.8: The jet energy resolution as a function of the average corrected jet $E_T$.

### 3.4.2 Energy Corrections

There are many effects which introduce systematic errors in the energies recorded by the calorimeter, such as nonuniformities in the calorimeter, nonlinearities in the calorimeter response to hadrons, noise due to the radioactivity

of uranium, and extra energy due to the underlying event. So a series of energy corrections are applied to both electrons and jets.

The electromagnetic (EM) section sets the absolute energy scale for the DØ calorimeter. The EM energy has been calibrated by constraining the $Z \rightarrow e^+e^-$ invariant mass to the measured LEP value. This introduced a correction factor of about 5% in the Central Calorimeter. Low mass resonances ($\pi^0 \rightarrow \gamma\gamma$, $J/\psi \rightarrow e^+e^-$) also have been checked at different energies.

The hadronic energy has been corrected using a procedure developed by the CDF collaboration [43], called the "Missing $E_T$ Projection Fraction" ($MPF$) method. Events which consist of an isolated photon and a single hadronic jet lying opposite in $\phi$, having no leptons of noticeable energy should not include neutrinos of noticeable energy and should register no $\not{E}_T$. It is assumed, therefore, that the observed $\not{E}_T$ in such a direct photon event is entirely due to jet energy mismeasurement. The error in the jet energy is assumed to be the projection of the $\not{E}_T$ along the jet axis.

$$E_T^{true} - E_T^{jet} = \vec{\not{E}}_T \cdot \hat{n}_T^{jet} . \tag{3.22}$$

The missing $E_T$ projection fraction (MPF) is defined as the correction factor

$$MPF \equiv \frac{\vec{\not{E}}_T \cdot \hat{n}_T^{jet}}{E_T^{jet}} . \tag{3.23}$$

This correction is a function of jet $E_T$, $\eta$, and electromagnetic content.

The energy contributions due to hadrons from spectator partons (underlying events) were determined from the minimum-bias event sample. The $E_T$ contribution from these particles is a constant in $\eta$ and $\phi$ with a value of

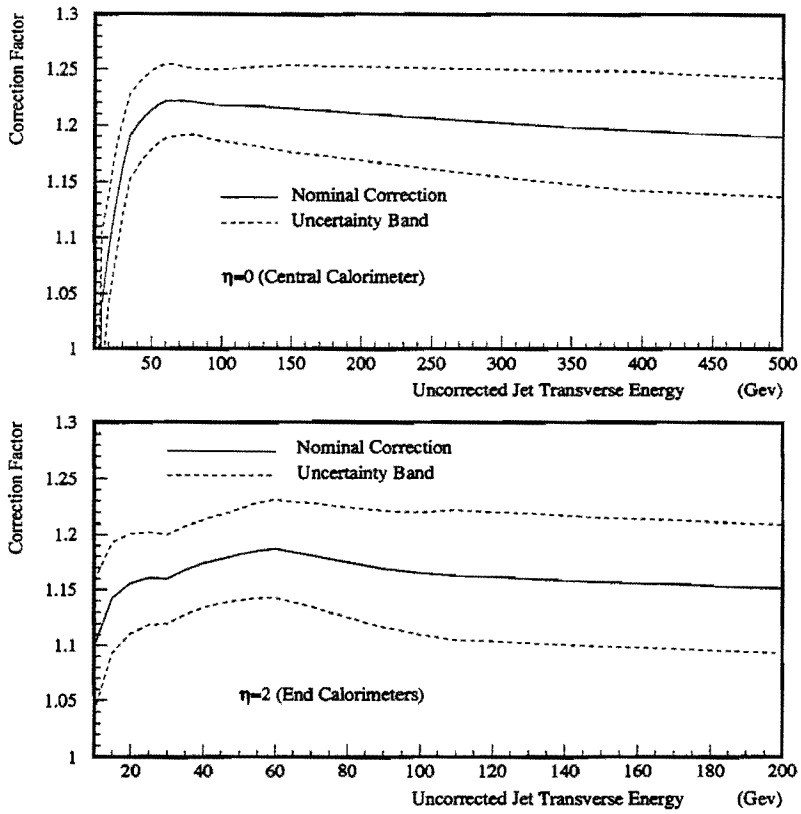


Figure 3.9: Energy correction factor for jets as a function of $E_T$ at $\eta = 0$ (upper) and $\eta = 2$ (lower).

$d^2E_T/d\eta d\phi = 0.55 \pm 0.1$ GeV. Corrections to the Calorimeter's non-linearities and out-of-cone showering were obtained from the Monte Carlo. It was found that an average of 96% of the jet's energy was reconstructed by the 0.5 cone jet algorithm independent of the jet energy.

## 3.5 Muons

### 3.5.1 Muon Reconstruction

Muons are reconstructed as tracks in the muon drift chambers. The reconstruction process is divided into three stages. In the first stage, the raw data (hits) are converted into locations in the coordinate systems of the specific muon chambers, and then transformed to the DØ global coordinate system. These hits are then combined into (muon) tracks. Since there is magnetized iron (the toroid) between the first and second layers of drift tubes, the tracks are bent in the field. DØRECO first fits straight lines through the hits in the outer chambers and then projects them to the magnet center. From these points it projects lines to the vertex point to find the hits in the inner chambers associated with the outer tracks. (This procedure eliminates most hits due to leakage from the calorimeter.) The final stage of muon reconstruction is a global fit: the muon tracks are linked with energy deposits of minimum ionizing particles (MIP's) in the calorimeter and with tracks in the central tracker. Approximately 70% of the locally determined muon track candidates are successfully fitted globally.

The transverse momentum of the muons in the muon chambers is determined from the deflection of the tracks and the $\int B\,dl$ in the toroid. A muon will typically lose a few GeV in the calorimeter; this energy loss is corrected for, using Monte Carlo calculations, and added to the measured muon momentum.

The muon momentum resolution is primarily determined by two compo-

nents: the multiple Coulomb scattering that occurs in the iron toroid, and the position resolution of the hits in muon chambers. Chamber inefficiencies and geometrical misalignment also degrade the momentum resolution. The resolution of the muon momentum is parameterized as [45]:

$$\left(\frac{\sigma_p}{p}\right)^2 = \left(\frac{0.18 \cdot (p-2)}{p}\right)^2 + ((0.003 \pm 0.001) \cdot p)^2 \ , \tag{3.24}$$

with $p$ in GeV. The first term is due to multiple Coulomb scattering and the second term comes from the space point drift resolution ($\sim 1\,\mathrm{mm}$). This parameterization was determined by comparing $Z \rightarrow \mu^+\mu^-$ data with the Monte Carlo simulated events where the position resolution was degraded until the width of the $\mu^+\mu^-$ invariant mass matched the data. The parameterization indicates that below 60 GeV the muon resolution is mainly determined by multiple scattering.

### 3.5.2 Offline Muon Selection

Due to efficiency problems in the end chambers resulting from chamber aging, we require all muons to be contained in the central muon (CF) system ($|\eta^{det}| < 1.0$). For $t\bar{t}$ events, which have all decay products roughly in the central region, this does not cause too much efficiency loss. Just as for electrons, there are some requirements used to define a good muon.

- **Muon Track Quality (IFW4)**: Each muon candidate has several quality flags associated with it during the reconstruction. One of those flags is IFW4 which reflects the track quality of the muon. It is defined as the number of failures in the following checklist:

- No missing modules.
- Nonbend view impact parameter $\leq 100\,\mathrm{cm}$
- Bend view impact parameter $\leq 80\,\mathrm{cm}$
- Nonbend view hit fit residual rms $\leq 7\,\mathrm{cm}$
- Bend view hit fit residual rms $\leq 1\,\mathrm{cm}$

After scanning the muon candidates event by event, we found that IFW4 was a very powerful tool for suppressing cosmic rays and combinatorics. Good muon candidates have an IFW4 value of zero. The candidates with IFW4$\geq 2$ were found to be mostly cosmic ray or combinatorics. So, we require that muon candidates have IFW4$\leq 1$.

- **A-stub rejection**: Some muon candidates only have hits in the innermost layer (A layer). In order to insure a good momentum determination of the muon track candidate and reduce the possibility of picking up candidates from hadronic punchthrough, we exclude these muon candidates from further consideration.

- **Calorimeter Confirmation**: Muons typically deposit 1 to 3 GeV of energy in the calorimeter and leave a distinctive energy signature over the total path length. The Muon Tracking in the Calorimeter (MTC) package [44] (which was included in DØRECO after version 12.11) uses the event vertex position and the muon candidate information to identify and reconstruct a track-like energy deposition in the calorimeter. The program locates a cluster of $5 \times 5$ towers in the calorimeter centered

on that candidate's trajectory in each layer. Hits are defined as any calorimeter cell in the cluster with a positive energy above zero suppression. The best calorimeter muon track is found by fitting a line through the calorimeter cells from the hadronic section toward the vertex. The quality of fit depends on the fraction of calorimeter layers used to get a fit. Parameters used in muon identification in the calorimeter are:

- **HFRAC.** It is defined as fraction of hadronic calorimeter layers used for the track fit out of the maximum possible. Ideally good muons will have HFRAC = 1 — in that case all possible layers are used for the track fit.
- **EFRAC_H1**: The energy fraction of last hadronic layer out of total for a cluster of $3 \times 3$ towers; usually only muons deposit energy in the last layer.

The requirement is:

$$\mathrm{HFRAC} = 1 \text{ or} \tag{3.25}$$

$$\mathrm{HFRAC} \geq 0.7\,, \quad \mathrm{EFRAC_H1} > 0\,. \tag{3.26}$$

In addition to the above cuts, we also require muons with a minimum $p_T^\mu$ of 4 GeV; this will be discussed in the next chapter.

During the February 1995 shutdown, some muon chambers were cleaned, so we expected to have different characteristics. In addition, the instantaneous luminosity was much higher after this shutdown, so we could get more random hits from the beam spray in the forward and backward chambers and

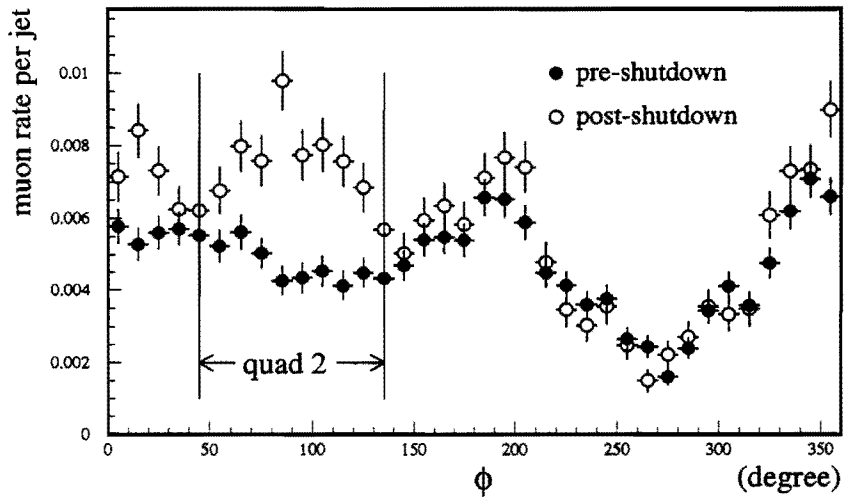


Figure 3.10: The $\phi$ distribution of muon rate per jet for the pre-shutdown (solid circles) and post-shutdown (open circles) data.

cause more fake combinatoric tracks. To compare the differences between "pre-shutdown" and "post-shutdown" muons, we preselect data from the trigger JET_MULTI. This trigger requires 5 jets above 10 GeV and has no muon requirement (which can prevent a possible bias from the trigger). Since the major muon sources come from heavy quark decay, we can use the muon rate per jet as an index. Muons have to pass the above offline cuts, with a minimum $p_T^\mu$ of 4 GeV, and be in the neighborhood of a jet ($\Delta R_{\mu j} \equiv \sqrt{\Delta\eta_{\mu j}^2 + \Delta\phi_{\mu j}^2} < 0.5$). The $\phi$ distribution of this rate is shown in Fig. 3.10. In the second quadrant ($45° < \phi < 135°$) the post-shutdown rate is nearly twice as high as that of pre-shutdown. The $\eta$ distribution for muons in this quadrant is shown in Fig. 3.11. The extra post-shutdown muons were located in the $|\eta| > 0.5$ region. We find that about 47% of them missed B layer. This percentage is almost three times as large as that of pre-shutdown muons (17%). After scanning those events,

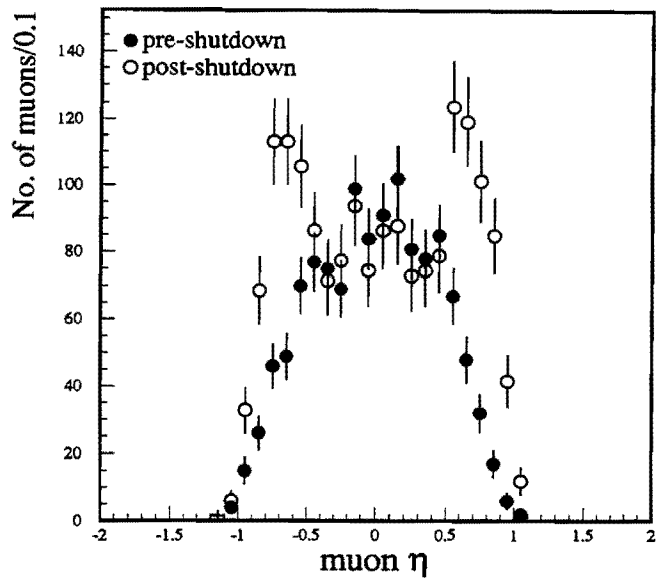


Figure 3.11: The $\eta$ distribution for the pre-shutdown (solid circles) and post-shutdown muons (open circles) in the second quadrant. The post-shutdown data has been normalized to that of pre-shutdown according to their luminosities.

we find that most "B-layer-missed" muons appear to be combinatoric tracks of A-stub hits and the hits in C layer possibly from the beam spray. For this reason, we further ask the post-shutdown muons to have B layer hits if they are in the second quadrant with $|\eta| > 0.5$, unless the muon projects into the B layer gaps and has all hits in A and C layers (4 hits in A layer and 3 hits in C layer).

To study the efficiencies of the offline IFW4 and calorimeter confirmation cuts, we select events from a number of jet triggers (listed in Table 3.2). Because our signal triggers do not require muons (see Section 4.1), this selection avoids trigger biases. For muons from semileptonic decays of $b$ or $c$ quarks which are part of the hadronic jets, the muons have to be associated with jets, and all isolated muons can be assumed as background (dominated by combina-

| triggers | number of events |
|---|---|
| JET_MIN | 301,612 |
| JET_30 | 880,000 |
| JET_50 | 704,941 |
| JET_85 | 947,381 |
| JET_MAX | 237,475 |

Table 3.2: Triggers used to study the efficiencies of muon cuts.

torics or cosmic rays). Here we can entirely ignore the isolated muons from $W$ or $Z$ decays because the cross sections of heavy quarks are orders of magnitude larger than those of $W$ and $Z$. Therefore, the distance between a muon and its nearest jet in $\eta$–$\phi$ space ($\Delta R_{\mu j}$) is used as a characteristic parameter. The $\Delta R_{\mu j}$ distributions with different selection criteria are plotted in Fig. 3.12. The muons with IFW4 $\geq 2$ are mostly background, so the $\Delta R_{\mu j}$ distribution is just the separation between random vectors with jets. Just as expected, the muon passing our final cuts are mostly confined within a $\Delta R_{\mu j} < 0.5$ cone.

To study the efficiency of IFW4 cut, we pre-select CF muons with $p_T^{\mu} >$ 4 GeV, no A-stubs, and passing the calorimeter confirmation requirement. A parent sample and a control sample are defined as follows:

- The parent sample: muons with $\Delta R_{\mu j} < 0.3$. This sample represents good muon candidates.

- The control sample: muons with $\Delta R_{\mu j} > 1.0$. This sample is used to estimate the backgrounds.

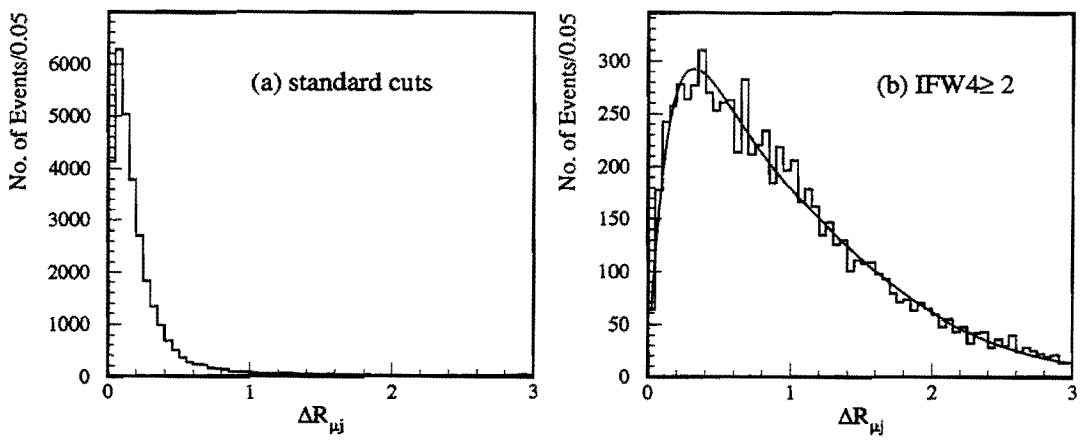


Figure 3.12: The $\Delta R_{\mu j}$ distribution of muons with (a) the standard cuts and (b) IFW4 $\geq$2.

Background in the region of the parent sample is estimated to be about 40% of the control sample from the bad muon distribution (Fig. 3.12(b)). Further studies are made similarly to the previous (electron) case. The efficiency for a cut was calculated by Equation (3.17). The efficiency for the IFW4 cut is $(96.5 \pm 0.3)\%$.

The calorimeter confirmation efficiency has been examined in a similar way. The pre-selection cuts are the same kinematic cuts as before along with IFW4 $= 0$ and in-time muon track ($t_0^f \leq 50\,\mathrm{ns}$). The overall efficiency is assumed to be the product of the individual efficiencies because there is no obvious correlation between them. The results are shown in Table 3.3.

## 3.6 Monte Carlo Simulation

We use Monte Carlo simulation mainly to generate signal and background data in order to optimize our selection cuts and estimate their efficiencies. The

| cut | efficiency (%) |
|---|---|
| IFW4$\leq$ 1 | $96.5 \pm 0.3$ |
| Calorimeter Confirm. | $98.7 \pm 1.3$ |
| Combination of the above two | $95.2 \pm 1.4$ |

Table 3.3: The efficiencies of CF muon offline cuts.

first step in the simulation is the event generation; physics events are generated according to theoretical calculations and phenomenological models. The second step is the simulation of the detector response to the generated events and the presentation of the analog and digital signals thus created in a format similar to the output of the data acquisition system. Finally the simulated events are reconstructed and analyzed as if they were experimental data. There is an uncertainty about how well the calculational model corresponds to what is happening in the experiment, so a major effort is made to find data checks of the Monte Carlo and direct determinations of backgrounds from the data, whenever possible.

### 3.6.1 Generators

ISAJET [46], the default generator in the DØ experiment, is used to simulate $pp$ and $p\bar{p}$ collisions and to model the hard parton-parton scattering processes. The algorithm of simulation incorporates perturbative QCD cross sections, leading order QCD radiative corrections for initial and final state partons, and phenomenological models for jet and beam jet fragmentation. The generation processes follow four distinct steps:

- **Hard Scattering**: The initial step is the calculation of the $p\overline{p}$ cross section for partons $i$ and $j$ to (inclusively) produce parton $k$, from the QCD perturbative leading order two body scattering interaction.

$$\sigma_{ij\to k} = \int dx_i \int dx_j \, f_i(x_i, Q^2) \, f_j(x_j, Q^2) \, \hat{\sigma}_{ij\to k} \, , \tag{3.27}$$

  where $x_i = p_i/p$ is the momentum fraction of parton $i$, $Q^2$ is the momentum transfer, $f(x, Q^2)$ is the parton density distribution function, and $\hat{\sigma}_{ij\to k}$ is a cross section calculated in QCD perturbation theory. The $t\bar{t}$ Monte Carlo is generated by ISAJET using the default EHLQ (Eichten, Hinchliffe, Lane and Quigg) structure functions [51].

- **QCD Radiative Corrections**: After the primary hard scattering is generated, QCD radiative corrections are added to model jet multiplicity in order to obtain the correct event structure. The radiations of photons, $W$'s, and $Z$'s from the final state quarks are also included and treated in the same approximation as QCD radiation.

- **Jet Fragmentation**: Colored quarks and gluons fragment into colorless hadrons when ejected into free space. Fragmentation is governed by soft non-perturbative processes that cannot be calculated from scratch. ISAJET uses the Feynman-Field fragmentation model [47] to simulate the process. In this fragmentation model a quark generates quark-antiquark pairs by the color force with the ratios $u : d : s = 0.43 : 0.43 : 0.14$. These numbers show the smaller probability for the production of the heavier $s$ quark. We also use HERWIG [52] generator in the

Monte Carlo study. HERWIG adopts a cluster hadronization model to handle the process.

- **Beam Jets**: In addition to the hard scattering, the spectator partons from beam jets add many low $p_T$ hadrons to the event. ISAJET uses a scheme based on the Abramovskii, Kanchelli and Gribov (AKG) model to calculate this effect. This forms the "underlying event."

In addition to ISAJET, the VECBOS Monte Carlo [48] is used to study the kinematics of the $W$ + jets background. VECBOS is a parton-level program using exact tree-level matrix elements for $W$ (or $Z$) + $n\,jets$ processes, where $1 \leq n \leq 4$. To generate events, one has to specify the value of $n$, so each order has to be generated separately. The VECBOS program processes the interaction of the incoming partons to produce a $W$ boson plus a definite number of additional partons in the final state. We then process this event through a modified version of ISAJET to handle final state radiation, jet fragmentation and include the effects of the underlying event. As VECBOS provides no information about the flavor of the final partons it is assumed that they are all gluons. For the analysis used in the $W$ + jets background study we require $E_T > 10\,\text{GeV}$ for all the final state partons, and use CTEQ1M for the structure functions [49].

### 3.6.2 Detector Simulation

The DØ detector simulation program is DØGEANT [50], a customized version of the CERN GEANT3 program. It is used to give the response of the

detector to the particles generated by the Monte Carlo by taking into account the various physics processes involved, including $\delta$-ray production, multiple Coulomb scattering, full electromagnetic and hadronic showering, electron and muon bremsstrahlung, and particle decays.

The output of DØGEANT needs further refinement in order to provide a better representation of the data. Therefore, the NOISY package for the calorimeter and the MUSMEAR package for the muon system are used in the simulation as described in the following:

- The NOISY Package: NOISY adds uranium noise and electronic fluctuations to the calorimeter raw data bank CAD cell by cell. It is based on the experimental pedestal distributions which were taken during the beam-off time after every store. To model multiple interactions and event pile-up, NOISY superposes events from an additional input stream of Monte Carlo minimum-bias data.

- The MUSMEAR Package: DØGEANT uses the design chamber resolution when it propagates muon tracks through the muon chambers. However, the actual resolution is not as good. There are many factors that DØGEANT does not consider, such as detector misalignment, inefficiency of the chambers and worse drift time resolution. To account for all these factors, the MUSMEAR package does the following 3 things.

  - The time resolution and the time division resolution are smeared according to the experimental data.

- The package drops hits from the muon raw data bank MUD1 to simulate the real efficiency of chambers.
- The package modifies the muon geometry in order to simulate the effect of misalignment.

# Chapter 4

# Data Analysis

The events of interest for this thesis are $t\bar{t}$ pairs that decay to $W^+ b\, W^- \bar{b}$, with one $W$ decaying to $e\nu$ and the other to quarks, and at least one jet containing a $\mu$ (which comes either from the $b$ or $c$ quark decay, hereafter called "$\mu$-tag"). We used level 1 and level 2 triggered events to select top decay candidates. The triggers primarily favor events in which a $W$ decays to an electron and in which there are also high $E_T$ jets. Further selection cuts are made in the offline analysis to reduce the number of background events. The trigger requirements, offline cuts and their effects on the efficiency of finding $t\bar{t}$ events are described in this chapter. The study of the background and how we estimate the number of background events that survive the cuts are also discussed.

Our signal events are a subset of the inclusive $W \rightarrow e\nu$ events, i.e., we look for an isolated good quality high $E_T$ electron along with a reasonably high $\not{E}_T$, the standard signature for a leptonically decaying $W$. The $\mu$-tag and the requirement of additional high $p_T$ jets distinguish this subset. The details

of the selection criteria are described in this chapter.

The data used in this analysis were collected between December 1993 and July 1995 (collider Run 1B). About 43 million events were recorded during this period and the total effective integrated luminosity for this analysis is $74.9\,\mathrm{pb}^{-1}$.

## 4.1 Online Event Selection

An event entered our data sample if it passed either one of the following level 2 (L2) filters (associated with its corresponding level 1 (L1) triggers): ELE_JET_HIGH or EM1_EISTRKCC_MS. In the course of the run some trigger criteria were modified; the description of the triggers and their modifications are spelled out in the following section.

### 4.1.1 Trigger Requirements

Features of the calorimeter relevant to the triggers for the data sample are:

- The readout towers in the DØ calorimeter are 0.1 in pseudorapidity ($\Delta\eta = 0.1$), and 0.1 in azimuth ($\Delta\phi = 0.1$).
- There are 4 EM layers, the third one of which spans the shower max region of EM objects and has a segmentation of $\Delta\eta \times \Delta\phi = 0.05 \times 0.05$.

L1 uses $\Delta\eta \times \Delta\phi = 0.2 \times 0.2$ clusters (of 4 towers) to trigger on "electrons" and "jets." L2 uses software algorithms and is therefore more flexible.

The general requirements for "electrons" and "jets" at both trigger levels are described here (and specified thresholds will be stated in the next section).

(i) **Electron Trigger Requirements**

- L1 trigger
  - The transverse EM energy in calorimeter clusters of $\Delta\eta \times \Delta\phi = 0.2 \times 0.2$ is required to be above a certain threshold.
- L2 trigger
  - The transverse EM energy in the $0.3 \times 0.3$ clusters centered about the highest EM energy tower in each L1 cluster has to be above a certain threshold.
  - The longitudinal shower profile requirement: The ratio of the energy deposited in the first fine hadronic layer to the energy in the electromagnetic layers ($\mathrm{FH1/EM_{TOT}}$) has to be below a given threshold which depends on the energy and $\eta$ position of the cluster in the detector.
  - The transverse shower profile requirement: The transverse shower profile has to satisfy a constraint on $\sigma_5 - \sigma_3$. $\sigma$ is an energy weighted shower radius in $\eta$–$\phi$ space as measured in the 3rd (highly segmented, shower max) electromagnetic layer

    $$\sigma = \Sigma \mathcal{R}_i E_i / \Sigma E_i \,,$$

    where $E_i$ is the cell energy, and $\mathcal{R}_i = \sqrt{\Delta\eta_i^{\,2} + \Delta\phi_i^{\,2}}$ as measured from the shower peak. $\sigma_3$ is the $\sigma$ calculated for the $3 \times 3$

cells configuration around the shower peak and $\sigma_5$ is the analogous $\sigma$ for the $5 \times 5$ cells configuration. These longitudinal and transverse shower shape cuts are $\eta$ and energy dependent and have been tuned using single electron data recorded during the DØ test beam run [53].

- The isolation criterion: The isolation variable is defined as the ratio

$$f_{iso} = \frac{E_{total}(\mathcal{R}_{iso}) - E_{EM}(\mathcal{R}_{core})}{E_{EM}(\mathcal{R}_{core})} < 0.15\,,$$

where $E_{total}$ is the total energy in a cone of radius $\mathcal{R}_{iso} = 0.4$ or 0.6, $E_{EM}(\mathcal{R}_{core})$ is the EM energy in a cone of radius $\mathcal{R}_{core} = 0.2$ in $\eta$–$\phi$ space. This cut is very similar to our offline isolation cut.

(ii) **Jet Trigger Requirements**

- L1 trigger
  - The transverse EM and fine hadronic energy ($\mathrm{FH} + \mathrm{EM_{TOT}}$) in $0.2 \times 0.2$ clusters is required to be above a certain threshold.
- L2 trigger
  - The L2 filter uses the L1 jet candidates as seeds and sorts them in descending $E_T$ order. Then the fixed cone size algorithm is applied to combine towers within a cone around each seed. In this process, some lower $E_T$ seeds could be swallowed up by their higher $E_T$ neighbors. The $\eta$ and $\phi$ of a jet are calculated

using $E_T$ weighted towers within the cone radius. The L2 trigger requires a certain number of jets to have $E_T$ above a given threshold within a certain range of $\eta$.

### 4.1.2 $W$ + jets triggers

We outline here the specific definitions of the two $W$ + jets triggers used to select data for this analysis.

(1) ELE_JET_HIGH

- L1: This trigger required an EM cluster with $E_T > 12\,\text{GeV}$ in the range of $|\eta| < 2.6$, and an additional jet with $E_T > 5\,\text{GeV}$.
- L2: This trigger required an EM cluster with $E_T > 15\,\text{GeV}$ in the range of $|\eta| < 2.5$ passing shower shape cuts, a jet with $E_T > 10\,\text{GeV}$ in $\mathcal{R} = 0.3$ cone and in the range of $|\eta| < 2.5$, and $\not{E}_T > 14\,\text{GeV}$.

(2) EM1_EISTRKCC_MS

- L1: This trigger required an EM cluster with $E_T > 12\,\text{GeV}$ during the early runs. After run 85277 it became necessary to reduce the rate from L1 to L2 because of high instantaneous luminosity occurrences. This was done by lowering the $E_T$ threshold to 10 GeV, and adding a level 1.5 (L1.5) requirement that the sum of the $E_T$ from the L1 "seed" cluster and the highest $E_T$ neighboring EM tower have $E_T > 15\,\text{GeV}$.

| Trigger Name | Level 1 | Level 1.5 | Level 2 |
|---|---|---|---|
| ELE_JET_HIGH | $\geq 1$ EM<br>$E_T^e > 12\,\text{GeV}$<br>$\lvert\eta^e\rvert < 2.6$<br>$\geq 1$ JET<br>$E_T^j > 5\,\text{GeV}$ | | $\geq 1$ EM<br>$E_T^e > 15\,\text{GeV}$<br>$\lvert\eta^e\rvert < 2.5$<br>$\geq 1$ JET<br>$E_T^j > 10\,\text{GeV}$<br>$\lvert\eta^j\rvert < 2.5$<br>$\not{E}_T > 14\,\text{GeV}$ |
| EM1_EISTRKCC_MS<br>Run 70000 to 85276 | $\geq 1$ EM<br>$E_T^e > 12\,\text{GeV}$ | | $\geq 1$ EM<br>$E_T^e > 20\,\text{GeV}$<br>$\not{E}_T > 15\,\text{GeV}$ |
| EM1_EISTRKCC_MS<br>after Run 85277 | $\geq 1$ EM<br>$E_T^e > 10\,\text{GeV}$ | $\geq 1$ EM<br>$E_T^e > 15\,\text{GeV}$ | $\geq 1$ EM<br>$E_T^e > 20\,\text{GeV}$<br>$\not{E}_T > 15\,\text{GeV}$ |

Table 4.1: Summary of two triggers used in the analysis.

- L2: This trigger required an EM cluster with $E_T > 20\,\text{GeV}$ and $\not{E}_T > 15\,\text{GeV}$. The EM cluster had to pass the standard shape cuts and an isolation requirement with $\mathcal{R}_{iso} = 0.4$. If it was in the $|\eta| < 1.3$ range, a matching track pointing to the EM cluster within $\Delta\eta = \pm 0.03$ and $\Delta\phi = \pm 0.03$ was also required.

Both triggers were very stable throughout the entire 1B run. The $\not{E}_T$ threshold and the $E_T$ cutoff of the electron in EM1_EISTRKCC_MS were more restrictive than those in ELE_JET_HIGH, so EM1_EISTRKCC_MS did not add many events to the data sample (i.e., did not improve the efficiency much) in higher jet multiplicity cases. Although EM1_EISTRKCC_MS was prescaled

in a few runs, the luminosity for these prescaled data was almost negligible compared to the whole Run 1B luminosity.

The inefficiency of the triggers mostly came from the $\not{E}_T$ requirement in L2. The trigger efficiency is discussed in section 4.4.2.

## 4.2 Offline Event Selection

The Run 1B raw data were collected on magnetic tapes and reconstructed on the UNIX nodes by the DØ reconstruction program DØRECO (version 12). The reconstructed data were separated into streams corresponding to physics interests using the online trigger tags and some reconstructed information. The streamed data in a condensed format were made available on disks.

Before applying any physics selection criteria, some "bad data" are removed right away. The rejected data include:

- Bad Runs: Typical reasons for entering a run in the bad run list were online data acquisition problems, or detector hardware failure during the run time, for example, electronic problems of the calorimeter or tracking chamber high voltage being down.

- Special Runs: These runs were taken for special purposes, such as upslion or direct photon studies, and used very different trigger lists which were not expected to be efficient for $t\bar{t}$ study.

- Micro-blanked Events: Since the Main Ring passes through the DØ hadronic calorimeter, each time Main Ring batches coasting through the

DØ detector were in coincidence with a Tevatron beam crossing, there was an energy blast in the calorimeter and muon system. As a result, the event had to be thrown away. This led to a total luminosity loss of about 9%.

The final integrated luminosity for this analysis is $\int \mathcal{L}dt = 74.9\,\mathrm{pb}^{-1}$ with a standard DØ luminosity uncertainty of 5.4% [54].

### 4.2.1 Inclusive $W \rightarrow e\nu$ Events

Since the data set for the $t\bar{t}$ to electron plus jets is part of the inclusive $W \rightarrow e\nu$ production, we select events with an isolated electron and considerable $\not\!\!E_T$. The electron candidates have to pass "tight electron" cuts (see section 3.3.2), and the following $W$ boson offline selection criteria are applied:

- The electron $E_T$ and the $\not\!\!E_T$ threshold: Fig. 4.1 shows electron $E_T$ and $\not\!\!E_T$ distributions from the $W$ and $t\bar{t}$ ($m_t = 180\,\mathrm{GeV}$ ) Monte Carlos. Both distributions peak at about 40 GeV (half of the $W$ mass), leading us to use the following thresholds:

$$E_T(e) > 20\,\mathrm{GeV}, \tag{4.1}$$

$$\not\!\!E_T > 20\,\mathrm{GeV}. \tag{4.2}$$

- The $\eta$ range of the electron: Most of the background to the leptonic $W$ comes from a hadronic jet whose calorimeter energy deposits fluctuated to pass the tight electron cuts. Such "fake" electrons are more severe in

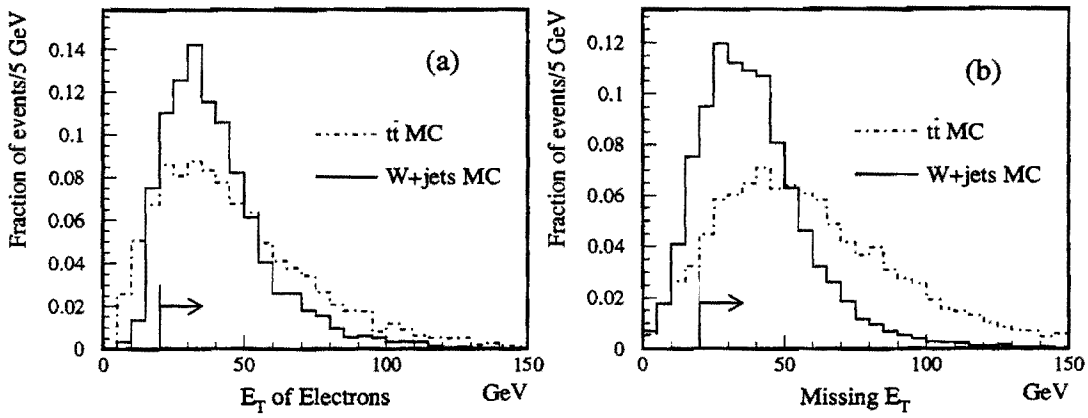


Figure 4.1: (a) The electron $E_T$ distribution and (b) The $\not\!\!E_T$ distribution from the $W$ MC (solid line) and $t\bar{t}$ ($m_t = 180$ GeV) MC (dashed line).

the high $\eta$ region. Since the $W$'s from $t\bar{t}$ decays and the electrons from their decays tend to be in the central region, we require the electrons to satisfy:

$$|\eta(e)| < 2.0\,. \tag{4.3}$$

- Events with two or more electrons that pass the "loose electron" cuts and the kinematic selections mentioned above, are rejected because they are possibly $Z$ bosons, $W^+W^-$, or $t\bar{t} \to ee$ candidates.

There are a total of 56043 single $W \to e\nu$ inclusive events. Their transverse mass distribution is shown in Fig. 4.2. A clear Jacobian peak is observed around the $W$ mass. Of course, most of the events are not coming from $t\bar{t}$'s. The topological difference between the $t\bar{t}$ signals and the $W$ background is that each $t\bar{t}$ decay has four high $E_T$ quark jets in addition to the leptonically decaying $W$, while the number of inclusive $W$ events decreases exponentially

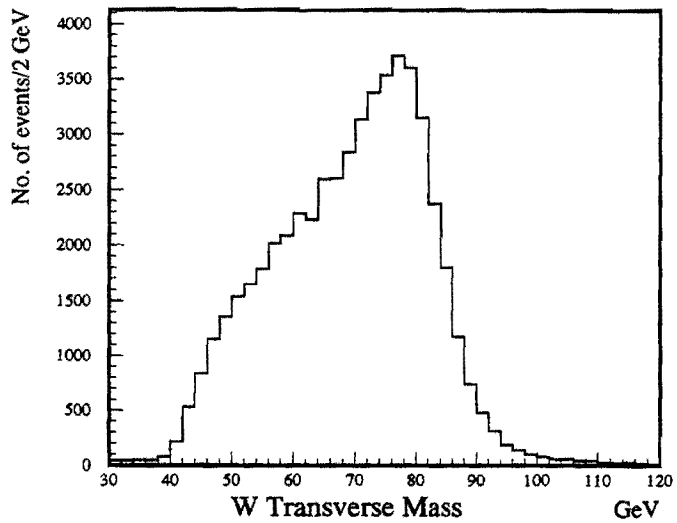


Figure 4.2: The transverse mass distribution of the $W$ data.

with jet multiplicity. Hence, picking events with large high $E_T$ jet multiplicity sharply improves the signal to background ratio.

Fig. 4.3 shows the $E_T$ distributions for the four leading jets from the $t\bar{t}$ ($m_t = 180\,\mathrm{GeV}$) MC and Fig. 4.4 shows the corresponding $E_T$ distribution from the inclusive $W$ data. If we increase the $E_T$ threshold of the jets to $20\,\mathrm{GeV}$ and require at least 3 jets in an event, more than 80% of $t\bar{t}$'s and only about 0.04% of all the $W$'s survive the requirement. Moreover, the jets from $t\bar{t}$ decays tend to be in the central (low $|\eta|$) region, while the data show many jets near the beam direction (high $|\eta|$ region) which are probably mainly background.

Fig. 4.5(a) compares the $\eta$ distributions of jets (with $E_T > 20\,\mathrm{GeV}$) from $t\bar{t}$ MC and inclusive $W$ data. Fig. 4.5(b) shows the relative detection efficiency as a function of $|\eta|$ for these two cases. If we require $|\eta| < 2$, almost no $t\bar{t}$ events are lost, but approximately 10% of the $W$ events are cut. So, we apply

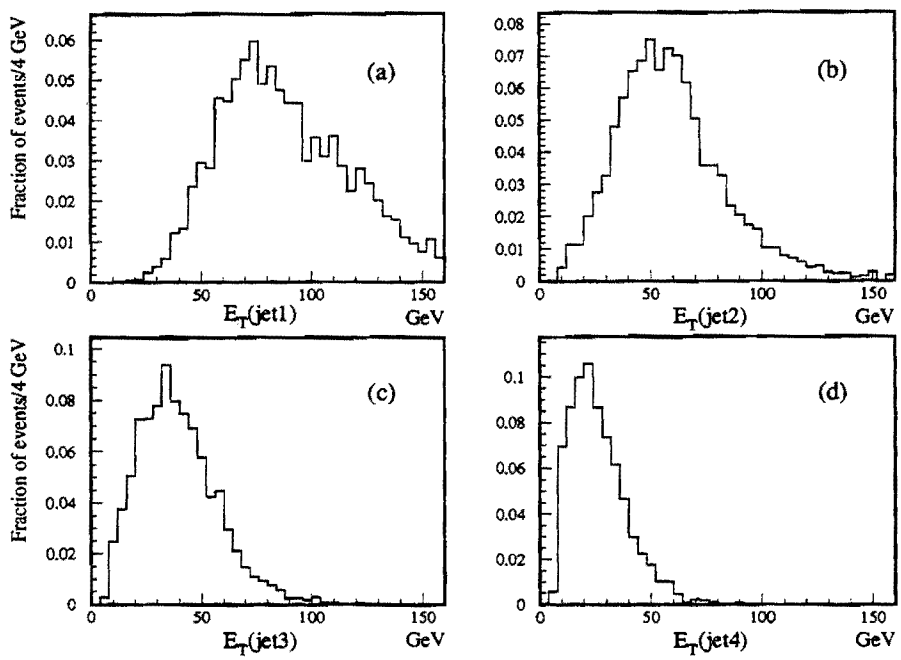


Figure 4.3: (a-d) The $E_T$ of the first 4 leading jets from $t\bar{t}$ MC ($m_t = 180$ GeV).

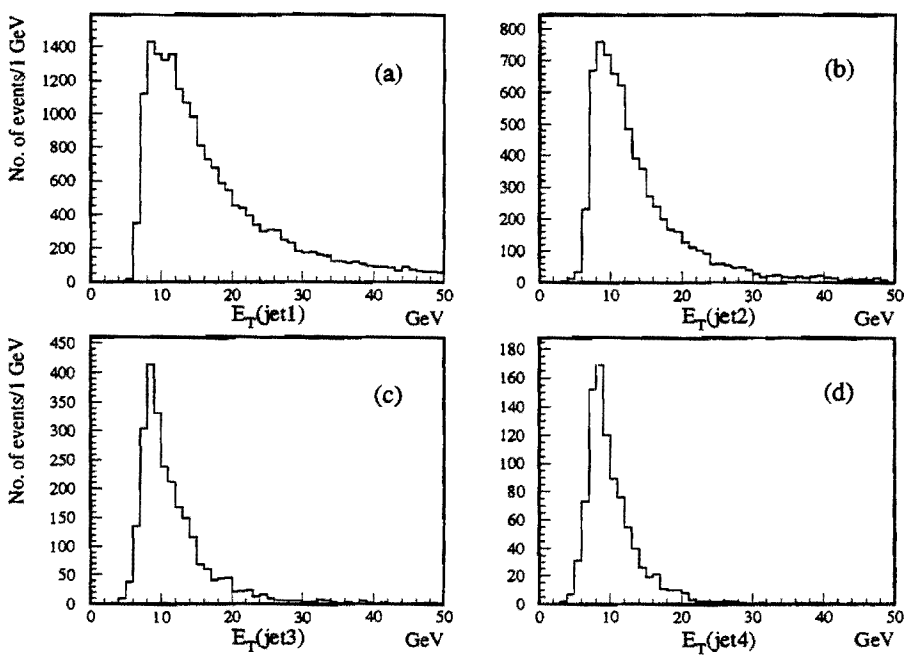


Figure 4.4: (a-d) The $E_T$ of the first 4 leading jets from inclusive $W$ events.

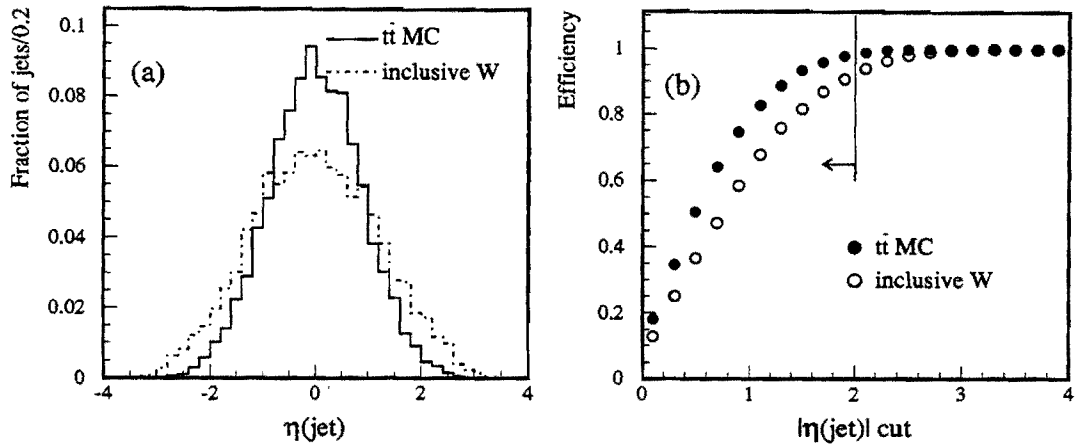


Figure 4.5: (a) $\eta$ distributions of jets from the $t\bar{t}$ MC (solid line) and inclusive $W$ data (dashed line). (b) The efficiency of $\eta$ cuts for both samples.

the cuts

$$E_T(jet) > 20\,\mathrm{GeV}\,, \tag{4.4}$$

$$|\eta(jet)| < 2.0\,. \tag{4.5}$$

Table 4.2 lists the number of inclusive $W$ candidates according to their jet multiplicities ($N_{jet}$). The $t\bar{t}$ candidates in the inclusive $W$ events come from the set of $N_{jet} \geq 3$. We do not choose $N_{jet} \geq 4$ because the efficiency of $N_{jet} \geq 4$ is somewhat low and strongly dependent on the top mass used in the MC.

### 4.2.2 Sources of Background in the $W \rightarrow e\nu$ Events

The major background in the $W \rightarrow e\nu$ data set are QCD events with either misidentified ("fake") electrons or real electrons from semileptonic decay of heavy quarks. Other sources of background are mainly $W \rightarrow \tau\nu$ followed by

| Jet Multiplicity | No. of Events |
|---|---|
| $\geq$ 0 Jet | 56043 |
| $\geq$ 1 Jet | 6139 |
| $\geq$ 2 Jets | 983 |
| $\geq$ 3 Jets | 159 |
| $\geq$ 4 Jets | 25 |

Table 4.2: Inclusive jet multiplicity of $W$ candidate events. Jets are required to have $E_T > 20\,\mathrm{GeV}$ and $|\eta| < 2$.

$\tau \rightarrow e\nu\nu$, $Z \rightarrow \tau\tau$ with one of the $\tau$ leptons decaying to an electron, $Z \rightarrow ee$ with one of electrons undetected, and $W^+W^-$ pair or $WZ$ production with one $W$ decaying to $e\nu$.

### (1) QCD background

In the previous chapter we mentioned fake electron problems. In addition, an electron from heavy quark semileptonic decay may also accidently pass the isolation requirement and be misidentified as a $W \rightarrow e\nu$ event. The events from both processes usually have a relatively low $\not\!\!E_T$ compared to that from a leptonically decaying $W$. We do not distinguish them in estimating the QCD background.

In addition to the electron ID selection, $W$ identification depends on the $\not\!\!E_T$ requirement. The Monte Carlo (Fig. 4.1) indicates that the $\not\!\!E_T$ distribution of $W$ events has broad peak at 40 GeV. On the other hand, QCD multijet events in general have little $\not\!\!E_T$. Sometimes instrumental effects such as noisy cells and energy measurement fluctuations in the calorimeter can cause imbal-

anced (missing) $E_T$ in the event. Usually the fake rate per jet is roughly a constant. Hence, the more jets a $W$ candidate has, the more probable it is to be a QCD fake. Because there is no single unbiased trigger which is appropriate for all different values of $N_{jet}$, we have to concentrate on events which have $N_{jet} \geq 3$; events with $N_{jet} < 3$ can be studied by the same method with a different trigger.

We first select events which pass the following preliminary requirements:

- Tagged by GIS_DIJET Level 2 filter.
- A reconstructed electron candidate (PELC) with $E_T > 20\,\mathrm{GeV}$.
- $N_{jet} \geq 3$

GIS_DIJET triggers on an EM cluster with $E_T$ higher than 15 GeV and two more jets with $E_T$ greater than 15 GeV. Since there is no $\not\!\!E_T$ requirement for this trigger, it can provide an unbiased $\not\!\!E_T$ distribution. Although GIS_DIJET is not a signal trigger, approximately 90% of $W + 3$jets candidates also fire the trigger. Since we are only interested in $W$ events and their background, $Z \rightarrow ee$ and diboson events are excluded in the sample by rejecting those events which have two electron candidates passing "loose electron" cuts.

We then use the following two samples to estimate the QCD background.

- Tight electron sample: Events with a PELC passing tight electron cuts. This sample is mixed with electron signal and background. In the low $\not\!\!E_T$ region, this sample is dominated by background. Only events with $\not\!\!E_T > 20\,\mathrm{GeV}$ meet the requirements of a $W$ candidate. We obtain a

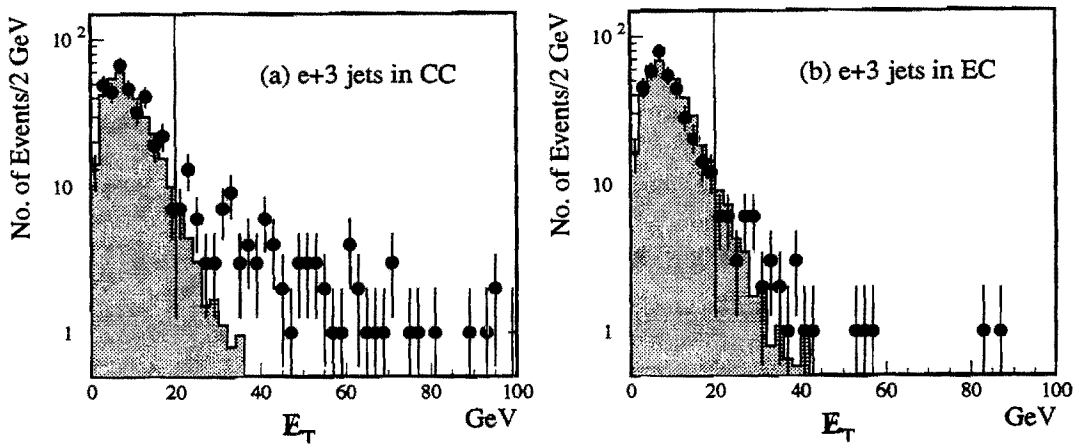


Figure 4.6: $\not{E}_T$ distribution for (a) tight electron events (solid dots), and (b) "fake electron" events (shaded histogram). Events have to be tagged by GIS_DIJET trigger and have $N_{jet} \geq 3$. The fake electrons are normalized to the tight electrons for $\not{E}_T < 10$ GeV.

total of 152 $W$ candidate events, of which 140 events also fired the signal triggers.

- Fake electron sample: Events which have a PELC with the electron likelihood $\mathcal{L}_e > 1.5$ if it is in the Central Calorimeter (CC) or $\mathcal{L}_e > 2.0$ if it is in the End Calorimeter (EC). This sample only has a small fraction ($\sim$ 1%) of the $W \rightarrow e\nu$ events, so it is totally dominated by QCD processes with quark and gluon jets.

We can normalize the fake electron sample to the tight electron sample in the low $\not{E}_T$ region. After the normalization, the QCD contamination of the $W$ candidates is the number of events with $\not{E}_T > 20$ GeV in the normalized fake sample. We then calculate the background fraction $f_{bkg}$ as

$$f_{bkg} = \frac{N_{tight}(\not{E}_T < E_{norm})}{N_{fake}(\not{E}_T < E_{norm})} \cdot \frac{N_{fake}(\not{E}_T > 20)}{N_{tight}(\not{E}_T > 20)}, \tag{4.6}$$

where the first factor is the normalization factor for $\not\!\!E_T < E_{norm}$, $N_{tight}$ and $N_{fake}$ are the number of events in the tight and fake electron sample respectively. We further subdivide the event samples according to the PELC's in the CC or EC fiducial region. We compare two different values of $E_{norm}$ (10 GeV and 16 GeV) to estimate the systematic error in the normalization. The results are shown in Table 4.3.

| $E_{norm}$ (GeV) | QCD $f_{bkg}$ in the CC (%) | QCD $f_{bkg}$ in the EC (%) |
|---|---|---|
| 10 | $23.1 \pm 3.4$ (stat) | $70.5 \pm 12.6$ (stat) |
| 16 | $23.3 \pm 3.3$ (stat) | $65.1 \pm 11.4$ (stat) |

Table 4.3: QCD background estimate for $W + 3$ or more jets.

The background fraction is significantly higher for electrons in the EC than in the CC. There is about 1% (8%) uncertainty from the selection of $E_{norm}$ for electrons in CC (EC); we use the average value as the final results. Since this study uses a different trigger from the signal triggers (and the overlap is about 90%), when we propagate the result to the signal sample, an additional 10% uncertainty is assigned.

For $N_{jet} \geq 0$ and $N_{jet} \geq 1$ cases, we use a combination of ELE_1_MON and EM1_ELE_MON triggers to study this background. Both triggers require an EM cluster with minimum $E_T$ of 16 GeV and 20 GeV respectively. The number of background events in the signal sample is estimated by multiplying the number of candidate events in the CC and the EC by the background fraction $f_{bkg}$ in that fiducial region individually then summing them up. The uncertainties are calculated by adding statistical errors and the systematic

| Data Type | QCD $f_{bkg}$ in the CC (%) | QCD $f_{bkg}$ in the EC (%) | No. of QCD Background in the Signal Sample |
|---|---|---|---|
| $N_{jet} \geq 0$ | $1.75 \pm 0.18$ | $11.2 \pm 1.2$ | $2009 \pm 207$ |
| $N_{jet} \geq 1$ | $9.21 \pm 1.05$ | $49.3 \pm 7.2$ | $1112 \pm 135$ |
| $N_{jet} \geq 2$ | $15.5 \pm 1.9$ | $60.0 \pm 8.2$ | $271 \pm 32$ |
| $N_{jet} \geq 3$ | $23.2 \pm 4.1$ | $67.8 \pm 15.3$ | $58.3 \pm 9.6$ |

Table 4.4: QCD background estimate for the inclusive $W$ + jets sample.

uncertainties from normalization and trigger effects in quadrature. The results are shown in Table 4.4.

**(2)** $W \rightarrow \tau \rightarrow e$

The electron from $W \rightarrow \tau \rightarrow e$ is much softer than the electron from direct $W$ decay, and the transverse mass distribution no longer has a Jacobian peak at half the $W$ mass. Assuming that the decay rate of $W \rightarrow \tau\nu$ is the same as that of $W \rightarrow e\nu$ and that the branching ratio for $\tau \rightarrow e\nu\nu$ is 17.9%, the background percentage of $W \rightarrow e\nu$ is

$$\begin{aligned} f &= 17.9\% \times \frac{A_\tau}{A_e} \\ &= 17.9\% \cdot \frac{(11.98 \pm 0.16)\%}{(58.11 \pm 0.61)\%} \\ &= 3.69\% \pm 0.06\%, \end{aligned} \tag{4.7}$$

where the kinematic acceptance $A_\tau$ for $W \rightarrow \tau \rightarrow e$ and $A_e$ for $W \rightarrow e\nu$ are given by the Monte Carlo.

**(3)** $Z \to \tau\tau$

The cross section for $Z \to \tau\tau$ is almost the same as for $Z \to ee$, which is about 10 times smaller than the $W \to e\nu$. The electron from the $\tau$ decay has a softer $p_T$ spectrum as in the previous case. This background is estimated to be less than 1% of the $W$ + jets background.

**(4)** $Z \to ee$

Events from $Z \to ee$ in which one electron either goes into a crack in the detector, or fails the loose electron cut, or is not in our kinematic acceptance region, are also a background. Most cases of $Z$ production have small $\not{E}_T$ but sometimes it can fluctuate and become bigger than our 20 GeV requirement. We generate Monte Carlo $Z$ events with full detector simulation, then normalize the luminosity of events to the data and use the efficiency of electron detection from data. This source yields $6.9 \pm 1.5$ events in the $N_{jet} \geq 3$ sample.

**(5)** $W^+W^-$ **and** $WZ$ **events**

The theoretically predicted cross section for $W^+W^-$ production is about 9.9 pb and for $WZ$ is about 2.8 pb, both of which are much smaller than the single $W$ production of 20 nb. From a Monte Carlo study we estimate $2.9 \pm 1.0$ events in the $N_{jet} \geq 3$ sample.

### 4.2.3 Search for $t\bar{t}$ by Soft Muon Tagging

Soft muon tagging is intended to identify muons from the $b$ or $c$ quark decays. Each $t\bar{t}$ decay has two $b$ quarks, and in the $e+$jets channel one $W$ has 50% chance to decay to a $c$ quark. From the fact that the branching ratio of $b \to \mu X$ is about 20% (including cascade decays, $b \to c \to \mu X$) and that of $c \to \mu X$ is about 10%, approximately 40% of $t\bar{t} \to e+$jets events may have tagged muons. In the main background processes, namely $W+$jets and QCD multijet production, tagged muons are much fewer so that $\mu$-tag provides an effective method to reduce the background.

The tagged muons first have to pass offline standard cuts (described in the previous chapter) and be contained in the central muon (CF) system ($|\eta| \lesssim 1.0$). To find a way to further suppress the background, we compare the tagged muons in the $t\bar{t}$ and $W+$jets Monte Carlo events. The major sources of muons in $W+$jets events result from heavy quark ($b$ or $c$) decays and $\pi/K$ decays. Other potential background sources, such as cosmic rays, combinatorics and hadronic punchthrough, are estimated to be much smaller ($\sim 4\%$). The following kinematic cuts are employed:

- The $p_T$ of muons: A muon passing through the calorimeter and iron toroids needs a minimum $p_T$ of about 3 GeV. The low $p_T$ muons usually have poor reconstruction efficiency and higher fake background; moreover, Fig. 4.7 shows the low $p_T$ region has severe muon background from $\pi/K$ decay, so we require

$$p_T(\mu) > 4\,\mathrm{GeV}\,. \tag{4.8}$$

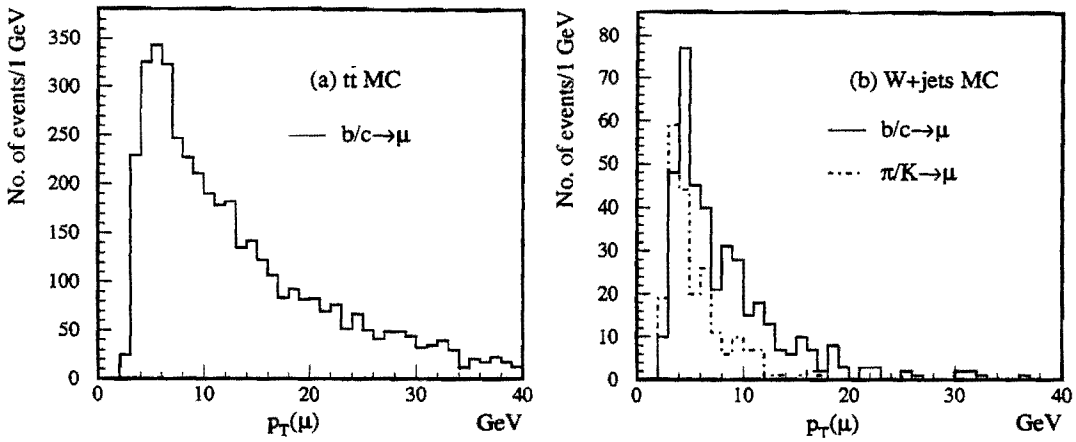


Figure 4.7: Muon $p_T$ distribution of (a) $t\bar{t}$ MC ($m_t = 180\,\text{GeV}$) and (b) $W$ + jets MC. Two major muon sources in $W$ + jets events are $b/c$ decays (solid line) and $\pi/K$ decays (dashed line).

- The separation between a muon and the nearest jet ($\Delta R_{\mu j}$): A muon from $b$ or $c$ quark decay is part of the hadronic jet, and is expected to be found in its proximity. The $\Delta R_{\mu j}$ is defined as the distance between the muon and its nearest jet in $\eta$–$\phi$ space. The distributions are shown in Fig. 4.8. The requirement is

$$\Delta R_{\mu j} < 0.5\,. \tag{4.9}$$

  This cut is used to distinguish isolated muons from $W$ or $Z$ decays, and also reduces the background from cosmic rays and combinatorics.

- The transverse momentum of the tagged jet ($E_T^{tag}$): The Monte Carlo study (see Fig. 4.9) shows the $E_T^{tag}$ from $t\bar{t}$ decay is higher than that from $W$ + jets. We look for $t\bar{t}$ signals in inclusive $W$ events with $N_{jet} \geq 3$ in

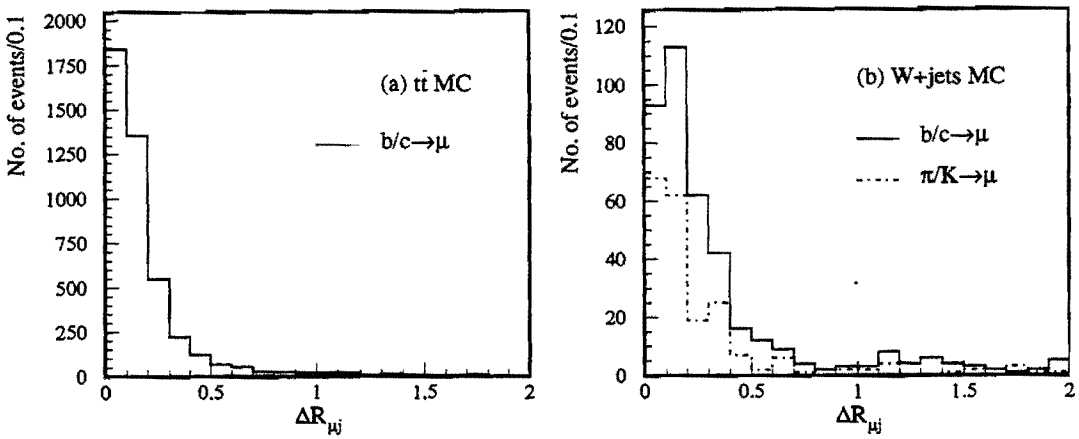


Figure 4.8: Muon-jet separation ($\Delta R_{\mu j}$) of (a) $t\bar{t}$ MC ($m_t$ = 180 GeV) and (b) $W$ + jets MC.

which each jet has minimum $E_T$ of 20 GeV. It is natural to impose the same requirement on the transverse momentum of the tagged jet, so we have

$$E_T^{tag} > 20\,\text{GeV}\,. \tag{4.10}$$

Approximately 15% of $t\bar{t}$ events have an observed muon tag and only less than 1.3% of $W + 3$ or more jets events have an observed muon tag. The sources of tagged muons in $W$ MC include 75% from $b/c$ quark decays and 25% from $\pi/K$ decays.

### 4.2.4 Additional Cuts

$\not{E}_T$ is a important signature for a leptonically decaying $W$ and the most effective way to reject the QCD background. In a $\mu$-tag event, however, both the $\mu$ and $\nu_\mu$ may also cause considerable $\not{E}_T$. Fig. 4.10 shows the $\mu$ tagging

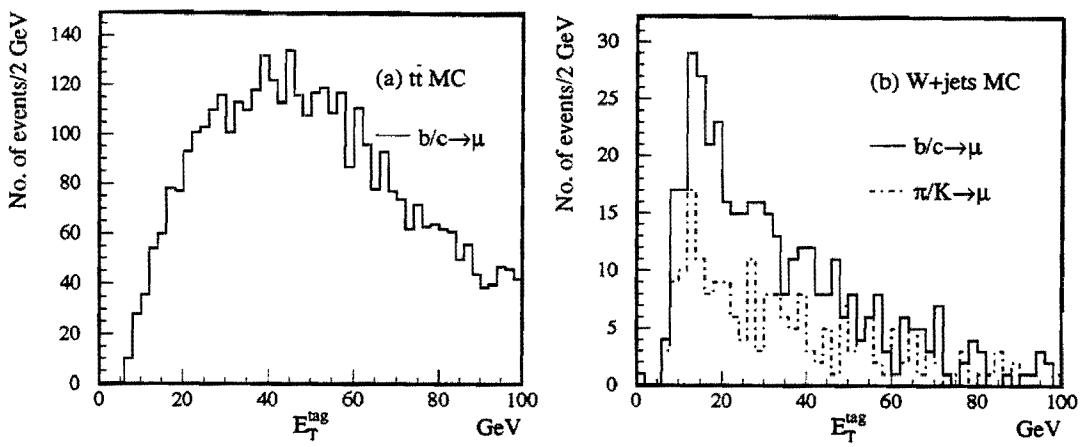


Figure 4.9: Tagged jet $E_T$ ($E_T^{tag}$) distribution of (a) $t\bar{t}$ MC ($m_t = 180\,\text{GeV}$) and (b) $W$ + jets MC.

rate per event increasing with $\not\!\!E_T$ in QCD multijet events. This fact indicates that the $\mu$ and the accompanying $\nu_\mu$ make a large contribution to $\not\!\!E_T$. Since the extra $\not\!\!E_T$ is correlated with the tagged muon, it tends to be parallel to the muon $\phi$ direction. This can be seen in Fig. 4.11, which shows the correlation of $\not\!\!E_T$ with the $\phi$ separation of the $\not\!\!E_T$ and the muon ($\Delta\phi(\mu, \not\!\!E_T)$). Most QCD multijet events are located in the small $\not\!\!E_T$ or the small $\Delta\phi(\mu, \not\!\!E_T)$ region. Therefore, in addition to the $\not\!\!E_T > 20\,\text{GeV}$ cut, we require

$$\Delta\phi(\not\!\!E_T, \mu)/80^\circ + \not\!\!E_T/40\,\text{GeV} > 1\,. \tag{4.11}$$

(See the contour cut shown in Fig. 4.11.) This cut can further reject about 40% of the QCD background, and less than 2% of $W$ + jet or $t\bar{t}$ events are lost.

Finally, the jets from high mass top decay are expected to be more ener-

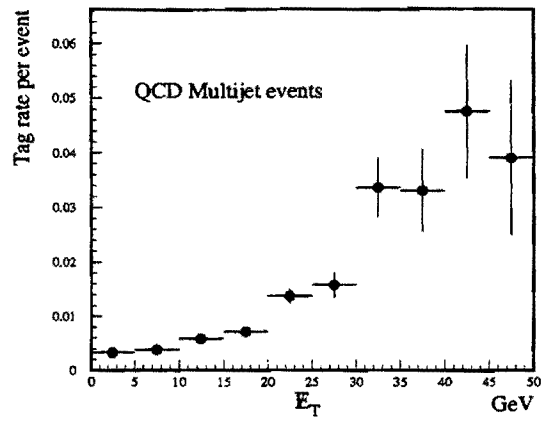


Figure 4.10: Muon tagging rate per event as a function of $\not\!\!E_T$. The increasing rate with $\not\!\!E_T$ implies tagged events have extra $\not\!\!E_T$ and need to be handled properly.

getic than the jets in $W$ or QCD multijet events. We, thus, define $H_T$ as

$$H_T = \sum_{jet=1}^{N_{jet}} E_T(jet)\,, \tag{4.12}$$

where the jets have to pass the kinematic cuts (4.4) and (4.5). Fig. 4.12 shows the $H_T$ distributions of QCD multijet events, $W + 3$ or more jets MC, and $t\bar{t}$ MC with top mass $m_t = 140$, and 180 GeV. The $H_T$ distribution is strongly correlated with the top mass; it is very effective to discriminate background in the high mass top case. However, a tight $H_T$ cut also may somewhat bias the mass fitting. We keep two sets of cuts; in the Standard Set we require

$$H_T > 120\,\mathrm{GeV}\,, \tag{4.13}$$

and in the Loose Set there is no $H_T$ requirement. The summary of event selections is listed in Table 4.5.

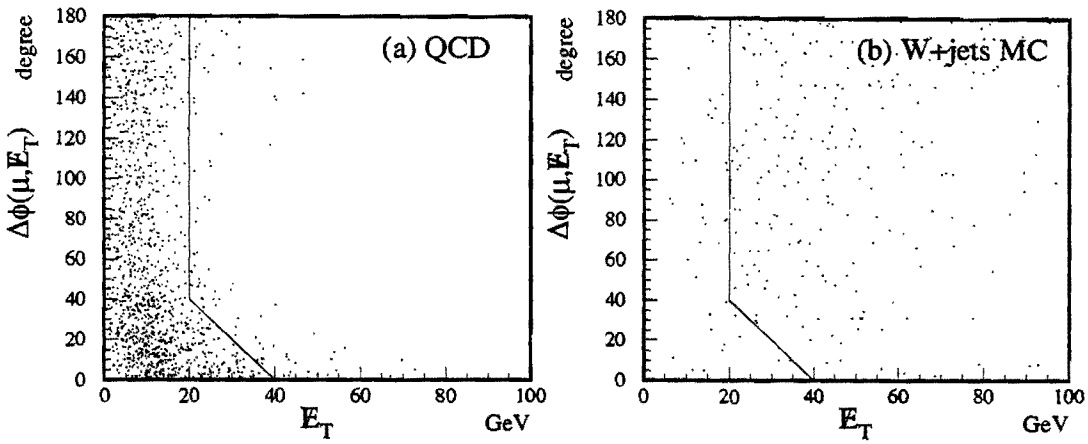


Figure 4.11: The correlation of the angle $\Delta\phi$ between the $\not{E}_T$ and the tagged muon with the $\not{E}_T$ for (a) QCD multijet background events and (b) $W$+jets Monte Carlo.

### 4.2.5 Candidate events

There are 5 events passing loose cuts, and 4 of them survive the final standard selection criteria. Table 4.6 lists the characteristics of these 5 events. Each event has been examined by the DØ display program. One intriguing candidate #85129/19079 is shown on Fig. 4.13. The upper side is the "lego" plot which displays reconstructed objects in the $\eta$–$\phi$ space. There are four high $E_T$ distinct jets in the Central Calorimeter, one of which ($\eta = 0.04$, $\phi = 3.59$) is tagged by a $\mu^+\mu^-$ pair. The other plot shows the top view of the whole event in which the tracks of the muon pair and the associated jet are illustrated. The high $E_T$ ($E_T = 43\,\text{GeV}$) electron is fully isolated ($f_{iso} = 0.0062$), and its shower was purely developed in the EM Calorimeter ($f_{EM} = 100\%$). The transverse mass of the electron and $\not{E}_T$ is 69.3 GeV, a very likely value for a leptonically decaying $W$. All these characteristics are also present in other candidate events.

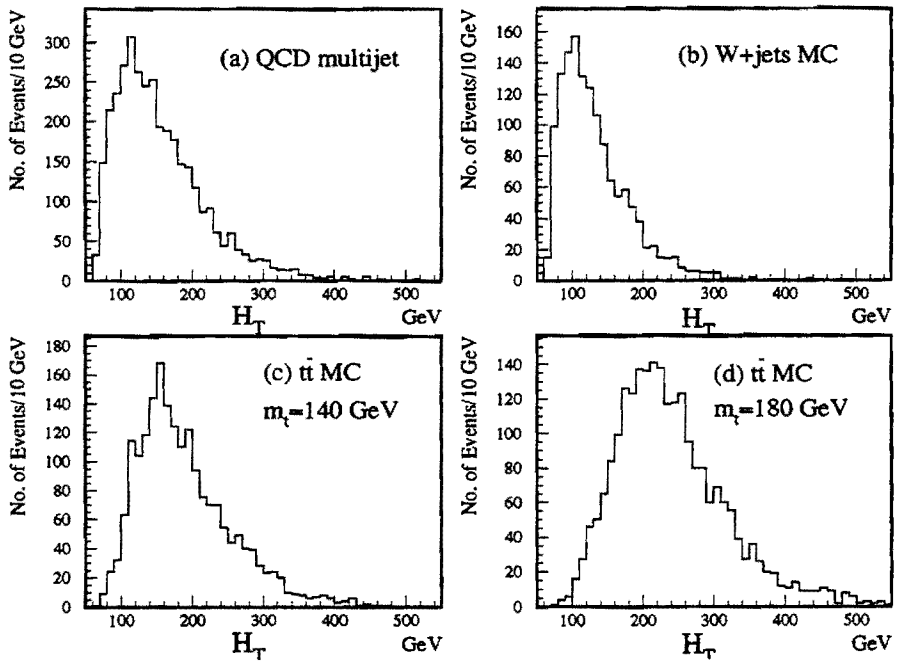


Figure 4.12: $H_T$ distribution of (a) QCD multijet events, (b) $W$ + jets MC, (c) $t\bar{t}$ MC with $m_t = 140$ GeV, and (d) $t\bar{t}$ MC with $m_t = 180$ GeV.

| Requirement | | Standard Set | Loose Set |
|---|---|---|---|
| | $\not\!\!E_T$ | $> 20$ GeV | $> 20$ GeV |
| Electron | $E_T(e)$ | $> 20$ GeV | $> 20$ GeV |
| | $\lvert\eta(e)\rvert$ | $< 2.0$ | $< 2.0$ |
| | $E_T(jet)$ | $> 20$ GeV | $> 20$ GeV |
| Jet | $\lvert\eta(jet)\rvert$ | $< 2.0$ | $< 2.0$ |
| | $N_{jet}$ | $\geq 3$ | $\geq 3$ |
| | $p_T(\mu)$ | $> 4$ GeV | $> 4$ GeV |
| | $\lvert\eta(\mu)\rvert$ | $\lesssim 1.0$ (in CF) | $\lesssim 1.0$ (in CF) |
| $\mu$-tag | $\Delta R_{\mu j}$ | $< 0.5$ | $< 0.5$ |
| | $E_T^{tag}$ | $> 20$ GeV | $> 20$ GeV |
| | $\Delta\phi(\not\!\!E_T, \mu)$ | $\Delta\phi/80 + \not\!\!E_T/40 > 1$ | $\Delta\phi/80 + \not\!\!E_T/40 > 1$ |
| | $H_T$ | $> 120$ GeV | — |

Table 4.5: Summary of kinematic requirements for event selections.

| 84681/13015 | | | | 87987/1228 | | | |
|---|---|---|---|---|---|---|---|
| | $E_T$ (GeV) | $\eta$ | $\phi$ | | $E_T$ (GeV) | $\eta$ | $\phi$ |
| electron | 64.7 | -0.82 | 3.51 | electron | 69.7 | 0.57 | 0.92 |
| $\not\!\!E_T$ | 64.5 | - | 6.14 | $\not\!\!E_T$ | 58.0 | - | 4.61 |
| jet 1 (tag) | 62.6 | -0.40 | 0.07 | jet 1 | 46.3 | -1.39 | 1.95 |
| jet 2 | 60.2 | 0.46 | 2.82 | jet 2 (tag) | 42.0 | 0.09 | 4.76 |
| jet 3 | 22.5 | 1.69 | 3.33 | jet 3 | 22.1 | 0.25 | 3.36 |
| tagged $\mu^+$ | 22.1 | -0.48 | 6.22 | tagged $\mu^+$ | 14.6 | 0.08 | 4.77 |
| $H_T$ | 145.4 | | | $H_T$ | 110.4 | | |
| 85129/19079 | | | | 89372/12467 | | | |
| | $E_T$ (GeV) | $\eta$ | $\phi$ | | $E_T$ (GeV) | $\eta$ | $\phi$ |
| electron | 43.0 | 0.60 | 5.20 | electron | 130.8 | 0.33 | 0.91 |
| $\not\!\!E_T$ | 29.9 | - | 1.55 | $\not\!\!E_T$ | 62.2 | - | 1.32 |
| jet 1 | 46.3 | -0.87 | 3.24 | jet 1 | 181.7 | -0.27 | 4.35 |
| jet 2 (tag) | 39.7 | 0.04 | 3.59 | jet 2 | 44.1 | -1.52 | 4.19 |
| jet 3 | 28.8 | 0.21 | 0.93 | jet 3 | 27.2 | 0.46 | 2.01 |
| jet 4 | 21.6 | -0.50 | 5.85 | jet 4 (tag) | 20.6 | -0.44 | 1.36 |
| tagged $\mu^-$ | 6.0 | -0.01 | 3.45 | tagged $\mu^+$ | 17.3 | -0.30 | 1.32 |
| tagged $\mu^+$ | 5.6 | 0.00 | 3.58 | $H_T$ | 273.5 | | |
| $H_T$ | 136.4 | | | | | | |
| 91206/13727 | | | | | | | |
| | $E_T$ (GeV) | $\eta$ | $\phi$ | | | | |
| electron | 97.0 | -0.70 | 6.11 | | | | |
| $\not\!\!E_T$ | 23.1 | - | 0.72 | | | | |
| jet 1 (tag) | 160.5 | -0.48 | 3.47 | | | | |
| jet 2 | 95.3 | -0.78 | 0.46 | | | | |
| jet 3 | 46.1 | 0.36 | 3.14 | | | | |
| tagged $\mu^-$ | 12.2 | -0.85 | 3.50 | | | | |
| $H_T$ | 301.9 | | | | | | |

Table 4.6: Characteristics of the 5 top candidate events which pass the Loose Set of cuts. Event #87987/1228 fails the Standard Set of cuts because it does not satisfy the $H_T$ requirement.

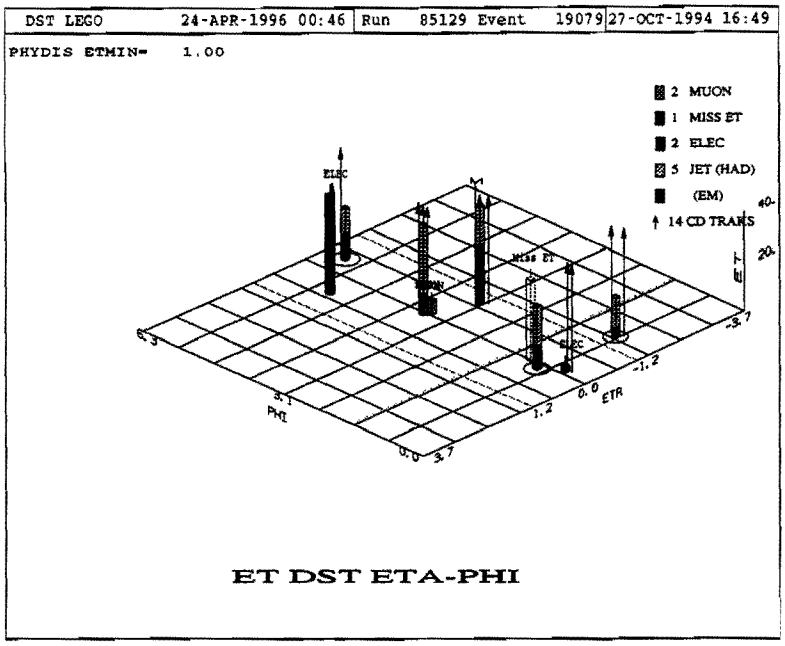


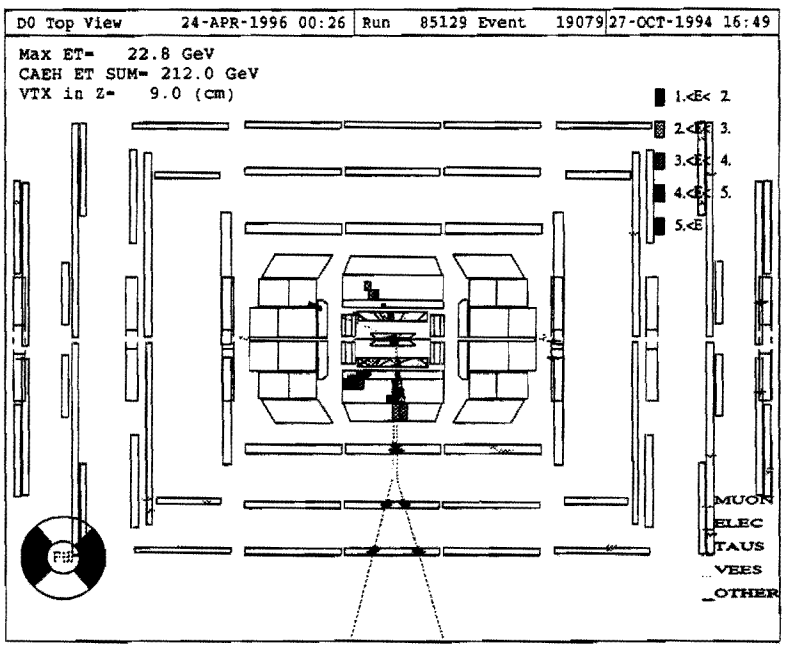


Figure 4.13: Display of event #85129/19079.

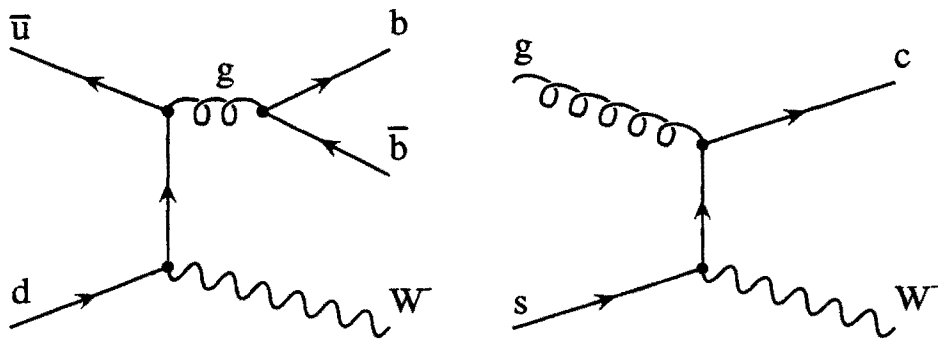


Figure 4.14: Typical Feynman diagrams contributing to heavy quark production with $W$ bosons: (a) gluon splitting to $b\bar{b}$ pair and (b) single charm production.

## 4.3 Backgrounds in $e + \text{jets} + \mu-\text{tag}$

As discussed before, QCD multijet events and $W+$jets are major background to the signal. We estimate them directly from the collider data. The other small backgrounds, such as $WW$, $WZ$ and $Z \to \tau\tau \to e\mu$, are determined by a combination of Monte Carlo simulation and offline efficiencies from the data results.

### 4.3.1 QCD Background

In Section 4.2.2 we estimated the QCD background in $W+$jets events. To further calculate the QCD contamination after $\mu$-tag, $\Delta\phi(\mu, \not{E}_T)$ and $H_T$ cuts, we use the normalized fake electron sample in Section 4.2.2 to measure the rate of QCD events passing all these cuts. The performance of the muon chambers changed during the course of the run. Since this background estimation uses data throughout the whole 1B collider run, this effect is already included. The results are listed in Table 4.7.

| Cuts | No. of QCD Background Remaining in the inclusive $W$ + jets Sample | | | |
|---|---|---|---|---|
| | $N_{jet} \geq 1$ | $N_{jet} \geq 2$ | $N_{jet} \geq 3$ | $N_{jet} \geq 3$ & $H_T > 120$ |
| $N_{QCD}$ | $1112 \pm 135$ | $271 \pm 32$ | $58.3 \pm 9.6$ | $39.4 \pm 6.5$ |
| $\mu$-tag | $13.3 \pm 1.8$ | $4.54 \pm 0.69$ | $1.54 \pm 0.36$ | $1.06 \pm 0.28$ |
| $\Delta\phi(\mu, \not{E}_T)$ cut | $4.78 \pm 0.74$ | $2.00 \pm 0.37$ | $0.97 \pm 0.26$ | $0.61 \pm 0.20$ |

Table 4.7: QCD background estimate for the inclusive $W$ + jets data sample after $\mu$-tag. $N_{QCD}$ is the number of QCD background estimation before $\mu$-tag (see Table 4.4).

### 4.3.2 $W$ + jets Background

Whatever $W$ bosons that do not come from $t$ decays but from other processes comprise this background. Fig 4.14 shows typical Feynman diagrams for the production of heavy quarks with $W$ bosons. In general the jets in such events are typical QCD jets with no special enrichment of the $b$ jet fraction. This background, therefore, can be considered as a product of two terms, each of which has a negligible contribution from $t\bar{t}$ events: the number of jets in $W$ + jets sample times the probability that a jet will have a $\mu$-tag.

The question is how to measure the tagging rate. True $W$ + jets events do not provide enough statistics to enable us even to scale from $W + 1$ jet and $W + 2$ jets to $W + 3$ and 4 jets. In order to get good statistics we measure the muon tagging rate of "fake $e$ + jets" events, that is of events selected by the level 2 ELE_JET_4_BKG trigger. This trigger requires a jet in which at least 80% of the energy is measured as electromagnetic (instead of an isolated

electron and $\not\!\!E_T$ as required by a $W$), and 3 other jets with a minimum jet $E_T$ of 10 GeV. $W$ candidates form only a small fraction and they are mainly QCD multijet events, though $W$'s are not excluded. Since this trigger neither triggers on muons nor has a $\not\!\!E_T$ requirement, it can provide an unbiased muon rate. We parameterize the probability of a $\mu$-tag as a function of jet $E_T$ and $\eta$. Assuming there is no correlation between $E_T$ and $\eta$, this rate can be decomposed as

$$P_{\mu-\text{tag}} = P_\eta(\eta) \cdot P_{E_T}(E_T)\,, \tag{4.14}$$

where $P_\eta$ is jet $\eta$ dependence and $P_{E_T}$ is the jet $E_T$ dependence. To study the $\eta$ dependence, we measure the ratio of the number of tagged jets to the total number of jets in different $\eta$ regions. The results are shown in Fig. 4.15. We subdivide the events into "pre-shutdown" (the runs before 89,000) and "post-shutdown" (the runs after 89,000) because some muon chambers were cleaned up during the February 1995 shutdown and thus the efficiency of the chambers changed. We parameterize the function $P_\eta$ as

$$P_\eta(\eta) = \frac{e^{-f\cdot\eta^2}}{(1+e^{-a(\eta+b)})(1+e^{c(\eta-d)})}\,. \tag{4.15}$$

From a fit to the data sample, we obtain $a = 10.12 \pm 1.84$, $b = 1.08 \pm 0.04$, $c = 9.33 \pm 2.26$, $d = 1.07 \pm 0.04$, $f = 1.15 \pm 0.11$ for the pre-shutdown, and $a = 15.25 \pm 2.70$, $b = 1.03 \pm 0.02$, $c = 10.80 \pm 1.52$, $d = 1.05 \pm 0.03$, $f = 0.51 \pm 0.11$ for the post-shutdown.

$P_{E_T}$ is calculated by the ratio of the number of tagged jets to the total of $P_\eta$ weighted jets in different $E_T$ bins. Since the $E_T$ of jets containing a

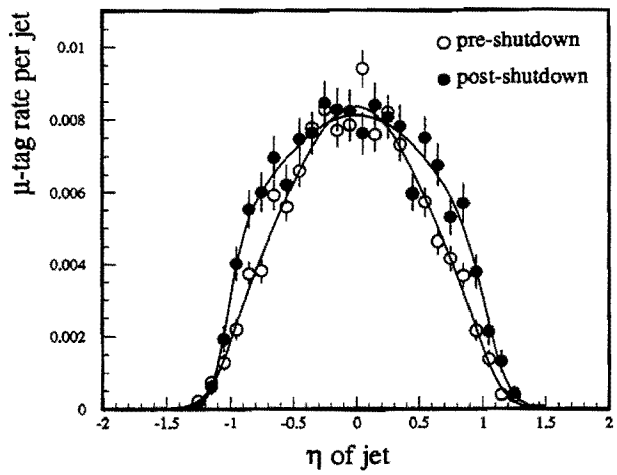


Figure 4.15: Muon tagging rate per jet as a function of jet $\eta$. We subdivide the data sample into "pre-shutdown" (open circles) and "post-shutdown" (solid circles) and fit to a function of $P_\eta(\eta) \sim \frac{e^{-f\cdot\eta^2}}{(1+e^{-a(\eta+b)})(1+e^{c(\eta-d)})}$.

muon systematically tends to be measured low in the calorimeter, the Monte Carlo study suggests adding the muon $p_T$ to the tagged jet for compensation. Fig. 4.16 shows $P_{E_T}$ for both the pre-shutdown and post-shutdown samples. The discrepancies between them are small in low $E_T$ region. We combine the data and parameterize the function $P_{E_T}$ as

$$P_{E_T}(E_T) = g \cdot \log_{10}(E_T) + h\,, \tag{4.16}$$

where $g = 0.0253 \pm 0.0007$ and $h = -0.0338 \pm 0.0011$.

To check this determination of the muon tagging rate, we calculate the expectations from Equation (4.14) in various samples and compare them to the measured values. The results are shown in Table. 4.8. We assume the heavy flavor content in $W$ + jets events is the same as, or less than that in QCD multijet events. This assumption is believed to be conservative. In $W$ + jets

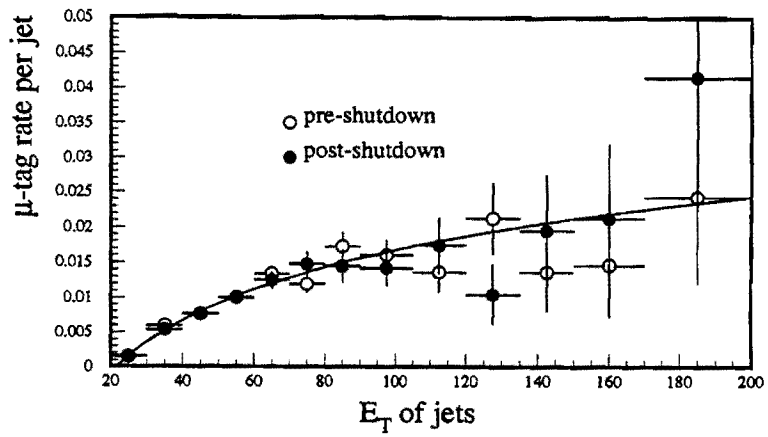


Figure 4.16: Muon tagging rate per jet as a function of jet $E_T$. The "pre-shutdown" (open circles) and "post-shutdown" (solid circles) have only small discrepancy in the low $E_T$ region. The curve is fitted to the combined data.

events, heavy flavor $b\bar{b}$ and $c\bar{c}$ pairs come from gluon splitting. In QCD multijet events, in addition to gluon splitting, direct production (e.g. $gg \rightarrow b\bar{b}$ or $c\bar{c}$) also generates heavy quark pairs. The VECBOS and ISAJET Monte Carlo calculations show heavy flavor content in $W$+jets events is smaller than that in QCD multijet events by about 7% [55]. The results suggest a 10% systematic uncertainty on the muon tagging rate prediction.

We can now take the numbers of jets from the inclusive $W$ + jets data sample and multiply them by the $\mu-$tag rate to obtain the background from $W$ + jets. The inclusive $W$ + jets sample contains the the fake electron events and unknown number of $t\bar{t}$ events. To avoid double counting the fake electron contribution, we correct it by

$$N_{bkg}^{W+\text{jets}}(\text{QCD corr}) = N_{bkg}^{W+\text{jets}} \cdot (1 - f_{bkg}^{QCD}), \tag{4.17}$$

where the $f_{bkg}^{QCD}$ is the QCD fraction in the inclusive $W$ + jets sample (see

| Event Sample | Total No. of Events | No. of Observed Tagged Muons | No. of Predicted Tagged Muons |
|---|---|---|---|
| JET_MIN (20 GeV jet trigger) | 282,493 | 237 | $250 \pm 14$ |
| JET_50 (50 GeV jet trigger) | 689,243 | 6,009 | $6132 \pm 84$ |
| JET_85 (85 GeV jet trigger) | 943,768 | 14,563 | $15,494 \pm 139$ |
| JET_MAX (115 GeV jet trigger) | 187,079 | 4,105 | $3951 \pm 29$ |
| JET_MULTI (10 GeV 5 jets trigger) | 475,552 | 7,494 | $7,464 \pm 35$ |
| $Z+ \geq 1$ jet | 399 | 2 | $1.22 \pm 0.03$ |
| $Z+ \geq 2$ jets | 54 | 0 | $0.39 \pm 0.01$ |

Table 4.8: A comparison of the observed number of tagged muons in different samples with the prediction from the muon rate. The uncertainties on the prediction is statistical error only.

Table 4.4). The results of background are shown in Table 4.9 .

### 4.3.3 Background Summary

In addition to the QCD and $W$ + jets backgrounds, there are some other small backgrounds from $Z \rightarrow \tau\tau$, and $W^+W^-$, $WZ$ diboson production. For the $Z \rightarrow \tau\tau$ case, we consider the case where one $\tau$ decays to an electron ($\tau \rightarrow e\nu_e\nu_\tau$) and the other decays to a muon ($\tau \rightarrow \mu\nu_\mu\nu_\tau$). The background from $WW$, $WZ$ events includes the following cases:

- $W \rightarrow e\nu$ and $W \rightarrow \mu\nu$.
- $W \rightarrow e\nu$ and $Z \rightarrow \mu\mu$.
- $W \rightarrow e\nu$ and $Z \rightarrow b\bar{b}$ $(c\bar{c}) \rightarrow \mu X$.

| Data Type | Total No. of events | No. of Estimated $\mu$-tags before correction | No. of Estimated $\mu$-tags after QCD correction |
|---|---|---|---|
| $N_{jet} \geq 1$ | 6139 | $19.97 \pm 2.05$ | $16.35 \pm 1.73$ |
| $N_{jet} \geq 2$ | 983 | $7.49 \pm 0.76$ | $5.42 \pm 0.60$ |
| $N_{jet} \geq 3$ | 159 | $2.14 \pm 0.21$ | $1.36 \pm 0.19$ |
| $N_{jet} \geq 3$ & $H_T > 120$ | 95 | $1.38 \pm 0.14$ | $0.81 \pm 0.13$ |

Table 4.9: The $W$+jets background estimate for the inclusive $W$+jets data sample. The results of the second column are calculated by using all the events in the $W$+jets sample. To prevent double counting QCD contributions, these results are corrected by Equation (4.17) and listed in the third column.

- $W \rightarrow \mu\nu$ and $Z \rightarrow ee$.

These backgrounds are determined by Monte Carlo simulations and then normalized to the luminosity of our data. A systematic uncertainty of 20% is assigned to the estimation due to the uncertainties of the event generator and energy scale of the calorimeter.

A summary of the background estimation for different jet multiplicities is present in Table 4.10. In the standard set of cuts ($N_{jet} \geq 3$ & $H_T \geq 120$) we obtain 4 signal events with estimated background $1.44 \pm 0.20$. The probability of an upward fluctuation of the background to 4 or more events is 6.1% ($1.6\,\sigma$). Although this signal by itself is not sufficient to establish the existence of the top quark, when we combine all channels together we obtain a good significance, as discussed in the final chapter.

| Background Source | No. of Background in Inclusive $W$ + jets Sample | | | |
|---|---|---|---|---|
| | $N_{jet} \geq 1$ | $N_{jet} \geq 2$ | $N_{jet} \geq 3$ | $N_{jet} \geq 3$ & $H_T > 120$ |
| QCD | $4.78 \pm 0.74$ | $2.00 \pm 0.37$ | $0.97 \pm 0.26$ | $0.61 \pm 0.20$ |
| W+jets | $16.35 \pm 1.73$ | $5.42 \pm 0.60$ | $1.36 \pm 0.19$ | $0.81 \pm 0.13$ |
| $Z \rightarrow \tau\tau$ | $0.47 \pm 0.12$ | $0.11 \pm 0.038$ | $0.029 \pm 0.016$ | $0.015 \pm 0.011$ |
| $WW$,$WZ$ | $0.039 \pm 0.015$ | $0.008 \pm 0.006$ | $0.002 \pm 0.002$ | $< 0.001$ |
| Total Background | $21.64 \pm 1.75$ | $7.54 \pm 0.62$ | $2.36 \pm 0.25$ | $1.44 \pm 0.20$ |
| No. of observed events | 22 | 9 | 5 | 4 |

Table 4.10: Summary of different backgrounds to the $t\bar{t}$ signal in the inclusive $W$ + jets data sample.

## 4.4 Signal Efficiency

The efficiency of $t\bar{t} \rightarrow e$ + jets + $\mu$−tag can be calculated as

$$\varepsilon = \varepsilon_{trig} \cdot \varepsilon_{offline} , \tag{4.18}$$

where $\varepsilon_{trig}$ is the trigger efficiency, $\varepsilon_{offline}$ is the offline efficiency, including the efficiencies of kinematic acceptance, reconstruction, and the particle ID cuts. The trigger efficiency is measured directly using collider data by comparing different triggers. The offline efficiency is determined from ISAJET Monte Carlo events with a full DØ detector simulation and then reconstructed by DØRECO. We use these MC events to calculate the acceptance and reconstruction efficiencies and then combine with the particle offline ID cut efficiencies from data to obtain $\varepsilon_{offline}$.

### 4.4.1 Trigger Efficiency

As described in Section 4.1 there are two triggers used in this analysis, ELE_JET_HIGH and EM1_EISTRKCC_MS. Both triggers require an EM cluster and $\not\!\!E_T$. ELE_JET_HIGH has an additional jet requirement. We factor the triggers into electron, $\not\!\!E_T$, and jet, then combine the results at the end.

To measure the electron trigger efficiency, we preselect events from a trigger without any EM requirement, then ask if events with an electron candidate satisfying offline requirements fired our signal triggers. We select the trigger JET_3_MISS for the study, which requires $\not\!\!E_T > 25\,\mathrm{GeV}$ and 3 jets with $E_T > 20\,\mathrm{GeV}$. We find the L1 and L2 combined efficiency of the electron trigger of ELE_JET_HIGH ($\varepsilon_e^{ELE}$) is $(99.8 \pm 0.2)\%$ and that of EM1_EISTRKCC_MS ($\varepsilon_e^{EM1}$) is $(94.2 \pm 1.1)\%$.

The efficiency of L2 $\not\!\!E_T$ is studied by using filter EM1_ELE_MON, which triggers on an EM cluster with $E_T > 20\,\mathrm{GeV}$. Since there is no $\not\!\!E_T$ requirement in this trigger, we can compare the L2 $\not\!\!E_T$ to that calculated from offline, then find the turn-on curve of L2 $\not\!\!E_T$ threshold. Because $\not\!\!E_T$ is strongly correlated to the number of jets, we select events with an electron candidate passing loose requirements and 3 or more reconstructed jets. Fig. 4.17(a) shows the $\not\!\!E_T$ spectrum for this sample (solid line) and the subsamples that also passed an additional L2 $\not\!\!E_T$ threshold of 14 GeV (dashed line). The efficiency of the L2 $\not\!\!E_T$ cut for each bin as a function of offline $\not\!\!E_T$ is the ratio of the dashed and solid histograms shown in Fig. 4.17(b). We then apply the L2 $\not\!\!E_T$ turn-on curve on $t\bar{t}$ MC to get the L2 $\not\!\!E_T$ trigger efficiency. We find that the efficiency

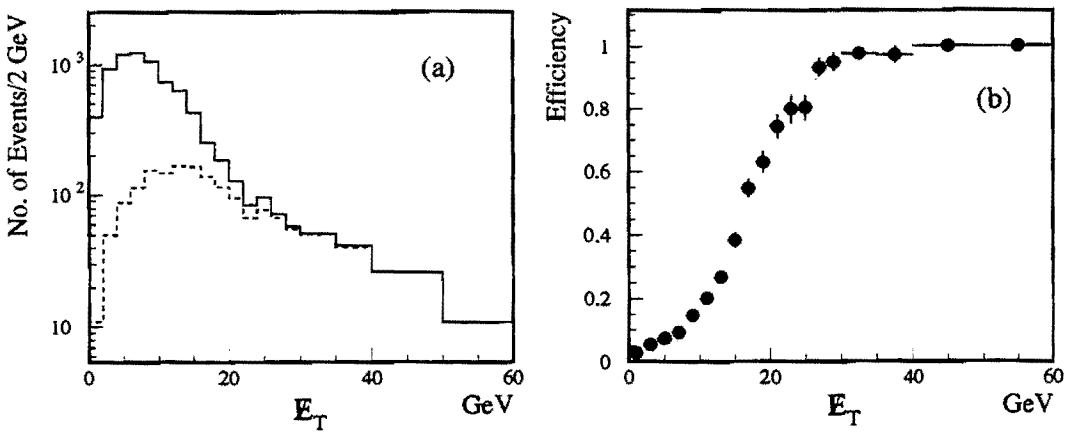


Figure 4.17: (a) $\not\!\!E_T$ spectra for the sample selected from EM1_ELE_MON trigger (solid line) and subsample also passing L2 $\not\!\!E_T$ of 14 GeV threshold (dashed line). (b) The efficiency of L2 $\not\!\!E_T$ threshold as a function of offline $\not\!\!E_T$.

for trigger ELE_JET_HIGH (with 14 GeV threshold) is $(97.5 \pm 0.5)\%$ and that for trigger EM1_EISTRKCC_MS (with 15 GeV threshold) is $(97.0 \pm 0.6)\%$. The uncertainties include the jet energy scale (0.2%) and different top masses used in MC (0.4%).

To measure jet trigger efficiency we select events with a loose electron and 3 or more jets from trigger EM1_EISTRKCC_MS, then observe how many of them also passed ELE_JET_HIGH. The results of this analysis shows the jet trigger efficiency ($\varepsilon_{jet}^{ELE}$) is $(98.0 \pm 0.9)\%$.

To get the overall efficiency for the signal triggers, we first assume there is no correlation between each factor. The efficiency of trigger ELE_JET_HIGH will be

$$\varepsilon^{ELE} = \varepsilon_e^{ELE} \cdot \varepsilon_{\not\!\!E_T}^{ELE} \cdot \varepsilon_{jet}^{ELE} .$$

In this way we obtain the efficiency for ELE_JET_HIGH trigger to be $(95.4 \pm$

1.0)%. The other extreme case (also the worst case) is that there is always only one factor inefficient at a time. In the case the overall efficiency would be

$$\varepsilon^{ELE} = 1 - (1 - \varepsilon_e^{ELE}) - (1 - \varepsilon_{\not{E}_T}^{ELE}) - (1 - \varepsilon_{jet}^{ELE}).$$

This calculation give us $(95.3 \pm 1.0)\%$. Since the difference between them is very small, we include the difference as a part of systematic error.

The efficiency for the trigger EM1_EISTRKCC_MS is calculated similarly and we obtain $(91.3 \pm 1.5)\%$.

We finally estimate the combined efficiency of these two signal triggers by the formula

$$\varepsilon_{trigger} = \varepsilon^{ELE} + (1 - \varepsilon_{jet}^{ELE}) \cdot \varepsilon^{EM1}, \tag{4.19}$$

where the first term is the contribution from ELE_JET_HIGH, and the second term is the contribution from EM1_EISTRKCC_MS only when events fail the jet trigger of ELE_JET_HIGH because the EM cluster and $\not{E}_T$ requirements of ELE_JET_HIGH are looser. The combined trigger efficiency is $(97.2 \pm 1.8)\%$.

### 4.4.2 Offline Efficiency

We use ISAJET MC to generate $t\bar{t}$ decay to everything for $m_t = 140$, 160, 180 and 200 GeV. The two MUSMEAR packages, one for pre-shutdown and the other for post-shutdown, are used to incorporate the the measured efficiencies of muon chamber modules. Both electron and muon ID efficiencies use the studies in the previous chapter. Based on the MC efficiency and trigger efficiency described above, the total efficiencies are listed in Table 4.11.

| Top Mass | Standard Set | | Loose Set | |
|---|---|---|---|---|
| | $\varepsilon \times Br\,(\%)$ | $N_{exp}$ | $\varepsilon \times Br\,(\%)$ | $N_{exp}$ |
| 140 GeV | $0.517 \pm 0.058$ | $6.5 \pm 0.8$ | $0.580 \pm 0.063$ | $7.3 \pm 0.9$ |
| 160 GeV | $0.672 \pm 0.073$ | $4.1 \pm 0.5$ | $0.740 \pm 0.079$ | $4.5 \pm 0.5$ |
| 180 GeV | $0.762 \pm 0.082$ | $2.4 \pm 0.3$ | $0.791 \pm 0.085$ | $2.5 \pm 0.3$ |
| 200 GeV | $0.956 \pm 0.101$ | $1.6 \pm 0.2$ | $0.990 \pm 0.105$ | $1.7 \pm 0.2$ |

Table 4.11: Efficiency$\times$ branching fraction ($\varepsilon \times Br$) and expected $t\bar{t}$ yields of $74.9\,\mathrm{pb}^{-1}$ data for different top mass. The cross section is based on the central theoretical $t\bar{t}$ production cross section of Ref. [16].

The following systematic uncertainties on the efficiency have been studied:

- Monte Carlo Generator: To estimate the uncertainty of Monte Carlo modeling the $t\bar{t}$ production and decay, we compare the acceptance of events generated by two different generators, ISAJET and HERWIG. ISAJET uses default EHLQ structure functions [51] and HERWIG uses CTEQ3M [56]. We find an uncertainty of 6% due to the generators at the parton level.

- Energy Scale: One major uncertainty is the relative energy scale for jets between data and Monte Carlo. Both data and MC use MPF method (see previous chapter) to correct jet energies. To determine this uncertainty we vary the MC energy correction by one standard deviation from its nominal correction. The change in acceptance is less than 5%.

- Electron Efficiency: Both electron reconstruction and offline ID cut efficiencies have been studied by using the $Z \rightarrow ee$ data. The overall

uncertainty is 3%.

- Muon Efficiency: The muon reconstruction efficiency is measured based on MUSMEAR packages. We compare the differences of several MUSMEAR packages from different runs and estimated 5% uncertainty. The uncertainty from offline ID cuts is 1.5%.

The total uncertainty is calculated by adding all effects in quadrature.

### 4.4.3 Cross Section for $t\bar{t}$ Production

To measure the $t\bar{t}$ production cross section, we assume that the observed excess events are due to $t\bar{t}$ production. Before calculating the cross section, we introduce a small correction to the $W$ + jets background. In Section 4.3.2 we calculated the $W$ + jets background by using the jets of $W$+ 3 or more jets events multiplied by $\mu$-tag rate. Since the inclusive $W$+jets events also contain QCD fakes and $t\bar{t}$ production and only the QCD fakes were corrected for, we have to make a further correction for the $t\bar{t}$ production. If the excess events correspond to the $t\bar{t}$ events in the sample after imposing the $\mu-$tag, dividing the number of excess by the $\mu-$tag efficiency for $t\bar{t}$ events ($15\% \pm 1\%$) yields the estimation of $t\bar{t}$ production before the $\mu-$tag requirement. The fraction of $t\bar{t}$ production in inclusive $W$ + jets events is estimated by

$$f_{t\bar{t}} = \frac{N_{obs} - N_{bkg}}{(0.15 \pm 0.01)\, N_{W+\text{jets}}}, \tag{4.20}$$

where $N_{obs}$ is number of observed events and $N_{bkg}$ is the expected total background, and $N_{W+\text{jets}}$ is the number of inclusive $W$ + jets events. The Equa-

tion (4.17) then is modified by

$$N_{bkg}^{W+\text{jets}}(\text{corr}) = N_{bkg}^{W+\text{jets}} \cdot (1 - f_{bkg}^{QCD} - f_{t\bar{t}}) \,. \tag{4.21}$$

We define the number of excess events as

$$N_{excess} \equiv N_{obs} - N_{bkg} \,. \tag{4.22}$$

Combining Equation (4.20), (4.21) and (4.22), we obtain the corrected number of the excess events as

$$N_{excess}(\text{corr}) = N_{excess} \cdot \left(1 - \frac{N_{bkg}^{W+\text{jets}}}{(0.15 \pm 0.01)\, N_{W+\text{jets}}}\right)^{-1} \,. \tag{4.23}$$

This correction increases the excess by about 10%.

The cross section of $t\bar{t}$ production then is calculated by

$$\sigma_{t\bar{t}} = \frac{N_{excess}(\text{corr})}{(\varepsilon \times Br) \times \int \mathcal{L} dt} \,, \tag{4.24}$$

where $(\varepsilon \times Br)$ is the efficiency $\times$ branching fraction in Table 4.11. We find that $\sigma_{t\bar{t}} = 4.9 \pm 3.5(\text{sta}) \pm 0.7(\text{sys})$ pb for standard cuts and $\sigma_{t\bar{t}} = 4.9 \pm 3.8(\text{sta}) \pm 0.8(\text{sys})$ pb for loose cuts if top mass is 180 GeV. The dominant error is due to the small statistics of candidate events. Fig. 4.18 illustrates the measured cross section as a function of top quark mass compared to that of the theoretical calculation.

| Top Mass | Standard Set $\sigma \pm \Delta\sigma_{sta} \pm \Delta\sigma_{sys}$ (pb) | Loose Set $\sigma \pm \Delta\sigma_{sta} \pm \Delta\sigma_{sys}$ (pb) |
|---|---|---|
| 140 GeV | $7.27 \pm 5.17 \pm 1.07$ | $6.84 \pm 5.15 \pm 1.02$ |
| 160 GeV | $5.59 \pm 3.98 \pm 0.81$ | $5.24 \pm 4.04 \pm 0.79$ |
| 180 GeV | $4.93 \pm 3.51 \pm 0.71$ | $4.90 \pm 3.78 \pm 0.75$ |
| 200 GeV | $3.93 \pm 2.80 \pm 0.56$ | $3.92 \pm 3.02 \pm 0.59$ |

Table 4.12: Cross section of excess events as a function of different top quark masses.

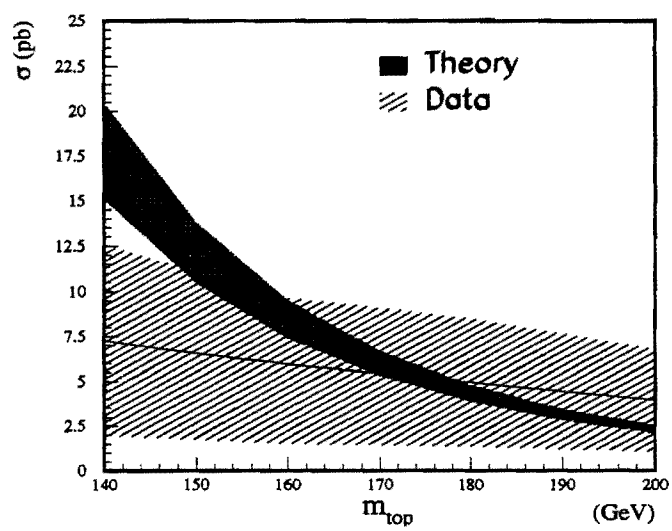


Figure 4.18: Measured cross section as a function of top quark mass. The solid line shows the central value of cross section calculated by standard set and the lighter band shows its one standard-deviation error. The theoretical calculation for $t\bar{t}$ production [16] is shown by the darker band.

# Chapter 5

# Conclusion

As described in the previous chapter, a search for $t\bar{t}$ production in the $e + \text{jets} + \mu-\text{tag}$ channel yields 4 candidates against an expected background of $1.44 \pm 0.20$ events in a luminosity of $74.9\,\text{pb}^{-1}$ data. The probability for an upward fluctuation of the background to 4 or more events is 0.061, which corresponds to $1.6\,\sigma$ for a Gaussian probability distribution. Based on the small excess of signal over background, the cross section for $t\bar{t}$ production was calculated to be $4.9 \pm 3.5(\text{stat}) \pm 0.7(\text{sys})\,\text{pb}$ (assuming $m_t = 180\,\text{GeV}$). This result is consistent with the earlier reported results by the DØ and CDF collaboration in their discovery papers [14, 15].

The DØ discovery paper included 3 dilepton channels ($ee$, $e\mu$ and $\mu\mu$) and 4 lepton+jets channels ($e$+jets without tagging, $e + \text{jets} + \mu-\text{tag}$, $\mu$+jets without tagging, $\mu+\text{jets}+\mu-\text{tag}$). Based on an integrated luminosity of about $50\,\text{pb}^{-1}$ collected in 1992-95, we found 17 candidate events, with an expected background of $3.8 \pm 0.6$ events. The probability for an upward fluctuation of the background to produce the observed signal is $2 \times 10^{-6}$(equivalent to $4.6\,\sigma$),

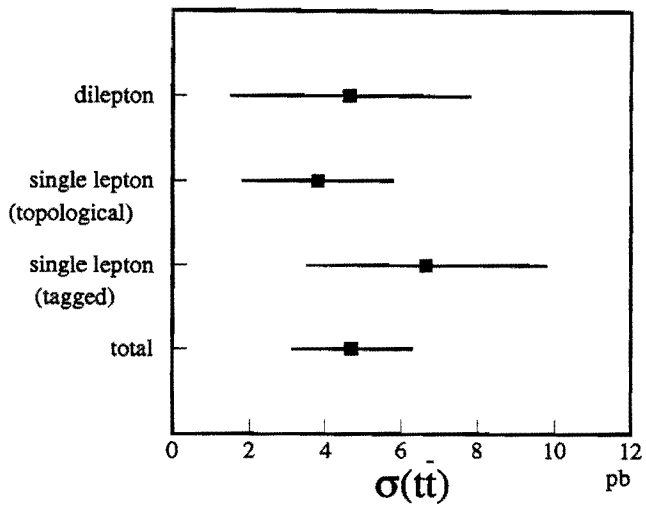


Figure 5.1: The cross section from the different top search channels.

so the existence of the top quark is firmly established. As of this year we have collected a total of about $100\,\mathrm{pb}^{-1}$ data. After re-optimizing the selection cuts for the cross section measurement by loosing some cuts, we find 37 events from 7 channels, with an estimated background of $13.4 \pm 3.0$ events. The cross section is measured as $5.2 \pm 1.8\,\mathrm{pb}$. The distribution of events among the several channels agree with the SM predictions for $t\bar{t}$ decays. This is also reflected in the cross section calculated in the individual channels shown in Fig. 5.1; the cross section for $t\bar{t} \rightarrow e + \text{jets} + \mu\text{−tag}$ that I have measured, $4.9 \pm 3.6\,\mathrm{pb}$, agrees with the overall $t\bar{t}$ cross section.

The mass of the top quark will provide very useful information to understand the Standard Model and beyond. However, because of limited statistics, it is hard to get a precise measurement from the current data. In the dilepton channel, it is even harder because there are two high $p_T$ undetected neutrinos from $W^+W^-$ decay in each event. For this reason, the current mass measurement is mainly based on the lepton+jets channels. The sample for the

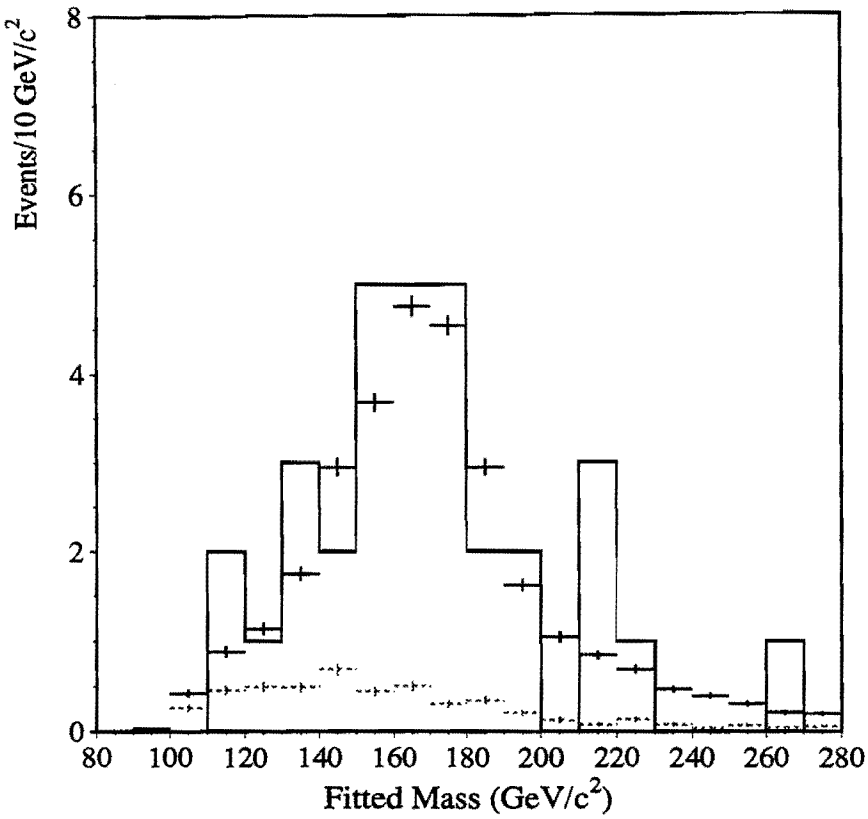


Figure 5.2: The fitted mass distribution for candidate events (histogram) with the expected mass distributions for top quark events (solid points) and backgrounds (dashed points).

fitting is a subset of the $e$ + jets and $\mu$ + jets candidates. A description of the fitting method is beyond the scope of this thesis. The latest result is $m_t = 169 \pm 8(\text{sta}) \pm 9(\text{sys})$ GeV [57] and the fit is shown in Fig. 5.2.

In the next run the upgraded DØ detector will be very good for studying the top quark. In particular, the new silicon vertex detector will be able tag $b$ quarks by identifying a secondary vertex. In addition, we will have a magnetic field in the central tracking system, which will improve the muon momentum

resolution and electron identification, and even allow us to tag $b$ quarks in the electron decay mode. With these improvements, we will be able to test the predictions of the Standard Model and may find some surprises.

# Bibliography


[1] S. L. Glashow, Nucl. Phys. **22**, 579 (1961).

[2] S. Weinberg, Phys. Rev. Lett. **19**, 1264 (1967).

[3] A. Salam, in *Elementary Particle Theory: Relativistic Groups and Analyticity (Nobel Symposium No. 8)*, edited by N. Svartholm (Almqvist and Wiksells, Sweden, 1968), p. 367.

[4] K. Gottfried, V. F. Weisskopf, *Concepts of Particle Physics*, Oxford University Press, 1986.

[5] M. Kaku, *Quantum Field Theory: A Modern Introduction*, Oxford University Press, 1993.

[6] S. W. Herb *et al.*, Phys. Rev. Lett. **39**, 252 (1977).

[7] M. L. Perl *et al.*, Phys. Lett. **35**, 1489 (1975).

[8] UA1 Collaboration, G. Arnison *et al.*, Phys. Lett. **B147**, 493 (1984); C. Albajar *et al.*, Z. Phys. **C48**, 1 (1990).

[9] UA2 Collaboration, T. Akesson *et al.*, Z. Phys. **C46**, 179 (1990).

[10] CDF Collaboration, F. Abe *et al.*, Phys. Rev. Lett. **64**, 147 (1990); Phys. Rev. Lett. **64**, 142 (1990); Phys. Rev. **D43**, 664 (1991); Phys. Rev. Lett. **68**, 447 (1992); Phys. Rev. **D45**, 3921 (1992).

[11] G. L. Kane, *Modern Elementary Particle Physics*, Addison-Wesley, 1993.

[12] DØ Collaboration, S. Abachi *et al.*, Phys. Rev. Lett. **72**, 2138 (1994).

[13] CDF Collaboration, F. Abe *et al.*, Phys. Rev. Lett. **73**, 225 (1994); Phys. Rev. **D50**, 2966 (1994).

[14] DØ Collaboration, S. Abachi *et al.*, Phys. Rev. Lett. **74**, 2632 (1995).

[15] CDF Collaboration, F. Abe *et al.*, Phys. Rev. Lett. **74**, 2626 (1995).

[16] E. Laenen, J. Smith, and W. van Neerven, Phys Lett. **B321**, 254 (1994); Nucl. Phys. **B369**, 543 (1992).

[17] Particle Data Group, Phys. Rev. **D50**, 1173 (1994).

[18] The LEP Collaboration and the LEP Electroweak Working Group, CERN Report No. CERN-PPE/94-187, 1994 (unpublished).

[19] Plot generated by Marcel Demarteau using calculations from Halzen and Kniehl and the LEP Electroweak Working Group ZFITTER Program (V4.8); F. Halzen and B. A. Kiehl, Nucl. Phys. **B353**, 567 (1991).

[20] L. M. Lederman, "The Tevatron", Scientific American, Vol. 264, p. 53, March 1991.

[21] H. T. Edwards, Ann. Rev. Nucl. Part. Sci., **35**, 605 (1985).

[22] DØ Collaboration, S. Abachi *et al.*, Nucl. Instrum. Methods **A338**, 185 (1994).

[23] A. R. Clark *et al.*, Nucl. Instrum. Methods **A279**, 245 (1989).

[24] J. F. Detoeuf *et al.*, Nucl. Instrum. Methods **A265**, 157 (1988); Nucl. Instrum. Methods **A279**, 310 (1989).

[25] S. J. Wimpenny *et al.*, Nucl. Instrum. Methods **A279**, 107 (1989).

[26] A. L. Spadafora *et al.*, Nucl. Instrum. Methods **A315**, 279 (1992).

[27] C. Brown *et al.*, Nucl. Instrum. Methods **A279**, 331 (1989).

[28] J. M. Butler *et al.*, Nucl. Instrum. Methods **A290**, 122 (1990).

[29] Yu. M. Antipov *et al.*, Nucl. Instrum. Methods **A297**, 121 (1990).

[30] G. S. Gao and R. Partridge, IEEE Trans. Nucl. Sci. **NS-38**, 286 (1991).

[31] M. Abolins *et al.*, IEEE Trans. Nucl. Sci. **NS-36**, 384 (1989).

[32] M. Abolins *et al.*, Nucl. Instrum. Methods **A289**, 543 (1990).

[33] D. Cutts *et al.*, IEEE Trans. Nucl. Sci. **NS-36**, 738 (1989).

[34] D. Edmunds, S. Gross, and P. Laurens, "The Level 1.5 Trigger Framework for DØ", DØ Note 1638, 1993 (unpublished).

[35] J. Drinkard, "The DØ Level 1.5 Calorimeter Trigger", DØ Note 2274, 1994 (unpublished).

[36] J. Yu, "Determination of the Strong Coupling Constant ($\alpha_s$) and a Test of Perturbative QCD Using $W$+jets Processes in the DØ detector", Ph.D. Thesis, State Univ. of Stony Brook, 1993 (unpublished).

[37] DØ Collaboration, S. Abachi, *et al.*, Phys. Rev. **D52**, 4877 (1995).

[38] M. Narain, "Electron Identification in the DØ detector", DØ Note 1548, 1992 (unpublished).

[39] M. Narain, in *The Fermilab Meeting Proceeding of Meeting of the Division of Particles and Fields of the American Physical Society, Batavia, Illinois, 1992*, edited by C. Albright, P. Kasper, R. Raja, and J. Yoh (World Scientific, Singapore, 1993).

[40] J. Neyman and E. S. Pearson, Phil. Trans. Roy. Soc., **231**, 289 (1933).

[41] J. Neyman, *First Course in Probability and Statistics*, Henry Holt & Co, 1950.

[42] M. Narain and U. Heintz, "A Likelihood Test for Electron ID", DØ Note 2386, 1994 (unpublished).

[43] CDF Collaboration, F. Abe *et al.*, Phys. Rev. Lett. **69**, 2896 (1992).

[44] E. Gallas, "The MTC Package (Muon Tracking in the DØ Calorimeter)", DØ Note 2066, 1994 (unpublished).

[45] C. Gerber *et al*, "Muon Momentum Determination", DØ Note 2140, 1994 (unpublished).

[46] F. Paige and S. Protopopescu, "ISAJET 6.49: A Monte Carlo Event Generator for $pp$ and $\bar{p}p$ Interactions", Fermilab Computing Division PM0059, 1992 (unpublished).

[47] R. Field and R. Feynman, Nucl. Phys. **B136**, 1 (1978).

[48] F. A. Berends, W. T. Giele, H. Kuijf, and B. Tausk, Nucl. Phys. **B357**, 32 (1991).

[49] J. Botts *et al.*, Phys. Lett. **B304**, 159 (1993).

[50] J. Womersley, *Proceedings of the XXVI International Conference on High Energy Physics*, Dalas, Texas, 1992, edited by. Sanfor. AIP Conf. Proc. No.272 (AIP, New York, 1993).

[51] E. Eichten *et al.*, Rev. Mod. Phys. **56**, 579 (1984).

[52] G. Marchesini and B. Webber, Nucl. Phys. **B310**, 461 (1988); I. G. Knowles, Nucl. Phys. **B310**, 571 (1988); G. Marchesini *et al.*, Comp. Phys. Comm. **67**, 465 (1992).

[53] M. Fatyga, "Tuning electron ID parameters for the Level 2 trigger using testbeam data", DØ Note 1768 , 1993 (unpublished).

[54] J. Bantly, A. Brandt, R. Partridge, J. Perkins, and D. Puseljic, "Improvement to the DØ luminosity monitor constant", DØ Note 2544, 1995 (unpublished).

[55] J. Butler, H. Greenlee, R. Partridge, and H. Xu, "$W$+jets background to $t\bar{t} \to e + \text{jets} + \text{soft}\,\mu$", DØ Note 2141, 1994 (unpublished).

[56] H. L. Lai *et al.* Phys. Rev. **D51**, 4763 (1995).

[57] P. Bhat, J. Cochran, F. Hsieh, M. Jones, R. Gilmartin, J. McDonald, R. Partridge, H. Prosper, S. Protopopescu, S. Snyder, M. Strovink, T. Trippe, E. Varnes, and G. Watts, "Measurement of Top Mass Using Lepton + Jets Events", DØ Note, 1996 (unpublished), note number not assigned yet.